Surface-Mounted Metal-Organic Frameworks for Extreme Ultraviolet Lithography

Exploration of New Nanopatterning Processes

Cover design by Suzanne Deuss

ISBN: 978-94-6423-250-9
Digital version is available at http://dare.uva.nl/en

Printed and bound by ProefschriftMaken
Amsterdam, The Netherlands, 2021

Surface-Mounted Metal-Organic Frameworks for Extreme Ultraviolet Lithography

Exploration of New Nanopatterning Processes

ACADEMISCH PROEFSCHRIFT

ter verkrijging van de graad van doctor
aan de Universiteit van Amsterdam
op gezag van de Rector Magnificus
prof. dr. ir. K.I.J. Maex
ten overstaan van een door het College voor Promoties ingestelde commissie,
in het openbaar te verdedigen in de Agnietenkapel
op donderdag 3 juni 2021, te 13.00 uur

door Olivier Christian Maurice Lugier
geboren te Niort

Promotiecommissie

Promotor:	prof. dr. A.M. Brouwer	Universiteit van Amsterdam
Copromotor:	dr. S. Castellanos Ortega	Advanced Research Center for Nanolithography
Overige leden:	dr. R.M. Williams	Universiteit van Amsterdam
	dr. S. Grecea	Universiteit van Amsterdam
	prof. dr. M.S. Golden	Universiteit van Amsterdam
	prof. dr. P. Swiderek	University of Bremen
	dr. ir. M.A. van der Veen	TU Delf

Faculteit der Natuurwetenschappen, Wiskunde en Informatica

The research described in this thesis was carried out at the Advanced Research Center for Nanolithography (ARCNL), a public-private partnership of University of Amsterdam (UvA), the Vrije Universiteit Amsterdam (VU), the Netherlands Organisation for Scientific Research (NWO) and the semiconductor equipment manufacturer ASML.

Table of contents

Chapter 1

Introduction

1.1 Photolithography

1.1.1 Computer chips and transistors

The invention of metal oxide semiconductor (MOS) transistors is considered one of the most significant technological innovations in history. MOS transistors enabled the development of integrated circuits[1] and second-generation computers, also known as transistor computers, in 1954. The room-sized vacuum tube computers (*e.g.*, Colossus 1943, ENIAC 1946) made space for the first transistorized computer (TRADIC 1954) measuring 3 cubic feet, a symbolic starting point of a miniaturization trend still very relevant today.

Transistors are embedded in electronic circuits (IC), also called chips or microchips, where they act as logic gates working together to provide computing power to the device. Adding more transistors to a microchip increases its computing power. This means that by miniaturizing the transistors of an IC—effectively increasing their density—one can simultaneously increase the computing power and reduce the size of a computer.

In 1965 Gordon Moore made an economic forecast concerning the development of integrated circuits in which he stated that the number of transistors in a microchip would double every year. As the semiconductor industry matured, Gordon Moore modified his forecast in 1975 predicting a doubling of the number of transistors every two years. This economics "prediction", now known as Moore's Law[2], has been widely adopted as a roadmap by the semiconductor industry, continuously stimulating innovation towards fixed two-years objectives.

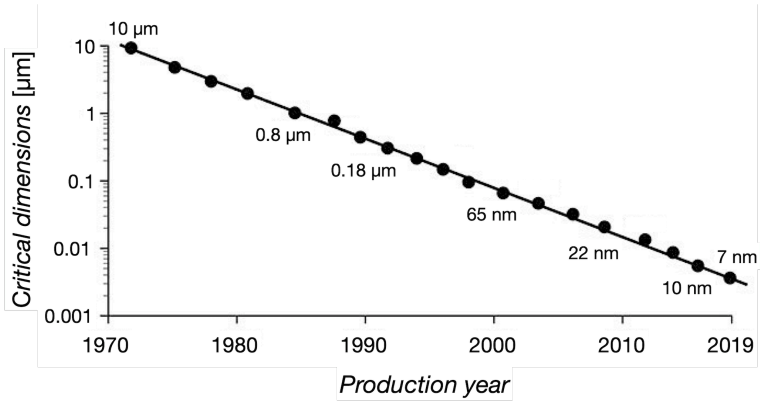

Figure 1.1: Evolution of the minimum feature size of transistors and other components of integrated of their year of production. Adapted from the International Roadmap for Devices and System (IRDS),[3] the International Technology Roadmap for Semiconductors (ITRS).[4]

In the following decades, technological and industrial development decreased production costs while economic growth simultaneously increased the affordability of technological devices which led to a significant expansion of their market share. After years of downscaling promoted by Moore's Law (Fig. 1.1), computer chips now host billions of nanometer-scale transistors integrated in complex circuitry enabling pocket-sized technological devices with astonishing computing power.

1.1.2 Evolution of photolithography: innovations driven by economics

Photolithography is the technology used to fabricate computer chips. It uses light in an intricate procedure to print billions of nanometre-scale transistors per square centimetres on a substrate. The procedure uses a photosensitive material deposited on the substrate, called photoresist, to first materialize the patterns before their subsequent transfer to the underlaying substrate in later steps.
Because light serves as patterning tool, the minimum printable feature size, also called critical dimension or resolution, is defined by the following equation derived from Rayleigh's resolution criterion:[5]

$$R = k_1 \frac{\lambda}{NA}$$

Here, k_1 is a constant coefficient representing process-related factors, λ the wavelength of the photons and NA the numerical aperture of the system. This equation shows that to decrease the resolution limit—in other words, to print smaller features—one can increase the NA or decrease the wavelength of the light. The semiconductor industry used both of these methods on various occasions throughout the years to keep up with the exponential downscaling required by Moore's Law.

First, photolithographic tools used mercury arc lamps generating photons at a wavelength of 435.8 nm (g-line), later reduced to 365.4 nm (i-line), with resolution limits around 3 µm and 600 nm, respectively. Then, deep ultraviolet (DUV) light was implemented with the KrF excimer laser at a wavelength of 248 nm and the ArF excimer laser introduced in the late 1990s with a wavelength of 193 nm. DUV lithography in its simplest form achieves a resolution limit below 40 nm, although immersion technology or multi-patterning methods can reach resolutions below 20 nm. Immersion technology increases the numerical aperture of the system by using a liquid medium (ultra-pure water) to replace the air gap between the end of the optical system and the substrate.[6] Multi-patterning consists in running multiple lithographic procedures with specially designed patterning sequences to create feature sizes smaller than the resolution limit at the cost of production rate.[7]

Currently, immersion DUVL, with single- or multi-patterning, remains the principal technology used to fabricate microchips[8] but macroeconomics and relentless consumer demand for more advanced devices instigated the development of extreme ultraviolet lithography (EUVL), with yet another reduction of the wavelength to 13.5 nm.

1.1.3 Development of EUV lithography

The transition from 193 nm to 13.5 nm light corresponds to a significant increase in photon energy from 6.4 eV to 92 eV. Thus, the semiconductor industry's commitment to EUV needed a major upgrade of the lithographic tools and methods to account for the major differences between the respective physics of DUV and EUV. New scanners incorporating new types of photon source (tin droplets and IR laser), optics (mirror optics) and photomasks (reflection interference) had to be developed to accommodate EUV and unlock high-volume manufacturing of integrated circuits with sub-20 nm resolution.

After roughly 20 years of research and development, the first devices branded with "EUV-inside" were released to the consumers market in August 2019, by Samsung. Although DUVL remains the dominant technology used in the fabrication of microchips, the gradual shift to EUVL steadily progresses as chipmakers upgrade their production lines.[9]

Regardless of this recent milestone and favorable forecast, the semiconductor industry is already focusing on the next technology with the development of high numerical aperture (high-NA) EUVL, aiming at sub-8 nm resolution by 2028.[3]

1.2 EUV-Lithography

1.2.1 Principles and physics of EUV

As in previous lithographic technologies, EUVL requires a lithography tool, known as EUV scanner, a substrate, and a photosensitive material to convert the aerial image (the distribution of light intensity as a function of spatial position in the image plane) into the desired patterns on the substrate, called photoresist or resists. During patterning, EUV scanners project light by means of a reflection mask onto a thin photoresist layer, 20 - 40 nm thick, previously deposited on a wafer usually via spin-coating. Unlike the more conventional absorption mechanisms occurring during UV or DUV exposures, EUV photons interact with both valence and core or semi-core electrons. Upon absorption of an EUV photon, the electron that it interacts with is emitted and the atom is ionized. For an electron emitted from the valence band, the kinetic energy after photoionization is estimated ~80 eV. Such photoelectron can then transfer energy to electrons from neighbouring atoms via inelastic scattering. These secondary events produce additional electrons, or secondary electrons, in a phenomenon called the electron cascade (Fig. 1.2). In addition to the inelastic scattering,

Auger processes (atomic relaxation processes) are also known to occur, providing even more free electrons to the system.[10,11]

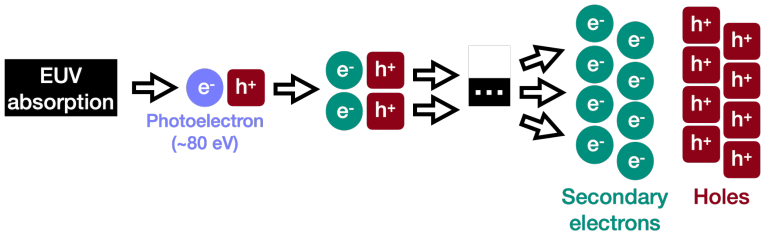

Figure 1.2: Schematic representation of the electron cascade. A hole is also created with each photo- and secondary electron emitted.

During exposure, photoelectrons and secondary electrons, as well as the ionized molecules from which they are generated, trigger various chemical reactions in the resist. As a result of these chemical changes, the solubility rate of the photoresist in a specific developing solution or solvent is altered, a phenomenon named “solubility switch”. After the exposure, the solubility switch enables the selective removal of either exposed or unexposed areas of the material during the development phase, effectively materialising the aerial image onto the photoresist. A photoresist is called negative tone if its solubility decreased upon exposure and positive tone if its solubility increased. The following steps of the procedure are etching and stripping, in which the pattern is transferred to the substrate and the remaining photoresist material removed from the substrate, respectively (Fig. 1.3).

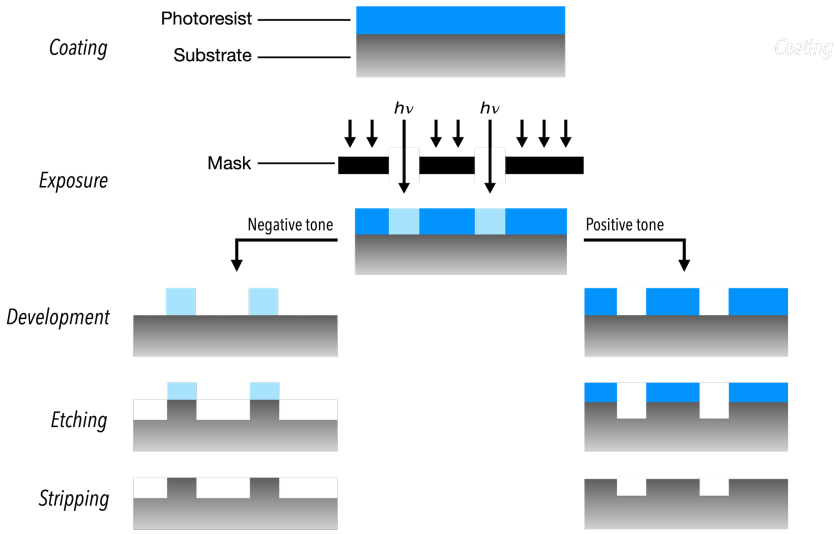

Figure 1.3: Photolithographic patterning principle

In summary, three concepts are most relevant in EUV lithography; (1) EUV photons are absorbed by atoms and interact with valence and (semi-)core level electrons, which means that the EUV absorptivity of a resist material depends mainly on its atomic composition and density; (2) multiple low energy electrons are created from the absorption of a single EUV photon; (3) these low energy electrons and the ionized molecules are responsible for the solubility switch, as they trigger diverse chemical reactions within the resist.

1.2.2 EUV Photoresists

Traditional lithography (UV, DUV) resists usually are organic materials named chemically amplified resists (CARs) comprising polymeric platforms, photoacids generators and photoacid quenchers. The photoacid generators (PAGs) are converted to acid upon reacting with photons (DUVL) or electrons (EUVL). The acids then react with the polymer molecules in a catalytic reaction that alter the local solubility of the CAR and leads to the solubility switch of exposed areas. Quenchers limit the diffusion of the photoacid within the resist which reduces the pattern blur.[12] Chain scission resists are similar polymer-based resists that do not have PAGs nor quenchers in their matrix but solely depend on photon-induced bond cleavage to achieve the solubility switch. Polymethylmethacrylate (PMMA) is a well-known example of a chain scission photoresist.

The first EUV photoresists were derived from these organic materials, yet metal-containing materials recently gained protagonism as specifically designed photoresists for EUV lithography, as they show promising performance, particularly in EUV absorptivity.[13] This is because many metal atoms have higher photon-absorption cross sections for 92 eV photons (Fig. 1.4) than the lighter atoms typically found in traditional resists. A better absorptivity may translate into better sensitivity, better patterning stochastics and better pattern quality.

The ionization phenomenon however, of which the probability is determined by the inherent absorptivity of the resist, is only the first step in a series of processes and reactions leading to the solubility switch. The efficiency of these events determines the photochemical quantum yield of the material. The quantum yield describes the number of times a certain reaction, deemed relevant for the solubility switch, takes place per absorbed photon. A resist with high quantum yield and a low absorptivity can have the same sensitivity as a resist with low quantum yield and high absorptivity. This is why metal containing resists are not systematically outperforming their organic counterparts, despite a better overall absorptivity. Nevertheless, organic-inorganic resists have demonstrated enough potential, particularly regarding etch resistance (Fig. 1.3), to justify the shift of focus from purely organic materials.

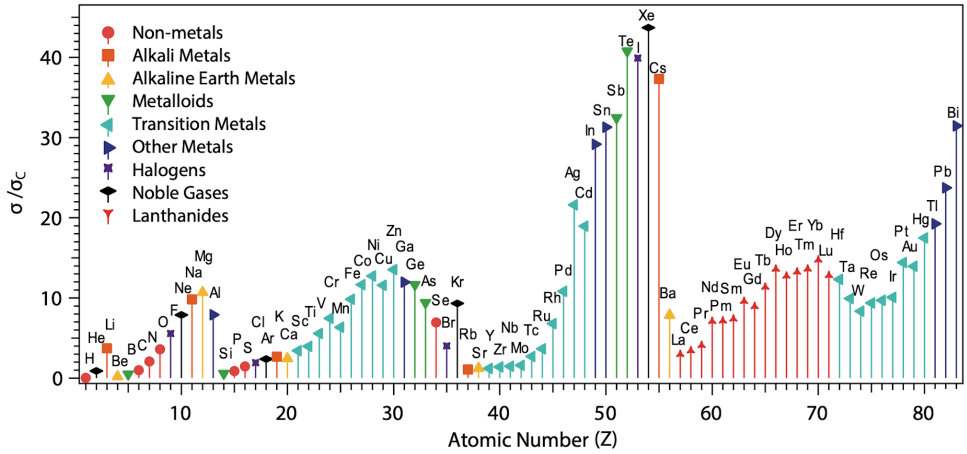

Figure 1.4: Photoabsorption cross section at 92 eV, relative to carbon, as a function of the atomic number of the atom, for Z = 1 to 83. Adapted from Refs 14,15.

1.2.3 Photoresists performance: the RLS trade-off

Resist performances are usually defined by a set of three main parameters: sensitivity (S), or minimum dose (in mJ/cm^2) required to obtained the desired patterns after development; resolution (R), or smaller printable feature (in nm), and critical dimension deviation (L), the deviation (in nm) from the ideal shapes of the original pattern (Fig. 1.5). The latter includes multiple factors, namely the line edge roughness (LER) and line width roughness (LWR) for linear patterns, and the local critical dimension uniformity (LCDU) for circular holes and pillars.

The concept of RLS trade-off, derived from the aforementioned performance observables (resolution, critical dimension deviation, and sensitivity), is the notion that one of these resist's parameters cannot be improved without deteriorating the others. This is because they are inversely dependent; for instance, if the sensitivity of a resist improves, less photons are required to print a feature and the CD deviation of that feature increases due to higher photon absorption stochastics. Although unrelated to photoresists, the contrast of the aerial image (the distribution of light intensity as a function of spatial position in the image plane) is also taken in consideration in the RLS equation and is constantly optimized for given resolutions by the manufacturers of EUV scanners (*i.e.*, ASML).

Various innovative methods have been developed to overcome the RLS trade-off of traditional resists. However, taking CARs and metal-containing resists as an example, it seems that the most efficient way to improve performances is to significantly change the composition of the resist material to generate new RLS parameters that rely on a differently

weighted set of factors. The problem of the RLS trade-off makes a strong argument for the investigation of new types of materials and methods for EUVL.

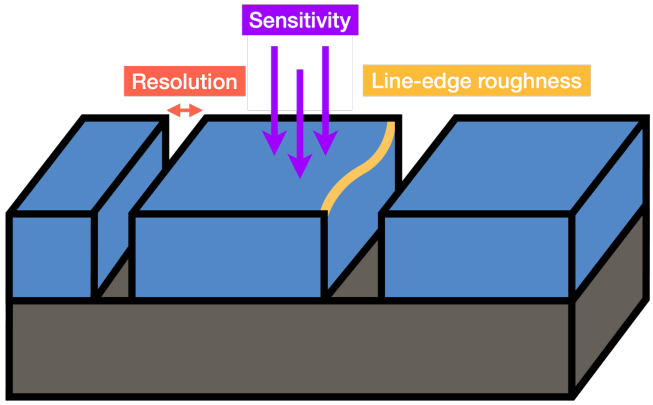

Figure 1.5: Example of straight line/space patterns printed in a photoresist illustrating the RLS parameters.

1.3 Limits of EUVL

EUVL needs to improve its fundamental understanding of the various processes inherent to the exposure step of the lithographic procedure (EUV-induced chemistry). Various crucial physico-chemical and radiative events taking place upon exposure are yet to be understood in detail, which slows the development of optimal photosensitive materials for this technology.[16–20]

Electron-generating events (number of secondary electrons generated per absorbed photon, role of Auger processes, role of the substrate), scattering events (photo- and secondary-electron energy distribution, electron mean free path, yield of secondary-electron generation, *etc.*) and chemical events (low-energy-electron reactivity, influence of dopants or contaminants, role of interfaces, *etc.*) fall in this category. The intricacy of these phenomena, lack of accurate theoretical models and limited possibilities for in-situ studies hinder photoresists research. In addition, pre- and post-exposure procedures (pre-bake, post-exposure baking, *etc.*) have proven to have an impact on the sensitivity and the quality of the patterns of resists but the exact nature and extent of their influence have yet to be fully understood.[21,22]

The upcoming switch to high-NA EUVL will add its share of challenges. Increasing the numerical aperture of a system reduces the depth of focus of the aerial image of the patterns. In the case of EUVL, the depth of focus determines the depth within which the patterns of the aerial image are sharp. If the depth of focus is smaller than the thickness of the resist

layer, the patterns will be partially blurred and lost during the etching procedure. This means that, high-NA EUVL will require thinner photoresist's layers, placing additional pressure on material scientists to improve their absorptivity.[23,24]

Consequently, to fulfil the requirements of upcoming nanofabrication technologies, EUV research should not focus solely on improving existing resists but new concepts and systems that can effectively react to radiation with nanoscale spatial resolution should be explored and accompanied with investigations of the fundamental aspects of their functioning.

1.4 Metal-organic frameworks and self-assembled monolayers

1.4.1 Description, properties and applications

MOFs are crystalline organic-inorganic materials first reported in 1999 by Yaghi et al.[25] They are composed of inorganic clusters, mostly metal oxo clusters, linked to each other by organic linkers forming 1D, 2D or 3D crystalline structures (Fig. 1.6). MOFs are actively studied for their numerous properties (porosity, conductivity, polarizability, fluorescence, *etc.*) that the scientific and industrial communities are trying to exploit in a wide array of applications, such as gas storage, gas separation, sensors, electronics, catalysis, photovoltaics, drug transportation or water capture.[26–28] Since 1999, more than 90,000 structures of MOFs have been reported and 500,000 predicted.[29,30]

Most MOFs are synthesised in the form of monocrystals or powders but can also be grown as thin films on a substrate, with thicknesses usually ranging from a few tens of nanometres to several micrometres, as a so-called surface mounted metal-organic framework (SURMOF). SURMOFs are chemically bonded to their surface, typically by means of an underlaying self-assembled monolayer (SAM) that acts as an anchor between material and substrate. Their development was motivated by their higher potential for device-integration as compared to MOFs synthesized as powders.[31,32]

Despite the scrutiny and sheer amount of research projects conducted on MOFs and SURMOFs their transition from laboratory materials with promising properties to active components in personal devices or industrial equipment remained limited to a few examples (TruPick™ by MOF Technologies in 2016, ION-X by NuMat in 2018).[33,34] Regardless, (SUR)MOFs have asserted themselves as high-potential materials to be used as central component in a wide range of technological, industrial, medical and personal devices.

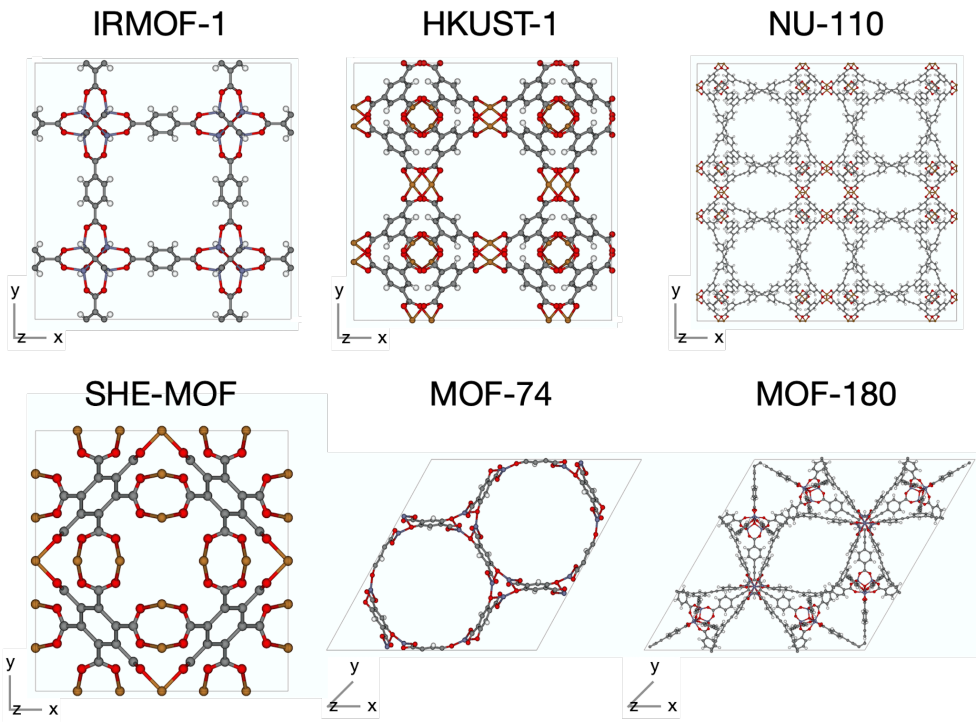

Figure 1.6: Unit cells of three-dimensional MOFs.

1.4.2 SURMOFs and EUVL

MOFs are closely related to a type of metal-containing photoresists currently investigated in our research group for EUVL applications, called metal oxo-clusters (MOCs). MOCs are promising candidates for EUVL because of their potential for fine tuning in absorptivity and reactivity. They are composed of an inorganic core made of metal-oxo clusters (Zn, Sn, Hf, Cu, Zr, etc.) coordinated by organic ligands. The clusters act as main EUV-light absorbers and photoelectron emitters, whereas the ligands react with the photo- and secondary-electrons to provide chemical contrast and the required solubility switch for the development step.[13,14,35]

While MOCs and other molecular versions of metal-containing resists are gaining traction in the EUV community, MOFs have remained untested, even though these two types of materials share several key properties for efficient EUV resists. MOFs can be described as a type of metal-containing resists where the metal atoms, or metal-oxo clusters, are interlinked in well-defined directions and with long-range periodicity. Therefore, a SURMOF film could be portrayed as a crystalline and lower density equivalent of its MOC counterpart (Fig. 1.7).

The differences between the molecular MOCs and the macrostructures of crystalline MOFs represent an advantageous scenario for fundamental EUV research. Mainly, the comparison of their respective performances can provide insights on the nature of EUV-induced events. Moreover, because of their unique set of properties, SURMOFs can help with the development of concepts that have not yet been explored. For example, their remarkable porosity and free volume could be exploited to transform the MOF into a "container" in which other photoresists or materials (MOCs, polymers, polymer precursors, etc.) could be loaded and exposed in a periodical spatial distribution that only their pores can provide.[36] Another interesting example of such hypothetical concepts, would be to take advantage of the spatial alignment of the ligands to control the direction of propagation of the electron induced reactions and significantly reduce line edge roughness and lateral blur.[37]

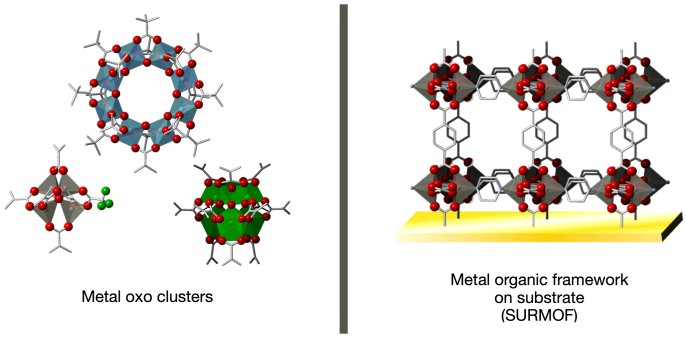

Figure 1.7: Comparison between MOCs specimens designed for EUV lithography (left) and a SURMOF of the DMOF-1 family.[38] From left to right, the MOCs shown are: Zn_4OL_6, $Ti_8O_8L_{16}$ and $Zr_6O_4(OH)_4L_{12}$ (L = ligand).

Finally, like for many other device-integrated materials, SURMOFs will likely require some type of patterning for successful device-integration. Thus, the potential of EUVL for high throughput patterning of nanometer- to micrometer-scale patterns could become attractive for (future) MOF-containing devices.

1.4.3 Self-Assembled Monolayers, SURMOFs and EUVL

Self-Assembled Monolayers (SAMs) are of utmost relevance in the preparation of SURMOFs since they can act as a template for the SURMOF growth constituting the interface between MOF and substrate. SAMs consist of a one-molecule thick layer with a packing order dictated by intermolecular interactions and various physical forces applied to them during the deposition process. A substrate on which a monolayer is deposited is said to be functionalized by the SAM. Substrates can be functionalized via vapor-based or solution-based deposition techniques. The most common types of SAMs are silanes, compatible with hydroxylated surfaces (glass, quartz, silicon oxide, aluminium oxide) and thiols, compatible

with coinage metal surfaces (gold, silver, copper, etc.). Silanes and thiols are composed of a head group with a strong affinity for the substrate, a so-called spacer that can be virtually any type of organic unit and a terminal functional group that determine the surface properties (Fig. 1.8).[39,40]

Several investigations on the influence of the SAM on the growth of SURMOFs showed the terminal group to have a strong impact on some key properties of the material, such as the homogeneity of the film or its crystalline orientation.[41,42] Note that for a SURMOF to grow on a functionalised substrate, its inorganic constituents should be able to coordinate with the terminal group of the SAM. This means that when a SAM species is favourable to the growth of one type of MOF it can be unfavourable to another type of MOF for a fixed set of synthetic conditions.

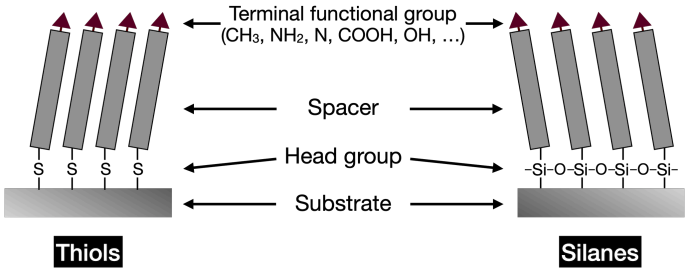

Figure 1.8: Thiols (left) and silanes (right) forming self-assembled monolayers on substrates.

Thiol SAMs are known to slowly desorb with time and the rate of desorption is inversely proportional to the packing quality. Consequently, when a thiol monolayer is damaged, the areas surrounding the defect desorb faster than pristine areas. One can take advantage of this phenomenon to pattern a monolayer with a different species of thiol and create a patterned mixed monolayer. To do that, the patterns are first printed in a monolayer by a damage-inducing force (radiation or mechanical force). Then, when the substrate is exposed to a different type of thiol in a solution or in gas phase, the faster desorption rate of the molecules located within damaged areas generates a selective exchange.[43,44] Moreover, SAMs have been proven to be easily damaged by low energy electrons.[45–48]

Based on these properties, in this thesis we designed patterning procedures involving SAMs and EUVL. By shining EUV light on a substrate prone to absorb EUV photons and functionalized by a SAM, the electron cascade initiated in the substrate can damage the molecules on its surface. If sufficient damage is sustained by the monolayer, the chemical differences obtained at the surface (chemical contrast) can be used to selectively grow or deposit various types of materials (*e.g.* DNA, nanoparticles, quantum dots, MOFs, perovskites) [49–56]. If the chemical contrast between the exposed and pristine areas is too low to support a selective deposition of the material of interest, one can still take advantage of

the contrast in packing order to selectively replace the exposed molecules. Providing that the chemical properties of the replacement molecules are different enough from those of the pristine SAM molecules, the newly obtained chemical contrast will enable selective deposition or growth.

This patterning approach can be said to use a 2D photoresist with virtually no absorptivity requirements as the role of photon absorber and electron generator is played by the substrate. Investigating such methods would provide fundamental insights regarding the influence of the substrate-photoresist interface, options to by-pass the aforementioned challenges related to photoresists' thickness (depth of focus, aspect ratio) and open new opportunities for the patterning of SAMs, SURMOFs and a wide range of other materials.

1.5 Outline and scope of this thesis

Photoresist research, under scrutiny for better performances, focuses mainly on the improvement of existing materials (PAGs, polymer-based resists, metal containing resists). We believe that the investigation of alternative methods and materials can benefit EUVL by providing new insights on EUV triggered mechanisms and reaction pathways, essential for the development of improved photoresists.

In this thesis we report on the investigation of surface anchored metal-organic frameworks (SURMOFs) in EUVL following three main research directions. The first direction investigates the reactivity and performances of SURMOFs used directly as EUV photoresists. The second direction explores a new method for EUVL which uses organic self-assembled monolayers and SURMOFs in a bottom-up approach that contrasts with the traditional top-down approaches. The third direction focuses on the synthesis of SURMOFs with experimental investigations on the influence of the synthetic conditions or the nature of their ligands over the growth of the thin films.

In chapter 2, we investigate the EUV reactivity of two analogous and well-known copper-based SURMOFs, namely copper oxalate and HKUST-1(Cu), via multiple ex-situ spectroscopy techniques. Their respective lithographic capabilities were tested. Copper oxalate showed promising performances while HKUST-1(Cu) remained mostly inert to EUV.
In chapter 3, we propose a new bottom-up approach for EUV lithography using self-assembled monolayers (SAMs) of thiols and surface anchored metal-organic frameworks (SURMOFs). In this method, we use SAM to materialize the patterns in the form of a chemical contrast to enable the subsequent growth of a SURMOF with spatial selectivity.
In chapter 4, we investigate the reactivity of perfluorinated monolayers of thiols on Au substrates towards EUV irradiation by means of in situ photoelectron spectroscopy and total

electron yield measurements. We found that upon EUV exposure, the perfluorinated thiol experience a loss of their fluorine content through bond breakage and desorption of molecular fragments. These experiments were conducted at the IOM-CNR BEAR beamline station at Elettra in Trieste, Italy.

In chapter 5, we study the effect of the nature of the ligand on the growth of analogous SURMOFs, namely X-DMOF-1(Cu) or $Cu_2(X\text{-}BDC)_2(DABCO)$ where BDC = benzene dicarboxylic acid; DABCO = 1,4-diazabicyclo[2.2.2]octane and X symbolizes the functional group attached to the dicarboxylate ligands.

Using layer-by-layer liquid phase epitaxy, we synthesized thin films of DMOF-1(Cu), F-DMOF-1(Cu), Br-DMOF-1(Cu), NH_2-DMOF-1(Cu), F_4-DMOF-1(Cu) (F_4 = 2,3,5,6-tetrafluoro-1,4-benzenedicarboxylic acid), and L_2-DMOF-1(Cu) (L_2 = 2,5-bis(allyloxy)terephthalic acid.). All SURMOFs were grown on gold substrates functionnalised with a carboxyl-terminated SAM of 4-(mercaptomethyl) benzoic acid (MBA) or a pyridyl-terminated SAM of 4-pyridylethyl mercaptan (4pyr). Characterization was conducted by means of PXRD, IRRAS, and SEM.

In chapter 6, we study the effect of the synthetic conditions on the growth of F-DMOF-1(Cu), also known as $Cu_2(F\text{-}BDC)_2(DABCO)$ where F-BDC = 2-fluorobenzene dicarboxylic acid and DABCO = 1,4-diazabicyclo[2.2. 2]octane. The effects of the temperature, concentration of linkers in the synthetic solutions, rinsing procedure and the type of self-assembled monolayer were monitored through a systematic experimental study. PXRD, IRRAS, AFM and SEM were used to characterize the samples.

Bibliography

(1) Kilby, J. S. Invention of the Integrated Circuit. *IEEE Trans. Electron Devices* **1976**, *23* (7), 648–654. https://doi.org/10.1109/T-ED.1976.18467.

(2) Moore, G. Cramming More Components onto Integrated Circuits. *Electronics* **1965**, *38* (8).

(3) IEEE International Roadmap for Devices and Systems™ https://irds.ieee.org (accessed Jan 2, 2020).

(4) ITRS reports http://www.itrs2.net (accessed Jan 2, 2020).

(5) Okoroanyanwu, O. *Chemistry and Lithography*; SPIE Press, 2010.

(6) Lin, B. J. Immersion Lithography and Its Impact on Semiconductor Manufacturing. *J. Micro/Nanolithography, MEMS, MOEMS* **2004**, *3* (3), 377. https://doi.org/10.1117/1.1756917.

(7) Totzeck, M.; Ulrich, W.; Göhnermeier, A.; Kaiser, W. Semiconductor Fabrication: Pushing Deep Ultraviolet Lithography to Its Limits. *Nat. Photonics* **2007**, *1* (11), 629–631. https://doi.org/10.1038/nphoton.2007.218.

(8) ASML. The semiconductor industry workhorses. https://www.asml.com/en/products/duv-lithography-systems (accessed Dec 1, 2020).

(9) Samsung Electronics Begins Mass Production at New EUV Manufacturing Line http://bit.ly/38Gw9oA (accessed Jan 2, 2020).

(10) Torok, J.; Del Re, R.; Herbol, H.; Das, S.; Bocharova, I.; Paolucci, A.; Ocola, L. E.; Ventrice, C.; Lifshin, E.; Denbeaux, G.; Brainard, R. L. Secondary Electrons in EUV Lithography. *J. Photopolym. Sci. Technol.* **2013**, *26* (5), 625–634. https://doi.org/10.2494/photopolymer.26.625.

(11) Closser, K. D.; Ogletree, D. F.; Naulleau, P.; Prendergast, D. The Importance of Inner-Shell Electronic Structure for Enhancing the EUV Absorption of Photoresist Materials. *J. Chem. Phys.* **2017**, *146* (16), 1–13. https://doi.org/10.1063/1.4981815.

(12) MacDonald, S. A.; Willson, C. G.; Fréchet, J. M. J. Chemical Amplification in High-Resolution Imaging Systems. *Acc. Chem. Res.* **1994**, *27* (6), 151–158. https://doi.org/10.1021/ar00042a001.

(13) Manouras, T.; Argitis, P. High Sensitivity Resists for EUV Lithography: A Review of Material Design Strategies and Performance Results. *Nanomaterials* **2020**, *10* (8), 1–24. https://doi.org/10.3390/nano10081593.

(14) Henke, B. L.; Gullikson, E. M.; Davis, J. C. X-Ray Interactions: Photoabsorption, Scattering, Transmission, and Reflection at E = 50-30,000 eV, Z = 1-92. *At. Data Nucl. Data Tables* **1993**, *54* (2), 181–342. https://doi.org/10.1006/adnd.1993.1013.

(15) Fallica, R.; Haitjema, J.; Wu, L.; Castellanos, S.; Brouwer, F.; Ekinci, Y. Absorption coefficient of metal-containing photoresists in the extreme ultraviolet. *J.*

Micro/Nanolithography, MEMS, MOEMS, **2018**, 17(2), 023505. https://doi.org/10.1117/1.JMM.17.2.023505

(16) Narasimhan, A.; Wisehart, L.; Grzeskowiak, S.; Ocola, L. E.; Denbeaux, G.; Brainard, R. L. What We Don't Know About EUV Exposure Mechanisms. *J. Photopolym. Sci. Technol.* **2017**, *30* (1), 113–120. https://doi.org/10.2494/photopolymer.30.113.

(17) Wood, O. R. EUVL: Challenges to Manufacturing Insertion. *J. Photopolym. Sci. Technol.* **2017**, *30* (5), 599–604. https://doi.org/10.2494/photopolymer.30.599.

(18) Xu, H.; Kosma, V.; Giannelis, E.; Ober, C. K.; Sakai, K. EUV Photolithography: Resist Progress and Challenges. *Proc. SPIE*, **2018**; p 2. https://doi.org/10.1117/12.2302759.

(19) Levinson, H. J.; Brunner, T. A. Current Challenges and Opportunities for EUV Lithography. *Proc. SPIE*, **2018**; p 2. https://doi.org/10.1117/12.2502791.

(20) Li, L.; Liu, X.; Pal, S.; Wang, S.; Ober, C. K.; Giannelis, E. P. Extreme Ultraviolet Resist Materials for Sub-7 nm Patterning. *Chem. Soc. Rev.* **2017**, *46* (16), 4855–4866. https://doi.org/10.1039/c7cs00080d.

(21) Vesters, Y.; De Simone, D.; De Gendt, S. Influence of Post Exposure Bake Time on EUV Photoresist RLS Trade-Off; *Proc. SPIE*; **2017**; p 1014324. https://doi.org/10.1117/12.2257910.

(22) Haitjema, J.; Zhang, Y.; Vockenhuber, M.; Kazazis, D.; Ekinci, Y.; Brouwer, A. M. Extreme Ultraviolet Patterning of Tin-Oxo Cages. *J. Micro/Nanolithography, MEMS, MOEMS* **2017**, *16* (03), 1. https://doi.org/10.1117/1.jmm.16.3.033510.

(23) Bilski, B.; Zimmermann, J.; Roesch, M.; Liddle, J.; van Setten, E.; Bottiglieri, G.; van Schoot, J. High-NA EUV Imaging: Challenges and Outlook. *Proc. SPIE;* **2019**; p 42. https://doi.org/10.1117/12.2536329.

(24) Zahlten, C.; Gräupner, P.; van Schoot, J.; Kuerz, P.; Stoeldraijer, J.; Kaiser, W. High-NA EUV Lithography: Pushing the Limits. *Proc. SPIE;* **2019**; p 43. https://doi.org/10.1117/12.2536469.

(25) Li, H.; Addaoudi, M.; O'Keeffe, M.; Yaghi, O. M. Design and Synthesis of an Exceptionally Stable and Highly Porous Metal-Organic Framework. *Nature* **1999**, *402*, 276–279.

(26) Yuan, S.; Feng, L.; Wang, K.; Pang, J.; Bosch, M.; Lollar, C.; Sun, Y.; Qin, J.; Yang, X.; Zhang, P.; Wang, Q.; Zou, L.; Zhang, Y.; Zhang, L.; Fang, Y.; Li, J.; Zhou, H. C. Stable Metal–Organic Frameworks: Design, Synthesis, and Applications. *Adv. Mater.* **2018**, *30* (37), 1–35. https://doi.org/10.1002/adma.201704303.

(27) Furukawa, H.; Cordova, K. E.; O'Keeffe, M.; Yaghi, O. M.; O'Keeffe, M.; Yaghi, O. M.; O'Keeffe, M.; Yaghi, O. M. The Chemistry and Applications of Metal-Organic Frameworks. *Science.* **2013**, *341* (6149). https://doi.org/10.1126/science.1230444.

(28) Cook, T. R.; Zheng, Y. R.; Stang, P. J. Metal-Organic Frameworks and Self-Assembled Supramolecular Coordination Complexes: Comparing and Contrasting

the Design, Synthesis, and Functionality of Metal-Organic Materials. *Chem. Rev.* **2013**, *113* (1), 734–777. https://doi.org/10.1021/cr3002824.

(29) Moghadam, P. Z.; Li, A.; Wiggin, S. B.; Tao, A.; Maloney, A. G. P.; Wood, P. A.; Ward, S. C.; Fairen-Jimenez, D. Development of a Cambridge Structural Database Subset: A Collection of Metal-Organic Frameworks for Past, Present, and Future. *Chem. Mater.* **2017**, *29* (7), 2618–2625. https://doi.org/10.1021/acs.chemmater.7b00441.

(30) Moosavi, S. M.; Nandy, A.; Jablonka, K. M.; Ongari, D.; Janet, J. P.; Boyd, P. G.; Lee, Y.; Smit, B.; Kulik, H. J. Understanding the Diversity of the Metal-Organic Framework Ecosystem. *Nat. Commun.* **2020**, *11* (1), 1–10. https://doi.org/10.1038/s41467-020-17755-8.

(31) Gu, Z. G.; Zhang, J. Epitaxial Growth and Applications of Oriented Metal–Organic Framework Thin Films. *Coord. Chem. Rev.* **2019**, *378*, 513–532. https://doi.org/10.1016/j.ccr.2017.09.028.

(32) Heinke, L.; Tu, M.; Wannapaiboon, S.; Fischer, R. A.; Wöll, C. Surface-Mounted Metal-Organic Frameworks for Applications in Sensing and Separation. *Microporous Mesoporous Mater.* **2014**, *216*, 200–215. https://doi.org/10.1016/j.micromeso.2015.03.018.

(33) Urquhart, J. World's First Commercial MOF Keeps Fruit Fresh. *Chemistry World*. September 27, 2016.

(34) Frameworks for Commercial Success. *Nat. Chem.* **2016**, *8* (11), 987–987. https://doi.org/10.1038/nchem.2661.

(35) Luo, C.; Xu, C.; Lv, L.; Li, H.; Huang, X.; Liu, W. Review of Recent Advances in Inorganic Photoresists. *RSC Adv.* **2020**, *10* (14), 8385–8395. https://doi.org/10.1039/c9ra08977b.

(36) Begum, S.; Hassan, Z.; Bräse, S.; Tsotsalas, M. Polymerization in MOF-Confined Nanospaces: Tailored Architectures, Functions, and Applications. *Langmuir* **2020**, *36* (36), 10657–10673. https://doi.org/10.1021/acs.langmuir.0c01832.

(37) Takayanagi, M.; Pakhira, S.; Nagaoka, M. Control of Diffusion and Conformation Behavior of Methyl Methacrylate Monomer by Phenylene Fin in Porous Coordination Polymers. *J. Phys. Chem. C* **2015**, *119* (49), 27291–27297. https://doi.org/10.1021/acs.jpcc.5b09332.

(38) Xie, M.; Prasetya, N.; Ladewig, B. P. Systematic Screening of DMOF-1 with NH_2, NO_2, Br and Azobenzene Functionalities for Elucidation of Carbon Dioxide and Nitrogen Separation Properties. *Inorg. Chem. Commun.* **2019**, *108*, 107512. https://doi.org/10.1016/j.inoche.2019.107512.

(39) Ulman, A. Formation and Structure of Self-Assembled Monolayers. *Chem. Rev.* **1996**, *96* (4), 1533–1554. https://doi.org/10.1021/cr9502357.

(40) Gooding, J. J.; Mearns, F.; Yang, W.; Liu, J. Self-Assembled Monolayers into the 21st Century: Recent Advances and Applications. *Electroanalysis* **2003**, *15* (2), 81–96. https://doi.org/10.1002/elan.200390017.

(41) Shekhah, O. Layer-by-Layer Method for the Synthesis and Growth of Surface Mounted Metal-Organic Frameworks (SURMOFs). *Materials.* **2010**, *3* (2), 1302–1315. https://doi.org/10.3390/ma3021302.

(42) Grytz, C. M.; Farr, F.; Kind, M.; Terfort, A.; Tussupbayev, S.; Zhuang, J.-L.; Diefenbach, M.; Holthausen, M. C. Insight into the Oriented Growth of Surface-Attached Metal–Organic Frameworks: Surface Functionality, Deposition Temperature, and First Layer Order. *J. Am. Chem. Soc.* **2015**, *137* (25), 8237–8243. https://doi.org/10.1021/jacs.5b03948.

(43) Baralia, G. G.; Duwez, A. S.; Nysten, B.; Jonas, A. M. Kinetics of Exchange of Alkanethiol Monolayers Self-Assembled on Polycrystalline Gold. *Langmuir* **2005**, *21* (15), 6825–6829. https://doi.org/10.1021/la050245v.

(44) Schlenoff, J. B.; Li, M.; Ly, H. Stability and Self-Exchange in Alkanethiol Monolayers. *J. Am. Chem. Soc.* **1995**, *117* (50), 12528–12536. https://doi.org/10.1021/ja00155a016.

(45) Frey, S.; Heister, K.; Zharnikov, M.; Grunze, M. Modification of Semifluorinated Alkanethiolate Monolayers by Low Energy Electron Irradiation. *Phys. Chem. Chem. Phys.* **2000**, *2* (9), 1979–1987. https://doi.org/10.1039/a910314g.

(46) Yildirim, C.; Füser, M.; Terfort, A.; Zharnikov, M. Modification of Aromatic Self-Assembled Monolayers by Electron Irradiation: Basic Processes and Related Applications. *J. Phys. Chem. C* **2017**, *121* (1), 567–576. https://doi.org/10.1021/acs.jpcc.6b11269.

(47) Harnett, C. K.; Satyalakshmi, K. M.; Craighead, H. G. Low-Energy Electron-Beam Patterning of Amine-Functionalized Self-Assembled Monolayers. *Appl. Phys. Lett.* **2000**, *76* (17), 2466–2468. https://doi.org/10.1063/1.126378.

(48) Zharnikov, M.; Frey, S.; Heister, K.; Grunze, M. Modification of Alkanethiolate Monolayers by Low Energy Electron Irradiation: Dependence on the Substrate Material and on the Length and Isotopic Composition of the Alkyl Chains. *Langmuir* **2000**, *16* (6), 2697–2705. https://doi.org/10.1021/la991034r.

(49) Zhuang, J. L.; Terfort, A.; Wöll, C. Formation of Oriented and Patterned Films of Metal-Organic Frameworks by Liquid Phase Epitaxy: A Review. *Coord. Chem. Rev.* **2016**, *307*, 391–424. https://doi.org/10.1016/j.ccr.2015.09.013.

(50) Szymonik, M.; Davies, A. G.; Walti, C. DNA Self-Assembly-Driven Positioning of Molecular Components on Nanopatterned Surfaces. *Nanotechnology* **2016**, *27* (39). https://doi.org/10.1088/0957-4484/27/39/395301.

(51) Shaali, M.; Woller, J. G.; Johansson, P. G.; Hannestad, J. K.; De Battice, L.; Aissaoui, N.; Brown, T.; El-Sagheer, A. H.; Kubatkin, S.; Lara-Avila, S.; Albinsson, B.; Jesorka, A. Site-Selective Immobilization of Functionalized DNA Origami on Nanopatterned Teflon AF. *J. Mater. Chem. C* **2017**, *5* (30), 7637–7643. https://doi.org/10.1039/c7tc01015j.

(52) Lee, S. H.; Rho, W.-Y.; Park, S. J.; Kim, J.; Kwon, O. S.; Jun, B.-H. Multifunctional Self-Assembled Monolayers via Microcontact Printing and Degas-Driven Flow

Guided Patterning. *Sci. Rep.* **2018**, *8* (1), 16763. https://doi.org/10.1038/s41598-018-35195-9.

(53) Yang, J.; Ichii, T.; Murase, K.; Sugimura, H. Site-Selective Assembly and Reorganization of Gold Nanoparticles along Aminosilane-Covered Nanolines Prepared on Indium-Tin Oxide. *Langmuir* **2012**, *28* (20), 7579–7584. https://doi.org/10.1021/la301042y.

(54) Wang, N.; Cheng, L.; Si, J.; Liang, X.; Jin, Y.; Wang, J.; Huang, W. Morphology Control of Perovskite Light-Emitting Diodes by Using Amino Acid Self-Assembled Monolayers. *Appl. Phys. Lett.* **2016**, *108* (14). https://doi.org/10.1063/1.4945330.

(55) Kim, G.; An, S.; Hyeong, S. K.; Lee, S. K.; Kim, M.; Shin, N. Perovskite Pattern Formation by Chemical Vapor Deposition Using Photolithographically Defined Templates. *Chem. Mater.* **2019**, *31* (19), 8212–8221. https://doi.org/10.1021/acs.chemmater.9b03155.

(56) Castellanos, S.; Verhoeven, J.; Frenken, J.; Antonov, P.; Ten Kate, N.; Lugier, O. Method and Apparatus for Forming a Patterned Layer of Carbon, Method of Forming a Patterned Layer of Material. WO 2019/166409 A1, 2019.

Chapter 2

Copper-Based SURMOFs as Photoresists for EUV Lithography*

Abstract

The ever-growing consumer demand for more powerful technological devices compels the semiconductor industry to regularly upgrade nanolithography techniques. Yet, currently, the development of photoresists for extreme ultraviolet lithography (EUVL), the emerging nanopatterning technology, is hindered by the lack of fundamental understanding of photoresist-photon and photoresist-electron interactions.

In this work, we explore the EUV reactivity of two copper-based surface-anchored metal-organic frameworks (SURMOFs), a type of hybrid material that shares relevant properties with promising metal-containing resists called metal oxo clusters (MOCs), but have remained untested for EUVL. Samples of $Cu(C_2O_4)•nH_2O$ and HKUST-1(Cu) were exposed to EUV and their reactivity characterised by means of x-ray photoelectron spectroscopy, atomic force microscopy and infrared reflection absorption spectroscopy.

We observe high sensitivity and promising patterning performances for $Cu(C_2O_4)•nH_2O$ with a threshold for solubility switch at 10 mJ/cm^2, as opposed to HKUST-1(Cu) which remained practically inert under EUV doses as high as 250 mJ/cm^2. We highlighted the prominence of favorable dissociative mechanisms over raw absorptivity for better performances and commented on the opportunities brought by metal-organic frameworks, through their exceptional tunability, to further our understanding of the radiative processes triggered by EUV in photoresists.

* Lugier, O.; Amairi, M.N.; Martin, F.; Castellanos, S.; "Copper-based SURMOFS as photoresists for EUV lithography"; manuscript in preparation.

2.1 Introduction

The semiconductor industry is under constant pressure to improve the performances of nanolithography, the technology that enables the fabrication of central processing units (CPUs), essential to computers and technological devices. Common CPUs contain billions of nm-scale transistors embedded in intricate circuitry to provide computing power to a device. Because adding more transistors to a CPU increases its performance, many nanolithography methods have been developed over the years to continuously downscale transistors' dimensions and keep up with Moore's Law, the economic prediction that the semiconductor industry adopted as roadmap.[1,2]

Now, in order to continue downscaling transistors at such pace, a better fundamental understanding of extreme ultraviolet lithography (EUVL) is required. In particular for the physico-chemical processes occurring in the photoresists, the photosensitive materials that transform the images projected with EUV light into nanopatterns. For this, more experimental data are needed to build and refine models to improve existing lithographic methods and anticipate future hurdles.[3–6]

The previous generations of organic resists, comprising polymeric platforms and photoacids, might be replaced by metal-containing materials.[7–9] Metallic atoms have higher EUV photon-absorption cross-sections than the light atoms commonly found in organic materials. This leads to improved sensitivity, decreased stochastics in the patterning process and, therefore, increased pattern quality.[10,11] Regardless of the type of photoresist, their complexity and diversity make it difficult to form a general theory on EUV-induced chemistry, while the peculiar conditions in which EUV exposure occurs make experimental studies very challenging with a limited number of available *in-situ* analysis techniques.[12,13]

While molecular versions of metal-containing resists are currently studied by the EUV community,[14] metal-organic frameworks (MOFs), an analogous type of organic-inorganic materials, have remained untested for EUVL. MOFs are composed of inorganic clusters, mostly metal oxo clusters, linked to each other by organic linkers forming 1D, 2D or, mainly, 3D structures. They are extensively studied in other fields of material science for their diverse properties (porosity, conductivity, tuneability, polarizability, fluorescence, *etc*.) by researchers and industrials alike, as they try to integrate MOFs into devices meant for various applications such as gas storage/purification, sensors, water capture, electronics, *etc*.[15–17]

Metal-organic frameworks are mainly synthesised as monocrystals or powders but can also be grown directly on a substrate as a so-called surface-mounted metal-organic frameworks (SURMOFs). SURMOFs are usually chemically bonded to the surface of the substrate

through self-assembled monolayers (SAMs) and are set to enable the production of a wide array of MOF-containing devices and surface coatings.

These materials could be portrayed as porous, crystalline and low-density metal-containing resists, in which nodes comprising metal-oxo clusters are coordinated by linkers with more than one coordinating site (multitopic) in well-defined directions and with a long-range periodicity. Motivated by the pre-ordered character of MOFs combined with their chemical similarities to other metal-containing resists, we investigated the structural and chemical changes triggered by the EUV exposure of two well-known copper-based MOFs, namely Copper Oxalate or $Cu(C_2O_4)•nH_2O$[18] and Cu_3(benzene-1,3,5-tricarboxylate)$_2$ or HKUST-1(Cu).[19] Specifically, we monitored the effect of EUV radiation on SURMOFs of these two prototypical materials via atomic force microscopy (AFM), scanning electron microscopy (SEM), infrared reflection absorption spectroscopy (IRRAS) and X-Ray photoelectron spectroscopy (XPS).

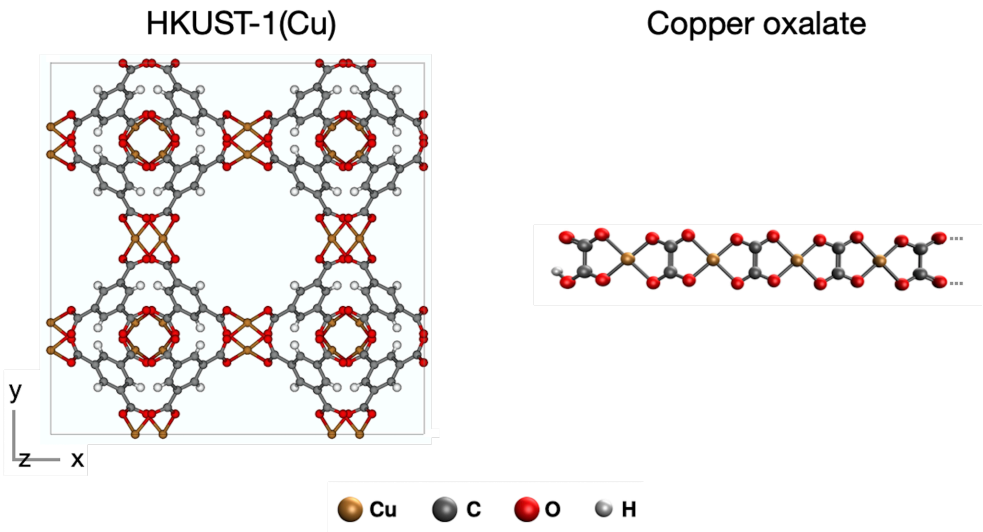

Figure 2.1: Comparison of the unit cell of HKUST-1(Cu) (left) and the structure of copper oxalate (right). The water molecules potentially coordinating the apical positions of the copper atoms are omitted.

The two MOFs were chosen for their related chemical compositions. They share the same metal atom and their linkers, oxalate for $Cu(C_2O_4)•nH_2O$ and benzene-1,3,5-tricarboxylate (also known as trimesate or BTC) for HKUST-1(Cu), use carboxylates (COO^-) as coordinating groups. However, these materials also offer significant differences in their crystalline structures. Benzene-1,3,5-tricarboxylate has three coordinating groups (tritopic), providing HKUST-1(Cu) with a massive free volume from pores of different sizes and a

much more complex structure than $Cu(C_2O_4)•nH_2O$, composed of ditopic linear oxalate linkers (Fig. 2.1). We anticipated these similarities and differences to help determining the origin of some EUV-triggered mechanisms and general reactivity trends.

To the best of our knowledge, this is the first investigation of the reactivity of a 3D metal-organic frameworks towards EUV light. This study aims at widening the scope of EUV research towards new concepts to improve photoresists performances and the fundamental understanding of EUV-induced chemistry in inorganic-organic hybrid systems.

2.2 Experimental

2.2.1 Sample preparation

Sputtering and thiol functionalisation

Polycrystalline gold surfaces were prepared by sputter coating (Leica EM ACE600) clean silicon substrates with an adhesion layer of chromium (5 nm) followed by a layer of gold (50 nm). The functionalization of the gold surfaces was conducted by immersion in an ethanol solution of 4-mercaptomethylbenzoic acid (MBA) at a concentration of 1 mM during 24h.

SURMOF growth

SURMOFs were grown using layer-by-layer Liquid Phase Epitaxy performed with a homemade automatized system composed of a mechanical arm that successively dips a sample holder into beakers with control over the temperature, time of immersion, stirring and sonication. Up to six samples can be subjected to the synthetic procedure at the same time, allowing for simultaneous growth and good reproducibility.

A growth cycle for HKUST-1(Cu) consists of 15 minutes of immersion in a 1 mM ethanol solution of copper acetate hexahydrate ($Cu(OAc)_2•6H_2O$), 3 minutes of rinsing in pure ethanol, 30 minutes of immersion in a 0.2 mM ethanol solution of trimesic acid (TMA) and 3 minutes of rinsing in pure ethanol. Sonication (80 Hz) was applied during the rinsing steps. Samples went through 15 to 20 cycles of growth depending on the thickness required.
A growth cycle for $Cu(C_2O_4)•nH_2O$ consists of 30 minutes of immersion in a 1 mM ethanol solution of copper acetate hexahydrate ($Cu(OAc)_2•6H_2O$), 2 minutes of rinsing in pure ethanol, 60 minutes of immersion in a 0.2 mM ethanol solution of oxalic acid, 2 minutes of rinsing in pure ethanol. Sonication (80 Hz) was applied during the rinsing steps. Samples went through 15 to 20 cycles of growth depending on the thickness required.

2.2.2 EUV exposures

EUV exposures were performed at the XIL-II beamline at the Swiss Light Source (SLS) synchrotron in the Paul Scherrer Institute (PSI).[20] The open frame exposures exposed pads with areas of 1.7 × 1.7 mm^2 (pinhole 70 µm) or 0.5 × 0.5 mm^2 (pinhole 30 µm) with different doses.

2.2.3 Sample characterisation

Atomic Force Microscopy (AFM)

AFM images were acquired in contact mode in air on a Bruker Scan Assist AFM using the silicon nitride Bruker ScanAsyst-Air tips. The images were treated using the software Nanoscope Analysis version 2.0.

Scanning Electron Microscopy (SEM)

SEM images were taken using a FEI VERIOS 460 scanning electron microscope using 5 keV electrons and a beam current of 100 pA.

Infrared Reflection Absorption Spectroscopy (IRRAS)

IRRAS spectra were acquired using the Bruker A513/Q variable angle reflection accessory on a FT-IR spectrometer Bruker Vertex 80v at an angle of 70° (more grazing angle could not be used due to limitations in the set-up and the dimension of the samples). The incident light was not polarized.

X-Ray photoelectron spectroscopy (XPS)

XPS spectra were acquired using a Scienta Omicron HiPP-3 analyzer and a monochromatic Al Kα source operating at 20 mA emission current with a pass energy of 100 eV. Data analysis and quantification were performed using the Unifit software version 2018.

Quartz crystal microbalance (QCM)

An INFICON Research Quartz Crystal Microbalance (RQCM) with 1-inch INFICON Research Crystals was used for studies on dissolution rates. SURMOFs were grown selectively on the active side of the quartz crystals (QCs) using LPE after selective thiol functionalisation of the QCs. The inactive side was thoroughly washed prior to measurement with a concentrated EDTA solution, acetone, ethanol and water. The QCs were immersed from air directly into the developer using a homemade automatic dipping arm. The developer was an aqueous solution of EDTA and NaOH. Two concentrations of EDTA and NaOH were used: 1 / 2 mM and 0.1 / 0.2 mM.

Development tests (on EUV-exposed samples)

Exposed SURMOF films were developed by immersion in aqueous solutions of EDTA and NaOH (0.1 / 0.2 mM) for 60 seconds for $Cu(C_2O_4)•nH_2O$ and 20 seconds for HKUST-1(Cu).

2.3 Results

EUV exposures

Thin films of $Cu(C_2O_4)•nH_2O$ and HKUST-1(Cu) grown by liquid phase epitaxy (LPE)[21] proved to be continuous layers, with thickness values around 50 nm and 30 nm, respectively, according to scanning electron microscopy (SEM) and atomic force microscopy (AFM) images taken prior to the EUV exposures. However, the morphology of each MOF was clearly different; $Cu(C_2O_4)•nH_2O$ was composed of clustered needle-shaped crystals while HKUST-1(Cu) films were composed of densely packed cubic crystallites (Fig. 2.2).

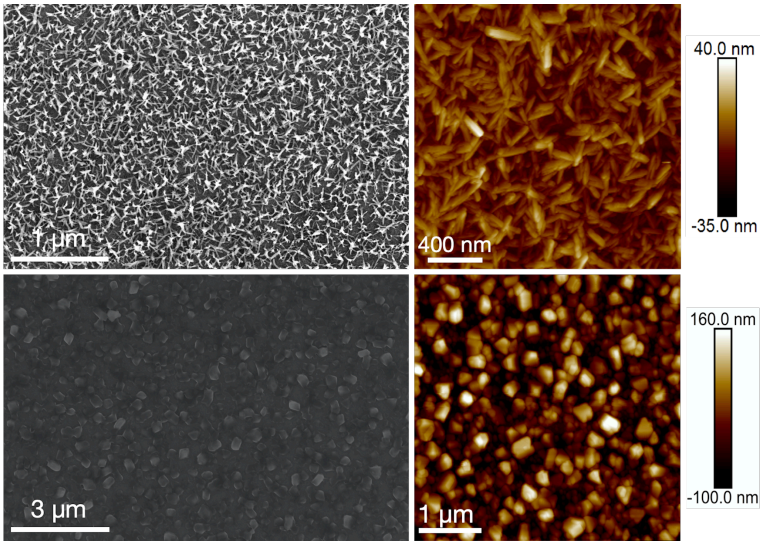

Figure 2.2: SEM (left) and AFM images (right) of SURMOF of $Cu(C_2O_4)•nH_2O$ (top) and HKUST-1(Cu) (bottom).

The SURMOFs thin films were exposed to EUV light in pattern-free square-shaped areas in order to facilitate the chemical analysis of the exposed material. Two types of experiments were performed: a) a multidose exposure to find dose thresholds for compression or changes in solubility rates; b) exposure of the whole sample area for spectroscopic analysis. The dose matrix for multi-dose patterning is shown Table 2.1. After the doses of interest were determined from the first set of multi-dose experiments, the wide-area exposures were

conducted at 25 mJ/cm^2, 75 mJ/cm^2, 150 mJ/cm^2, or 500 mJ/cm^2 on $Cu(C_2O_4)•nH_2O$ and at 250 mJ/cm^2 or 1000 mJ/cm^2 on HKUST-1(Cu).

***Table 2.1**: Dose matrix for the multi dose exposures of 0.5 mm × 0.5 mm pads.*

Multi-dose matrix (mJ/cm^2)		
2	5	10
15	25	50
75	100	150
250	500	1000

SEM imaging (Fig. S2.1 in Supporting Information) on $Cu(C_2O_4)•nH_2O$ samples shows contrast between exposed (darker) and unexposed (brighter) areas. Whether these differences in brightness arise from different work functions due to changes in the films or other effects (density, changes in electron scattering cross-sections, *etc*.) cannot be discriminated. Yet, the contrast in SEM indicates that the exposed areas underwent chemical reactions upon EUV irradiation. For HKUST-1(Cu), no difference is seen in such conditions. These observations are the first hint at differences in EUV reactivity between the two SURMOFs.

X-ray photoelectron spectroscopy (XPS)

XPS was used to monitor the chemical changes triggered by EUV and determine the SURMOFs' reactivity at various doses. The C 1s spectrum of unexposed $Cu(C_2O_4)•nH_2O$ (Fig. 2.3d) presents two main components at 285 eV and 289 eV. The former is expected to have a strong contribution from adventitious carbon or potential unreacted copper acetate moieties and was dismissed in the monitoring of chemical changes. The latter is attributed to the carboxylate groups of the oxalate ligand. A third minor component at 287 eV, usually attributed to C-O moieties, was considered negligible for our study. The Cu $2p_{3/2}$ region of $Cu(C_2O_4)•nH_2O$ (Fig. 2.3c) displays three main components detected at 930.5 eV and 932 eV, both assigned to Cu-species with oxidation states lower than 2+, and at 934 eV, assigned to Cu^{2+}. Multiple Cu^{2+} satellite peaks are observed between 929 eV and 939 eV and a weak contribution from multiplet splitting is detected at 936.5 eV.[22] The presence of copper atoms in low oxidation states in pristine samples is a known occurrence for copper-based MOFs. This phenomenon can be caused by synthesis defects, contamination or X-Ray-induced damages during XPS analysis.[23,24]

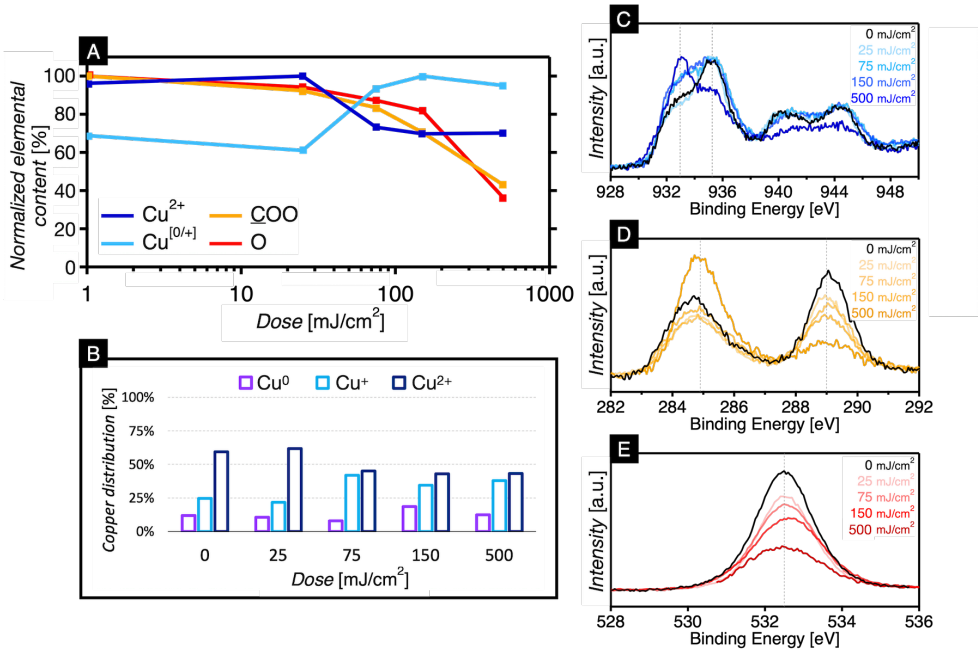

Figure 2.3: (A) Elemental content of $Cu(C_2O_4)•nH_2O$ as a function of the EUV dose. $Cu^{[0/+]}$ represents the combined concentrations of copper species in lower oxidation states. The species ratio at each dose was normalized to the ratio in the pristine material, except for the Cu species appearing during irradiation. **(B)** Copper distribution in $Cu(C_2O_4)•nH_2O$ as a function of the EUV dose. **(C), (D)** and **(E)** Stacked XPS spectra of the Cu $2p_{3/2}$, C 1s and O 1s regions, respectively, of $Cu(C_2O_4)•nH_2O$ exposed at various EUV doses. Dotted lines are set at 933.0 eV and 935.2 eV in **(C)**, 284.9 eV and 289.0 eV in **(D)** and 532.5 eV in **(E)**.

Finally, the O 1s region (Fig. 2.3e) shows three components at 534 eV, 532.5 eV and 531 eV, assigned to H_2O/OH, carbonates and O-Cu, respectively. The entirety of the O 1s envelop is considered for oxygen content monitoring. (Fig. 2.3c, 2.3d, 2.3e and Fig. S2.2 in Supporting Information).

Because our XPS is lacking a mapping option, each measurement of distinct doses was performed on a different sample exposed to EUV over its whole area. Therefore, the fitting values are normalised twice. First to the total copper content of each sample, to correct for potential artefacts that could arise from slight differences in measurement conditions. Then, the obtained C/Cu or O/Cu ratios are normalised again, either to the corresponding ratio in the pristine sample (for decreasing concentrations) or in the sample with the highest concentration of the element of interest (for increasing concentrations). From these ratios, we can estimate the increase or decrease percentage for the concentration of each species in the SURMOF at every EUV dose tested.

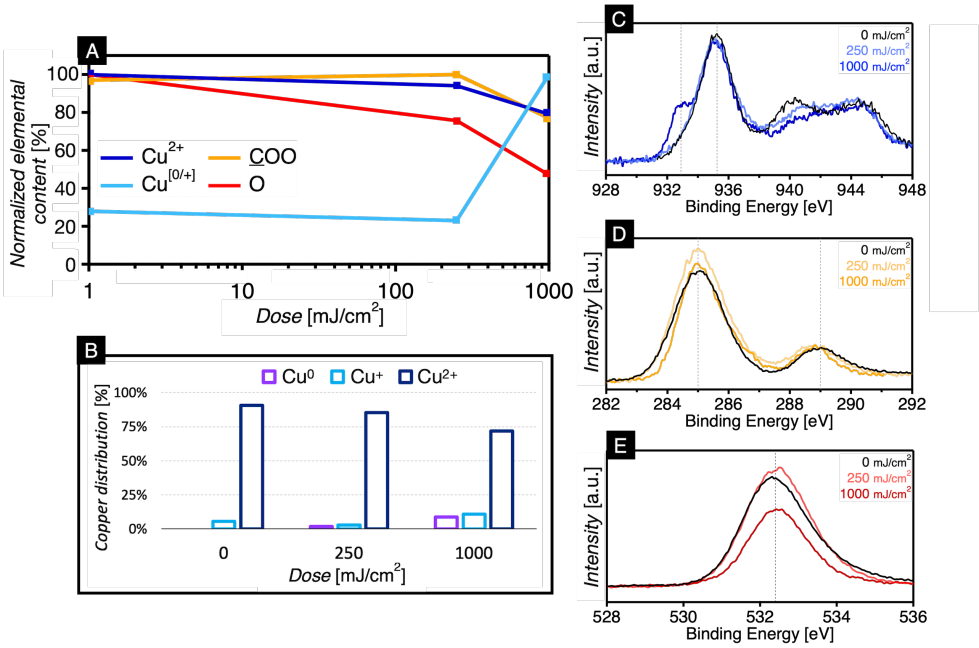

Figure 2.4: (A) Elemental content of HKUST-1(Cu) as a function of the EUV dose. $Cu^{[0/+]}$ represents the combined concentrations of copper species in lower oxidation states. The species ratio at each dose was normalized to the ratio in the pristine material, except for the Cu species appearing during irradiation. **(B)** Copper distribution in HKUST-1(Cu) as a function of the EUV dose. **(C), (D)** and **(E)** Stacked XPS spectra of the Cu $2p_{3/2}$, C 1s and O 1s regions, respectively, of HKUST-1(Cu) exposed at various EUV doses. Dotted lines are set at 933.0 eV and 935.2 eV in **(C)**, 285 eV and 289.0 eV in **(D)** and 932.5 eV in **(E)**.

From these fittings, we observe a gradual decrease of the concentrations of Cu^{2+} (934 eV), COO (289 eV) and O (532 eV) for increasing EUV doses. Simultaneously, the contributions of the reduced copper species (930.5 eV and 932 eV) are increased. These observations reveal that decarboxylation occurs with CO_2, or CO, molecules desorbing from the thin film while the Cu^{2+} ions are reduced to lower oxidation states upon exposure (Fig. 2.3b). At 500 mJ/cm^2, the highest dose tested for $Cu(C_2O_4)\bullet nH_2O$, *ca.* 30% of the Cu^{2+} of the SURMOF are reduced while *ca.* 55% of the COO moieties and 65% of the oxygen desorb. (Fig. 2.3a).

The XPS spectra of the C 1s, Cu $2p_{3/2}$ and O 1s regions of HKUST-1(Cu) have the same components than $Cu(C_2O_4)\bullet nH_2O$ as expected from their analogous elemental compositions (Fig. 2.4c, 2.4d, 2.4e and Fig. S2.3 in Supporting Information). Upon EUV exposure, a similar spectral evolution is observed in HKUST-1(Cu), although higher doses are required to reach comparable results. We observe a decrease in the concentrations of COO (289 eV), O (532.5 eV) and Cu^{2+} (934 eV) in favour of an increase of Cu in lower oxidation states (932

eV and 931.5 eV). At a dose of 1000 mJ/cm^2, the highest dose tested for HKUST-1(Cu), 25% of the carboxylates and 55% of the oxygen has desorbed (Fig. 2.4a) while *ca.* 20% of the Cu^{2+} are reduced to Cu ions in lower oxidation states (Fig. 2.4b).

IRRAS analysis

Similarly to XPS studies, we performed IRRAS measurements on thin films of $Cu(C_2O_4)•nH_2O$ and HKUST-Cu(1) before and after EUV irradiation, using one sample for each dose.

$Cu(C_2O_4)•nH_2O$ samples show a decrease in the intensities of the asymmetric COO stretching mode, ν_{as}COO at 1650 cm^{-1}, and the OH stretching mode, νOH at 3200 cm^{-1}, for increasing EUV doses (Fig. 2.5). In addition, ν_{as}COO gradually red-shifts from 1650 cm^{-1} in pristine samples to 1625 cm^{-1} after a 150 mJ/cm^2 irradiation. The other characteristic vibrational modes, namely the symmetric stretching vibrations of C-O, ν_sC-O at 1400 cm^{-1} and 1300 cm^{-1}, and δ(COO) at 825 cm^{-1}, the asymmetric deformation of the COO group, possibly coupled with some Cu-O stretching modes ν(Cu-O), are all too weak to enable accurate gauging of a trend.

We assume the significant attenuation of the symmetric vibrational modes to be caused by the orientation of the carboxylate linkers of the SURMOF. We deduce from the different intensities that the C-C bond of the oxalate linkers is in a plane parallel to the surface while the carboxylate groups are in a plane perpendicular to the surface. This echoes with the AFM micrographs (Fig. 2.2) that show most of the $Cu(C_2O_4)•nH_2O$ needles lying flat on the substrate, instead of randomly angled, suggesting a homogeneous crystalline orientation. See section 6.3.2 (chapter 6) of this thesis, or previous IRRAS studies of on pillar-layer SURMOFs, for more details.[25–27]

In line with the XPS results, IRRAS analysis on HKUST-1(Cu) samples only reveals small differences between pristine and exposed samples (Fig. 2.5). The spectra are normalised to the intensity of the symmetric stretching mode of -CO_2, ν_sCOO at 1450 cm^{-1}. Following EUV exposure, we observe a decrease in the intensity of the symmetric and asymmetric stretching modes of COO at 1650 cm^{-1} and 1380 cm^{-1}, respectively, suggesting that decarboxylation occurs during EUV exposure, as previously observed from XPS results. The absorption band associated to ν_sCOO at 1380 cm^{-1} gets slightly blue-shifted (+ 5 cm^{-1}) while the other ν_sCOO band at 1450 cm^{-1} is unaffected regardless of the dose.

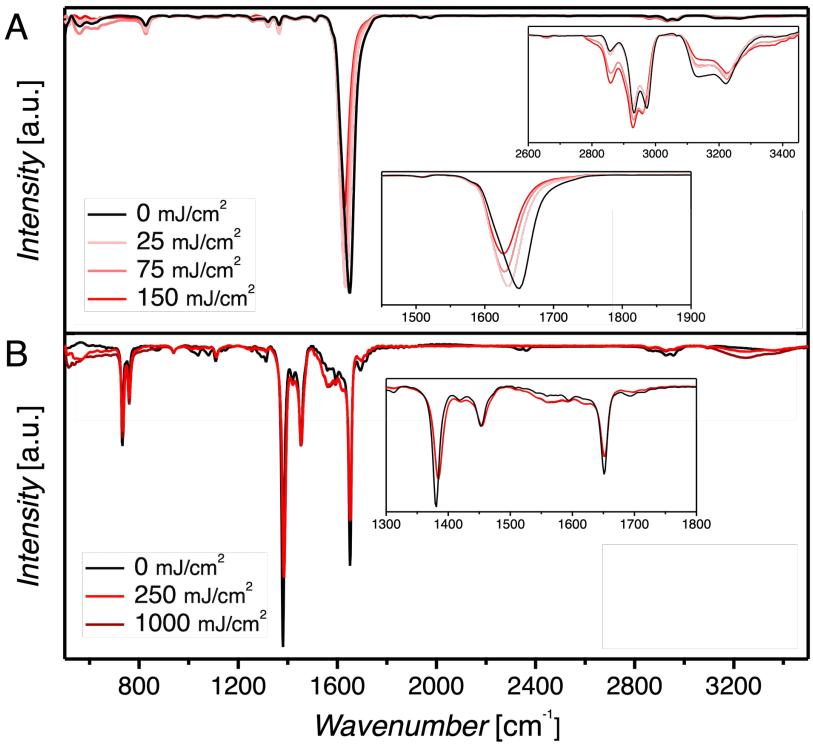

Figure 2.5: IRRAS spectra of SURMOFs of **(A)** $Cu(C_2O_4)•nH_2O$ and **(B)** HKUST-1(Cu) exposed to EUV at various doses.

The intensity of the broad band detected between 1525 cm^{-1} and 1625 cm^{-1} increases. This band has contributions from mixed $[Cu_2(BTC)_2Ac_2]$ clusters and free copper acetate clusters potentially trapped in the material's pores. It is tempting to attribute these changes to EUV-induced structural disorder in the SURMOF, but similar discrepancies are sometimes observed between pristine samples from different batches due to differences in their acetate concentration from incomplete reaction processes during synthesis.[28–30]

Determination of the dissolution rates

The SURMOFs here studied are expected to act as positive tone photoresists, that is, the exposed areas should be cleared out when immersed in a solvent or solution after exposure, a step known as development. The rationale behind it is that, as the crystalline structure loses some of the organic linkers during exposure, a solvent or a solution with chelating agents would more easily interact with the copper atoms and thus dissolve the remaining material at a faster rate on exposed areas. We chose aqueous solutions of ethylenediaminetetraacetic acid (EDTA), a strong chelating agent for numerous metal atoms including copper, to test

how the solubility rates of $Cu(C_2O_4)•nH_2O$ and HKUST-Cu(1) change after EUV exposures.[31] We expected the partial loss of linkers to facilitate the chelation of copper atoms by EDTA molecules, thus creating distinctive dissolution rates for exposed and unexposed thin films.

To generate a strong positive contrast, we set as a criterion that the unexposed SURMOFs thin films should not lose more than 50% of their thickness (d_0) during the development process. Therefore, the maximum dissolution rate (R_{max}) tolerated for a linear and homogeneous dissolution is:

$$R_{max} = \frac{-0.5 \times d_0}{t} \; [nm/min]$$

Considering a t = 1 min—typical for nanolithographic processes—this means that, for a 40 nm film of copper oxalate or a 30 nm film of HKUST-1(Cu), as the ones here prepared, development rates should not exceed $R_{max\ [Cu(C2O4).nH2O]}$ = 20 nm/min (3.2 µg/min; for A = 1 cm^2) and $R_{max\ HKUST\text{-}1(Cu)}$ = 15 nm/min (1.5 µg/min; for A = 1 cm^2).

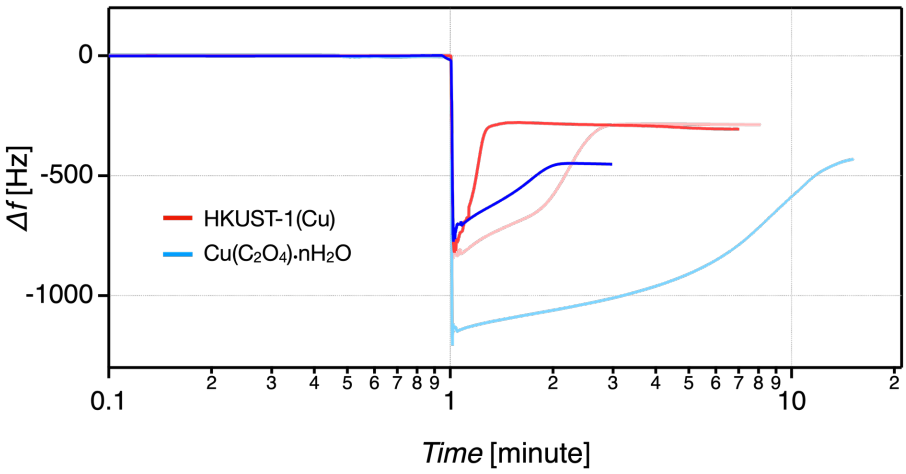

Figure 2.6: Semi-logarithmic graphs displaying the frequency of the quartz crystal upon dissolution of $Cu(C_2O_4)•nH_2O$ (in blue) and HKUST-1(Cu) (in red) SURMOFs in EDTA/NaOH aqueous solutions of 1 / 2 mM (dark lines) and 0.1 / 0.2 mM (clear lines) at 21 °C.

Dissolution rates were obtained using a quartz crystal microbalance (QCM), an analytic tool sensitive to mass changes on the surface of sensors called quartz crystals (QCs). Mass changes on the surface of the QC induce changes in the quartz resonance frequency. QCM enable the detection of mass change with nanogram sensitivity.[32] For all samples, the measured frequency drops sharply (at t = 1 min) due to the change of medium from air to the

developer solution. Then, the frequency value rises up as the SURMOF films are being dissolved. Finally, it plateaus out once the entirety of the material has been removed from the QC's surface. Considering that SURMOFs are not soft viscoelastic materials,[33] the dissolution rates are expressed by the following equation, derived from Sauerbrey's equation[34]:

$$R = \frac{\Delta f}{-C_f \times t}$$

Where Δf = the observed frequency change [Hz], C_f = the sensitivity factor of the crystal [$Hz.ng^{-1}.cm^2$], t = dissolution time [min] and R = the dissolution rate [ng cm^{-2} min^{-1}].

We obtained rates of 0.5 µg cm^{-2} min^{-1} and 4 µg cm^{-2} min^{-1} for $Cu(C_2O_4)•nH_2O$ and 4.7 µg cm^{-2} min^{-1} and 50 µg cm^{-2} min^{-1} for HKUST-1(Cu) in diluted (0.1 mM) and concentrated (1 mM) developer solutions, respectively. Because the dissolution rates obtained for pristine HKUST-1(Cu) exceed our aforementioned limit of 1.5 µg/min, the development step of the EUV exposed samples was shortened to 20 seconds for this material. The QCM frequency curves are shown in Figure 2.6.

Development

To test the dose thresholds for solubility contrast, multidose samples (see experimental section for details) were developed by immersion in a 0.1 mM EDTA developer solution during 1 min for $Cu(C_2O_4)•nH_2O$ and 20 seconds for HKUST-1(Cu).

The contrast curve of a photoresist is a graphical representation of its sensitivity when using a certain developer and development time. It is obtained by measuring the thickness remaining after exposing the material to increasing EUV doses and applying the chosen development conditions. In positive tone photoresist, the minimum EUV dose needed to clear out all of the exposed resist's thickness is called dose to clear and can be determined from the contrast curve.

For our thin films of $Cu(C_2O_4)•nH_2O$, we found a dose to clear between 250 mJ/cm^2 and 500 mJ/cm^2, far from the industry target, which lays at *ca.* 20 mJ/cm^2 (Fig. 2.7d). However, some changes are detected in the thin film already from 10 mJ/cm^2 onward using an optical microscope (Fig. 2.7b). We attribute the optical contrast to disparities in surface roughness and density of the films between exposed and pristine areas, even when no significant thickness loss was registered.

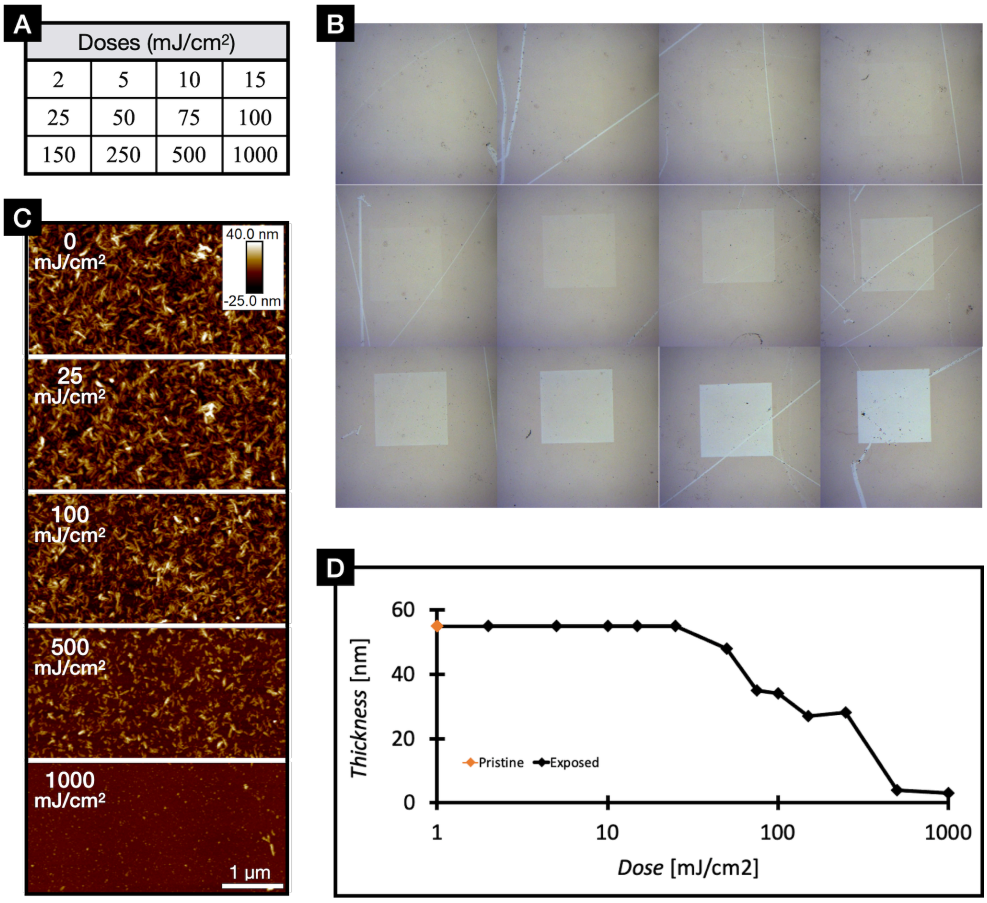

Figure 2.7: (A) EUV dose matrix of the pads printed on $Cu(C_2O_4)•nH_2O$. **(B)** Optical microscope images of each pad. **(C)** AFM micrographs illustrating the evolution of the thin films' topography (post-exposure and development) at the centre of a selected number of pads. **(D)** Semi-logarithmic graph of the thickness of the remaining SURMOF layer post-development as a function of the EUV dose (contrast-curve).

For SURMOFs like $Cu(C_2O_4)•nH_2O$, the diversity of size, shape and orientation of the crystallites is responsible for the significant absolute deviation of the film thickness, and thus the high surface roughness of the film. AFM analysis shows a decrease of the roughness for increasing doses (Fig. 2.7c). This is because exposed crystallites dissolve faster than their pristine counterparts, leading to smaller crystallites, hence a smaller absolute deviation of the thickness on exposed areas after development. And, as the reflectivity and/or refractivity of the films depend on their roughness, clear differences in color and opacity are observed on optical images between exposed and pristine areas, despite the films being too thin for the detection of transparency differences. This indirect optical contrast evidences changes in the

solubility rate already occurring at 10 mJ/cm^2 and highlights the potential of the material. We expect an optimized development procedure to drastically improve the dose-to-clear towards more competitive values.

For HKUST-1(Cu), no contrast was observed following the development step. The absence of solubility switch further supports our previous observations from XPS, IRRAS and SEM analysis post-exposure.

2.4 Discussion

In EUV photoresists, the radicals and charged species generated upon irradiation are responsible for the chemical changes, and consequently solubility rate changes, due to polymerization, acid generation and proton-catalyzed reactions, change in polarizability, or other reactions.[35,36]

For our materials, XPS and IRRAS analysis confirmed the occurrence of decarboxylation upon EUV exposure with desorption of CO_2 and/or CO fragments. The differences observed between their sensitivity is justified by differences in the nature of their crystalline structures and the reactivity of their linkers, particularly regarding the fragmentation mechanisms.

For the oxalate linkers of $Cu(C_2O_4)•nH_2O$, one ionisation reaction yields a very unstable moiety that fragmentates into a CO_2 molecule and a $CO_2^{\bullet-}$ radical anion. The latter can then transfer an electron to a Cu^{2+} species and outgas as a neutral molecule, thus completely disconnecting two copper dimers in the structure and interrupting the linear periodical structure (Fig. 2.8b and 2.1).[37] Similarly, the capture of an electron would induce the dissociation of the oxalate linker into CO_2 and $CO_2^{\bullet-}$ radical anions while the electron flow during the decarboxylation mechanism would transfer electrons to two Cu^{2+} in the process (Fig. 2.8b).

On the other hand, the more complex crystalline structure of HKUST-1(Cu), comprising tritopic aromatic linkers, requires much higher EUV doses to reach similar levels of degradation. After one or two decarboxylation reactions, the BTC's backbone can prevail and partly hold the porous network as a ditopic or monotopic linker. Because of this, a partially cleaved BTC linker only creates a small defect in the crystalline structure of the material, resulting in only minor changes in solubility and other properties of the exposed areas. Moreover, the radicals present on fragmented BTCs can be stabilised by means of conjugation until potential reaction with either water adsorbed in the pores (hydrogen subtraction) or $OH^{\bullet-}$ radical anions formed by the fragmentation of free carboxylic acid groups located at structural defects in the SURMOF. This likely means that additional fragmentation of the linker cannot occur without another ionisation event.

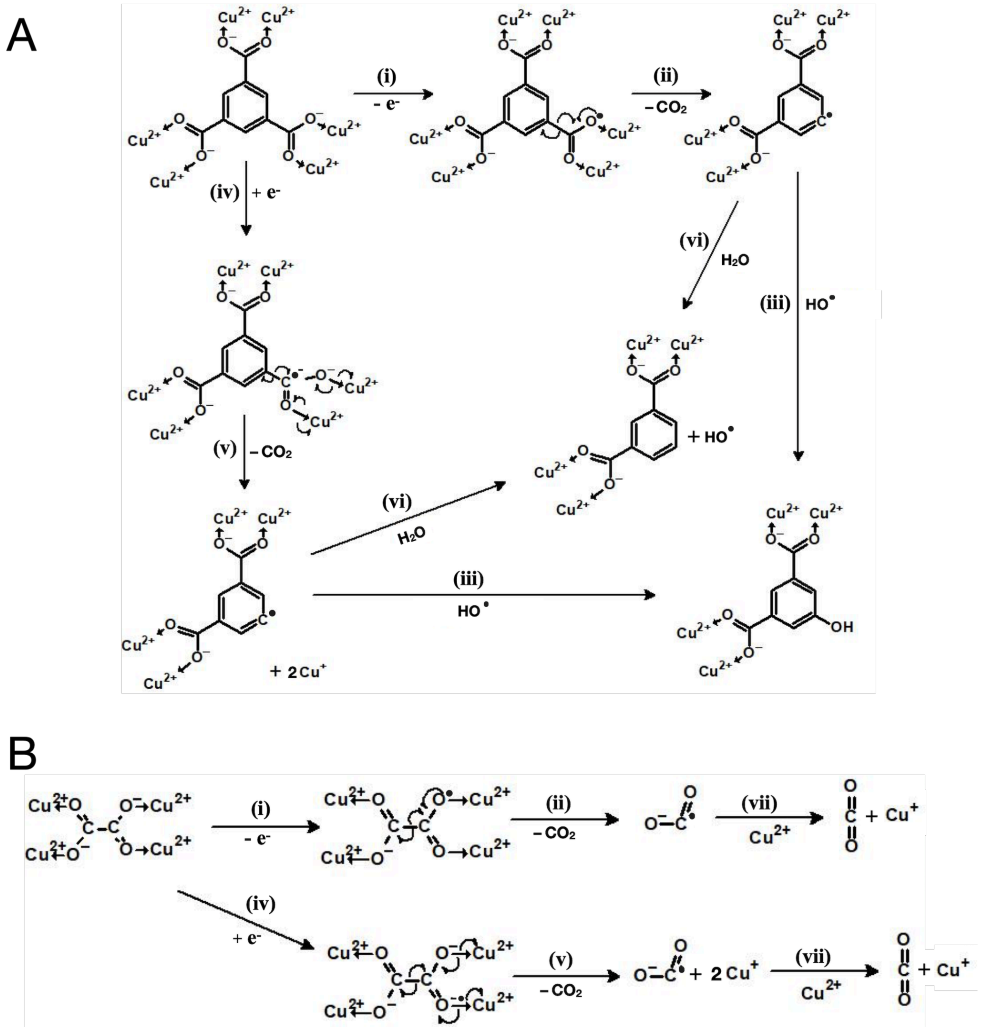

Figure 2.8: Potential fragmentation mechanisms of **(A)** the terephthalate linker in HKUST-1(Cu) and **(B)** the oxalate linker in $Cu(C_2O_4)•nH_2O$ upon direct ionization by EUV photons or ionization by electron scattering (electron attachment or electron ionization). The reaction steps are (i) ionization; (ii) decarboxylation after ionization; (iii) potential combination reaction with a radical $^{\bullet}OH$, product of the fragmentation of a free COOH group (free acid); (iv) electron attachment; (v) decarboxylation after electron attachment; (vi) potential combination reaction with H_2O present in the material; (vii) reduction of Cu^{2+} by radical $CO_2^{\bullet-}$.

And, because fragmented BTCs remain coordinated to copper dimers, their position is fixed within the structure which hinders reaction with other species in the crystal structure. This might increase the recombination probability of cleaved bonds and disfavor fragmentation and desorption (Fig. 2.8a). In addition, we speculate that the low density of HKUST-1(Cu) reduces the probability of electron scattering within the SURMOF.[38]

The reduction of Cu^{2+} ions to Cu^{+} ions by direct electron attachment with secondary electrons from the electron cascade is also expected in both materials. In that case, as well as in the case of a reduction by $CO_2^{\bullet-}$ radical anions from the dissociation of oxalate linkers, a rearrangement of the coordination of the linkers is expected. The shift of the -COO asymmetric stretching vibration observed with IRRAS on $Cu(C_2O_4)\bullet nH_2O$ could stem from such rearrangement as the remaining oxalate linkers switch from bridging to chelating upon structural reorganisation. A similar phenomenon was reported in previous studies on carboxylate coordination complexes.[39] The formation of new Cu complexes or the creation of oxygen vacancies from the loss of apical H_2O, could also affect the oxidation state of the copper atoms within the exposed material. These observations are also in accordance with previous reports on the low energy electron reactivity of $Cu(C_2O_4)\bullet nH_2O$.[37,40] as well as on the EUV and electron (80 eV) reactivity of M-oxalate MOCs (M = Co, Fe or Cr).[41,42]

To fairly compare the EUV reactivities of the two SURMOFs here studied, their respective EUV absorptivity and quantum yields should both be compared. We estimated a linear EUV absorptivity of 10.7 μm^{-1} for $Cu(C_2O_4)\bullet nH_2O$ and 5.4 μm^{-1} for HKUST-1(Cu). As a reference, metal-containing materials that already work for EUVL show linear absorptivity values around 20 μm^{-1}. For example, 20 μm^{-1} for the commercial INPRIA© photoresist,[7] around 15 μm^{-1} for specimens of the $[(C_4H_9Sn)_{12}O_{14}(OH)_6]X_2$ (X = interchangeable counterion) family of tin-based resists.[36,43] However, other less absorbing materials such as zirconium-based $Zr_6O_4(OH)_4Mc_{12}$ (Mc = methacrylate), with 6 μm^{-1}, have also proven to work at low doses, most likely due to highly efficient polymerization mechanism.[44] Traditional organic chemically amplified resists usually have linear absorptivity of around 5 μm^{-1}.[45]

Considering thin films of equal thickness (50 nm), transmittance values of 59% and 76% are calculated, for $Cu(C_2O_4)\bullet nH_2O$ and HKUST-1(Cu), respectively. Although substantially different, the sole comparison of their respective absorptivity is not sufficient to rationalize the different degree of chemical transformation observed for the two materials. Indeed, absorptivity characterizes the probability of photon absorption, only the first step of an intricate series of processes leading to solubility switch. Therefore, the decarboxylation quantum yields are a more pertinent reference to compare the materials' reactivity. They are obtained by calculating the number of carboxylates lost during exposure as a function of the number of absorbed photons. Based on our XPS results, considering an intermediate dose at

which chemical changes are observed for both SURMOF (*i.e.*, 275 mJ/cm^2), we obtain a yield of **2.4** carboxylates lost per absorbed photon for $Cu(C_2O_4)•nH_2O$ against **0.05** for HKUST-1(Cu).

The calculated absorptivity $Cu(C_2O_4)•nH_2O$ / HKUST-1(Cu) ratio of 2.0 is significantly smaller than the estimated quantum yield ratio of **48**. This implies that the poor performances of HKUST-1(Cu) for EUV exposures are not just caused by a lack of photon absorption but rather by the relative inefficiency of its ionization-induced and electron-induced reactions following photon absorption.

As the exposure progresses the chemical compositions and properties of the SURMOFs are modified. This leads to changes in their reactivity at the exposed areas; hence the variations in their quantum yields with increasing EUV doses shown in Table 2.2.

Table 2.2. *Comparison of the EUV quantum yields of HKUST-1(Cu) and $Cu(C_2O_4)•nH_2O$ as a function of the dose.*

Dose [mJ/cm^2]	25	75	150	**275**	500
Quantum yield HKUST	0	0	0	**0.05**	0.11
Quantum yield $Cu(C_2O_4)•nH_2O$	5.1	3.6	3.2	**2.4**	1.7
Ratio	/	/	/	**48**	15

In light of these results, studying the reactivity of HKUST-1 variants by derivatising the BTC linkers, the metal in the nodes and/or the content of its pores could bring valuable insights for the understanding of the radiative processes that occur during EUV irradiation. For instance, one could obtain information on the influence of the metal atom by comparing performances after full, or partial, replacement the Cu ions by other metallic elements (*e.g.*, Zn, Ni, Co). Derivatising BTC linkers to modify fragmentation mechanisms to investigate the reactivity of relevant functional groups could help optimise the organic components of EUV resists for better sensitivity and provide information concerning the electron cascade. Finally, given the low reactivity of HKUST-(Cu) itself towards EUV, loading its nano-channels and nano-pores with well-selected guests would offer unique a opportunities, as the MOF could act as an extended matrix of periodically ordered nanometer-scale reactors over a wide area.[46–50]

2.5 Conclusion

The two copper-based materials studied herein, namely $Cu(C_2O_4)•nH_2O$ and HKUST-1(Cu), show significant differences in their reactivity towards EUV irradiation, as evidenced by X-

Ray photoelectron spectroscopy (XPS), infrared reflection absorption spectroscopy (IRRAS) and post-exposure development tests.

We observed similar reaction pathways with decarboxylation and reduction of Cu^{2+} occurring upon EUV exposure for both materials. However, HKUST-1(Cu) was evidenced to be significantly less reactive with a quantum yield of decarboxylation 48 times smaller than the one of copper oxalate.

We hypothesised these discrepancies to stem from differences in their respective crystalline structures and linkers' nature. In particular, their different backbones, saturated ditopic or aromatic tritopic, lead to different reaction mechanisms after ionization- and electron-induced degradation. The cleavage of oxalates, yielding full dissociation of the linker and outgassing of CO_2, is much more efficient than fragmentation patterns in trimesate linkers. The higher connectivity of the latter further stabilizes HKUST-1(Cu) by increasing the minimum number of bonds to cleave in order to achieve complete linker desorption.

We proved that $Cu(C_2O_4)•nH_2O$ can act as a positive tone EUV resists by using basic aqueous solutions of EDTA as developer. Positive tone hybrid resists are rare since, so far, mainly molecular resists have been explored and, for those, the mechanism behind pattern formation is based on condensation reactions after their organic shells are cleaved and desorbed. However, the characteristic crystalline network provided by MOFs opens the door to new pathways for solubility switch approaches.

For copper oxalate, changes in the thin film were observed at doses as low as 10 mJ/cm^2, although with the chosen development procedure the dose to clear was found between 250 mJ/cm^2 and 500 mJ/cm^2. We are confident that an optimisation of the development conditions will considerably improve the lithographic sensitivity of this material. Contrarily, no solubility switch was detected upon irradiation of HKUST-1(Cu) with EUV light. This result is in line with the higher stability of this materials towards EUV photons observed spectroscopically.

Bibliography

(1) Moore, G. Cramming More Components onto Integrated Circuits. *Electronics* **1965**, *38* (8).

(2) Schaller, R. R. Moore's Law: Past, Present and Future. *IEEE Spectr.* **1997**, *34* (6), 52–59. https://doi.org/10.1109/6.591665.

(3) Bilski, B.; Zimmermann, J.; Roesch, M.; Liddle, J.; van Setten, E.; Bottiglieri, G.; van Schoot, J. High-NA EUV Imaging: Challenges and Outlook. *Proc. SPIE*, **2019**; p 42. https://doi.org/10.1117/12.2536329.

(4) Zahlten, C.; Gräupner, P.; van Schoot, J.; Kuerz, P.; Stoeldraijer, J.; Kaiser, W. High-NA EUV Lithography: Pushing the Limits. *Proc. SPIE (EMLC)*; **2019**; p 43. https://doi.org/10.1117/12.2536469.

(5) Levinson, H. J.; Brunner, T. A. Current Challenges and Opportunities for EUV Lithography. *Proc. SPIE*; **2018**; p 2. https://doi.org/10.1117/12.2502791.

(6) Wood, O. R. EUVL: Challenges to Manufacturing Insertion. *J. Photopolym. Sci. Technol.* **2017**, *30* (5), 599–604. https://doi.org/10.2494/photopolymer.30.599.

(7) Grenville, A.; Anderson, J. T.; Clark, B. L.; De Schepper, P.; Edson, J.; Greer, M.; Jiang, K.; Kocsis, M.; Meyers, S. T.; Stowers, J. K.; Telecky, A. J.; De Simone, D.; Vandenberghe, G. Integrated Fab Process for Metal Oxide EUV Photoresist. *Adv. Patterning Mater. Process. XXXII* **2015**, *9425* (April), 94250S. https://doi.org/10.1117/12.2086006.

(8) Businesswire. EUV Photoresist Pioneer Inpria Raises $23.5 Million in Series B Funding Led by Samsung Ventures. July 2017.

(9) Businesswire. EUV Photoresist Pioneer Inpria Raises $31 Million in Series C Funding Led by JSR Corporation. February 2020.

(10) Henke, B. L.; Gullikson, E. M.; Davis, J. C. X-Ray Interactions: Photoabsorption, Scattering, Transmission, and Reflection at E = 50-30,000 eV, Z = 1-92. *At. Data Nucl. Data Tables* **1993**, *54* (2), 181–342. https://doi.org/10.1006/adnd.1993.1013.

(11) Manouras, T.; Argitis, P. High Sensitivity Resists for EUV Lithography: A Review of Material Design Strategies and Performance Results. *Nanomaterials* **2020**, *10* (8), 1–24. https://doi.org/10.3390/nano10081593.

(12) Narasimhan, A.; Wisehart, L.; Grzeskowiak, S.; Ocola, L. E.; Denbeaux, G.; Brainard, R. L. What We Don't Know About EUV Exposure Mechanisms. *J. Photopolym. Sci. Technol.* **2017**, *30* (1), 113–120. https://doi.org/10.2494/photopolymer.30.113.

(13) Lio, A. EUV Photoresists: A Progress Report and Future Prospects. *Synchrotron Radiat. News* **2019**, *32* (4), 9–14. https://doi.org/10.1080/08940886.2019.1634431.

(14) Luo, C.; Xu, C.; Lv, L.; Li, H.; Huang, X.; Liu, W. Review of Recent Advances in Inorganic Photoresists. *RSC Adv.* **2020**, *10* (14), 8385–8395.

https://doi.org/10.1039/c9ra08977b.

(15) Frameworks for Commercial Success. *Nat. Chem.* **2016**, *8* (11), 987–987. https://doi.org/10.1038/nchem.2661.

(16) Ameloot, R.; Stassen, I.; Burtch, N.; Talin, A.; Falcaro, P.; Allendorf, M. An Updated Roadmap for the Integration of Metal-Organic Frameworks with Electronic Devices and Chemical Sensors. *Chem. Soc. Rev.* **2017**, *46* (11), 3185–3241. https://doi.org/10.1039/c7cs00122c.

(17) Kirchon, A.; Feng, L.; Drake, H. F.; Joseph, E. A.; Zhou, H.-C. From Fundamentals to Applications: A Toolbox for Robust and Multifunctional MOF Materials. *Chem. Soc. Rev.* **2018**, *47* (23), 8611–8638. https://doi.org/10.1039/C8CS00688A.

(18) Schrader, I.; Wittig, L.; Richter, K.; Vieker, H.; Beyer, A.; Gölzhäuser, A.; Hartwig, A.; Swiderek, P. Formation and Structure of Copper(II) Oxalate Layers on Carboxy-Terminated Self-Assembled Monolayers. *Langmuir* **2014**, *30* (40), 11945–11954. https://doi.org/10.1021/la5026312.

(19) Lin, K. S.; Adhikari, A. K.; Ku, C. N.; Chiang, C. L.; Kuo, H. Synthesis and Characterization of Porous HKUST-1 Metal Organic Frameworks for Hydrogen Storage. *Int. J. Hydrogen Energy* **2012**, *37* (18), 13865–13871. https://doi.org/10.1016/j.ijhydene.2012.04.105.

(20) Gronheid, R.; Solak, H. H.; Ekinci, Y.; Jouve, A.; Van Roey, F. Characterization of Extreme Ultraviolet Resists with Interference Lithography. *Microelectron. Eng.* **2006**, *83* (4–9), 1103–1106. https://doi.org/10.1016/j.mee.2006.01.149.

(21) Wang, Z.; Wöll, C. Fabrication of Metal–Organic Framework Thin Films Using Programmed Layer-by-Layer Assembly Techniques. *Adv. Mater. Technol.* **2019**, *4* (5), 1–22. https://doi.org/10.1002/admt.201800413.

(22) Chenakin, S.; Kruse, N. XPS Characterization of Transition Metal Oxalates. *Appl. Surf. Sci.* **2020**, *515* (February), 146041. https://doi.org/10.1016/j.apsusc.2020.146041.

(23) Chenakin, S. P.; Szukiewicz, R.; Barbosa, R.; Kruse, N. Surface Analysis of Transition Metal Oxalates: Damage Aspects. *J. Electron Spectros. Relat. Phenomena* **2016**, *209*, 66–77. https://doi.org/10.1016/j.elspec.2016.04.001.

(24) Grosvenor, A. P.; Kobe, B. A.; Biesinger, M. C.; McIntyre, N. S. Investigation of Multiplet Splitting of Fe 2p XPS Spectra and Bonding in Iron Compounds. *Surf. Interface Anal.* **2004**, *36* (12), 1564–1574. https://doi.org/10.1002/sia.1984.

(25) Lugier, O.; Pokharel, U.; Castellanos, S. Impact of Synthetic Conditions on the Morphology and Crystallinity of FDMOF-1(Cu) Thin Films. *Cryst. Growth Des.* **2020**, *20* (8), 5302–5309. https://doi.org/10.1021/acs.cgd.0c00529.

(26) Burrows, A. D.; Tiana, D.; Cadman, L. K.; Walsh, A.; Mahon, M. F.; Stubbs, N. E.; Bristow, J. K. Compositional Control of Pore Geometry in Multivariate Metal–Organic Frameworks: An Experimental and Computational Study. *Dalt. Trans.* **2015**, *45* (10), 4316–4326. https://doi.org/10.1039/c5dt04045k.

(27) Nishikawa, Y.; Osawa, M.; Ataka, K.-I.; Yoshii, K. Surface-Enhanced Infrared Spectroscopy: The Origin of the Absorption Enhancement and Band Selection Rule in the Infrared Spectra of Molecules Adsorbed on Fine Metal Particles. *Appl. Spectrosc.* **1993**, *47* (9), 1497–1502.

(28) Tan, K.; Nijem, N.; Canepa, P.; Gong, Q.; Li, J.; Thonhauser, T.; Chabal, Y. J. Stability and Hydrolyzation of Metal Organic Frameworks with Paddle-Wheel SBUs upon Hydration. *Chem. Mater.* **2012**, *24* (16), 3153–3167. https://doi.org/10.1021/cm301427w.

(29) Delen, G.; Ristanović, Z.; Mandemaker, L. D. B.; Weckhuysen, B. M. Mechanistic Insights into Growth of Surface-Mounted Metal-Organic Framework Films Resolved by Infrared (Nano-) Spectroscopy. *Chem. - A Eur. J.* **2018**, *24* (1), 187–195. https://doi.org/10.1002/chem.201704190.

(30) Dhumal, N. R.; Singh, M. P.; Anderson, J. A.; Kiefer, J.; Kim, H. J. Molecular Interactions of a Cu-Based Metal–Organic Framework with a Confined Imidazolium-Based Ionic Liquid: A Combined Density Functional Theory and Experimental Vibrational Spectroscopy Study. *J. Phys. Chem. C* **2016**, *120* (6), 3295–3304. https://doi.org/10.1021/acs.jpcc.5b10123.

(31) Tsotsalas, M.; Liu, J.; Tettmann, B.; Grosjean, S.; Shahnas, A.; Wang, Z.; Azucena, C.; Addicoat, M.; Heine, T.; Lahann, J.; Overhage, J.; Bräse, S.; Gliemann, H.; Wöll, C. Fabrication of Highly Uniform Gel Coatings by the Conversion of Surface-Anchored Metal-Organic Frameworks. *J. Am. Chem. Soc.* **2014**, *136* (1), 8–11. https://doi.org/10.1021/ja409205s.

(32) O'Sullivan, C. K.; Guilbault, G. G. Commercial Quartz Crystal Microbalances - Theory and Applications. *Biosens. Bioelectron.* **1999**, *14* (8–9), 663–670. https://doi.org/10.1016/S0956-5663(99)00040-8.

(33) Kankare, J. Sauerbrey Equation of Quartz Crystal Microbalance in Liquid Medium. *Langmuir* **2002**, *18* (18), 7092–7094. https://doi.org/10.1021/la025911w.

(34) Sauerbrey, G. Verwendung von Schwingquarzen Zur Wägung Dünner Schichten Und Zur Mikrowägung. *Zeitschrift für Phys.* **1959**, *155* (2), 206–222. https://doi.org/10.1007/BF01337937.

(35) Wu, L.; Baljozovic, M.; Portale, G.; Kazazis, D.; Vockenhuber, M.; Jung, T.; Ekinci, Y.; Castellanos, S. Mechanistic Insights in Zr- and Hf-Based Molecular Hybrid EUV Photoresists. *J. Micro/Nanolithography, MEMS, MOEMS* **2019**, *18* (01), 1. https://doi.org/10.1117/1.jmm.18.1.013504.

(36) Cardineau, B.; Del Re, R.; Marnell, M.; Al-Mashat, H.; Vockenhuber, M.; Ekinci, Y.; Sarma, C.; Freedman, D. A.; Brainard, R. L. Photolithographic Properties of Tin-Oxo Clusters Using Extreme Ultraviolet Light (13.5 nm). *Microelectron. Eng.* **2014**, *127*, 44–50. https://doi.org/10.1016/j.mee.2014.04.024.

(37) Ahlenhoff, K.; Koch, S.; Emmrich, D.; Dalpke, R.; Gölzhäuser, A.; Swiderek, P. Electron-Induced Chemistry of Surface-Grown Coordination Polymers with

Different Linker Anions. *Phys. Chem. Chem. Phys.* **2019**, *21* (5), 2351–2364. https://doi.org/10.1039/c8cp07028h.

(38) Ahlenhoff, K.; Preischl, C.; Swiderek, P.; Marbach, H. Electron Beam-Induced Surface Activation of Metal–Organic Framework HKUST-1: Unraveling the Underlying Chemistry. *J. Phys. Chem. C* **2018**, *122* (46), 26658–26670. https://doi.org/10.1021/acs.jpcc.8b06226.

(39) Nara, M.; Torii, H.; Tasumi, M. Correlation between the Vibrational Frequencies of the Carboxylate Group and the Types of Its Coordination to a Metal Ion: An Ab Initio Molecular Orbital Study. *J. Phys. Chem.* **1996**, *100* (51), 19812–19817. https://doi.org/10.1021/jp9615924.

(40) Rückriem, K.; Grotheer, S.; Vieker, H.; Penner, P.; Beyer, A.; Gölzhäuser, A.; Swiderek, P. Efficient Electron-Induced Removal of Oxalate Ions and Formation of Copper Nanoparticles from Copper(II) Oxalate Precursor Layers. *Beilstein J. Nanotechnol.* **2016**, *7* (1), 852–861. https://doi.org/10.3762/bjnano.7.77.

(41) Grzeskowiak, S.; Narasimhan, A.; Murphy, M.; Napolitano, L.; Freedman, D. A.; Brainard, R. L.; Denbeaux, G. Reactivity of Metal-Oxalate EUV Resists as a Function of the Central Metal. *Adv. Patterning Mater. Process. XXXIV* **2017**, *10146*, 1014605. https://doi.org/10.1117/12.2258151.

(42) Kopyra, J.; Rabilloud, F.; Abdoul-Carime, H. Interaction of Gas Phase Copper(II) Acetylacetonate with Slow Electrons. *Phys. Chem. Chem. Phys.* **2018**, *20* (11), 7746–7753. https://doi.org/10.1039/c7cp08149a.

(43) Haitjema, J.; Zhang, Y.; Vockenhuber, M.; Kazazis, D.; Ekinci, Y.; Brouwer, A. M. Extreme Ultraviolet Patterning of Tin-Oxo Cages. *J. Micro/Nanolithography, MEMS, MOEMS* **2017**, *16* (03), 1. https://doi.org/10.1117/1.jmm.16.3.033510.

(44) Wu, L.; Bespalov, I.; Witte, K.; Lugier, O.; Haitjema, J.; Vockenhuber, M.; Ekinci, Y.; Watts, B.; Brouwer, A. M.; Castellanos, S. Unravelling the Effect of Fluorinated Ligands in Hybrid EUV Photoresists by X-Ray Spectroscopy. *J. Mater. Chem. C* **2020**, *8* (42), 14757–14765. https://doi.org/10.1039/d0tc03216f.

(45) Fallica, R.; Haitjema, J.; Wu, L.; Castellanos, S.; Brouwer, F.; Ekinci, Y. Absorption Coefficient and Exposure Kinetics of Photoresists at EUV. *Extrem. Ultrav. Lithogr. VIII* **2017**, *10143* (March 2017), 101430A. https://doi.org/10.1117/12.2257240.

(46) Hu, T.; Jiang, Y.; Ding, Y. Computational Screening of Metal-Substituted HKUST-1 Catalysts for Chemical Fixation of Carbon Dioxide into Epoxides. *J. Mater. Chem. A* **2019**, *7* (24), 14825–14834. https://doi.org/10.1039/C9TA02455G.

(47) Bhardwaj, S. K.; Bhardwaj, N.; Kaur, R.; Mehta, J.; Sharma, A. L.; Kim, K. H.; Deep, A. An Overview of Different Strategies to Introduce Conductivity in Metal-Organic Frameworks and Miscellaneous Applications Thereof. *J. Mater. Chem. A* **2018**, *6* (31), 14992–15009. https://doi.org/10.1039/c8ta04220a.

(48) Chui, S. S. Y.; Lo, S. M. F.; Charmant, J. P. H.; Orpen, A. G.; Williams, I. D. A Chemically Functionalizable Nanoporous Material [Cu3(TMA)2 (H2O)3](N).

Science. **1999**, *283* (5405), 1148–1150. https://doi.org/10.1126/science.283.5405.1148.

(49) Talin, A. A.; Centrone, A.; Ford, A. C.; Foster, M. E.; Stavila, V.; Haney, P.; Kinney, R. A.; Szalai, V.; El Gabaly, F.; Yoon, H. P.; Léonard, F.; Allendorf, M. D. Tunable Electrical Conductivity in Metal-Organic Framework Thin-Film Devices. *Science.* **2014**, *343* (6166), 66–69. https://doi.org/10.1126/science.1246738.

(50) Sava Gallis, D. F.; Parkes, M. V.; Greathouse, J. A.; Zhang, X.; Nenoff, T. M. Enhanced O_2 Selectivity versus N_2 by Partial Metal Substitution in Cu-BTC. *Chem. Mater.* **2015**, *27* (6), 2018–2025. https://doi.org/10.1021/cm5042293.

Chapter 3

Extreme Ultraviolet Photoelectron Spectroscopy on Fluorinated Monolayers: towards Nanolithography on Monolayers*

Abstract

The semiconductor industry plans to keep fabricating integrated circuits, progressively decreasing their features size, by employing extreme ultraviolet lithography (EUVL). With this method, new designs and concepts for photoresist materials need to be conceived. In this work, we explore an alternative concept to the classic photoresist material by using an organic self-assembled monolayer (SAM) on a gold substrate. The monolayer, composed of a richly fluorinated thiol sensitive to low-energy electrons, is adsorbed on the Au substrate which acts as main EUV-absorber and as the source of photoelectrons and secondary electrons. We investigate the stability of the SAM adsorbed on gold towards EUV radiation by means of *in-situ* photoelectron spectroscopy. The photoelectron spectra indicate that the monolayer attenuates a significant amount of primary electrons generated in the gold layer. The spectral evolution upon EUV irradiation indicates that the SAM loses a significant amount of its initial fluorine content (*ca.* 40% at 200 mJ/cm^2). We attribute these chemical changes mostly to the interaction with the electrons generated in the thiol/Au system.

*Lugier, O.; Troglia, A.; Sadegh, N.; van Kessel, L.; Bliem, R.; Mahne, N.; Nannarone, S.; Castellanos, S. Extreme Ultraviolet Photoelectron Spectroscopy on Fluorinated Monolayers: Towards Nanolithography on Monolayers. *J. Photopolym. Sci. Technol.* **2020**, *33* (2), 229–234.
https://doi.org/10.2494/photopolymer.33.229

3.1 Introduction

Future integrated circuits are expected to reach the 10 nm feature size (node) and below in the coming decade. The way chosen by the semiconductor industry to fabricate them in a cost-effective manner is by employing extreme ultraviolet (EUV) lithography. However, the use of such highly energetic EUV photons leads to complex chemical processes, involving the interaction between the photoresist materials and electrons generated upon irradiation.[1,2] In addition, the optical projection will be further improved by using an optical system with higher numerical aperture (NA) in future EUV scanners. Yet, a consequence of using higher NA is having a lower depth of focus (DoF),[3] which requires even thinner films of photoresist material. Therefore, to make an efficient use of this refined technology, new resist concepts should be explored, so that all the targets in the nanopattern resolution and quality can be met.

In this work, we explore an alternative concept to the existing resists. We study a system where a monolayer of organic molecules is adsorbed on the surface of a substrate consisting of a metal with a relatively high EUV photon absorption cross-section. In this way, absorption events occur mainly in the substrate but the chemistry occurs mainly on the organic molecules at the surface. This is because the electrons generated in the substrate upon photon absorption can damage the molecules on top. Turchanin et al. proved that indeed EUV lithography can be performed on self-assembled monolayers (SAMs) adsorbed on gold, though very high doses seemed to be required.[4]

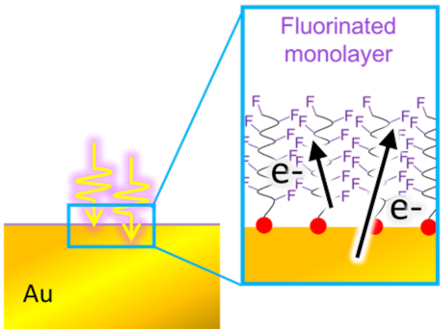

Figure 3.1: Schematic of a monolayer of fluorinated carbon chains adsorbed on an Au substrate when it is irradiated with EUV photons. Photoelectrons generated upon the absorption of EUV photons (absorption mainly in the Au substrate) induce chemical change.

Yet, the reactivity of organic molecules towards electrons is very much dependent on the molecular structure.[5] Here, we studied a SAM based on a fluorinated carbon chain (Fig. 3.1). It has been reported in the literature that C-F bonds are prone to cleave with electrons[6,7] and, in particular, fluorinated thiols undergo many chemical reactions when exposed to low-energy electrons.[8] It is foreseen that chemical damage induced in a fluorinated monolayer could provide high chemical contrast between exposed and unexposed areas through the decrease of hydrophobicity resulting from the loss of fluorine. Such contrast could be used for lithographic applications.[8,9]

3.2 Experimental

3.2.1 Sample preparation

Polycrystalline gold surfaces were prepared by sputter coating (Leica EM ACE600) silicon substrates with a layer of 50 nm of gold (adhesion layer: 5 nm of Chromium). The fluorinated thiol 1H,1H,2H,2H-Perfluoro-1-decanethiol (HFDT) was purchased from Sigma-Aldrich. The thiol was adsorbed on the Au surfaces by immersing the substrates in an ethanol solution of HFDT (3 mM, 24 h, RT).

3.2.2 Exposure and characterisation (synchrotron beamline)

Chemical changes induced by EUV photons were evaluated by means of photoelectron spectroscopy (PES) provided with an hemispherical analyzer with energy resolution ~ 100 meV at synchrotron IOM-CNR BEAR beamline station at ELETTRA in Trieste, Italy.[10–12] Monochromatized (approx. 30 meV of resolution) photons of 92 eV were used as excitation energy. The incoming light was linearly polarized (horizontally) orthogonal to the incidence plane (*s*-polarization ~ 97% of polarization degree) with light spot at sample ~ 400 × 140 μm^2 (horizontal × vertical). The angle of incidence was 45° with the electron analyzer positioned in normal emission. The impinging photons intensity at 92 eV was measured by an absolute (AXUV100) photodiode. Exposure doses were estimated according to beamline optics settings, light spot and impinging flux. To correct for possible beam fluctuation, the acquired data was accompanied with its relative photon flux, monitored on the last optical element (refocusing mirror) upstream of the sample.

To prevent exposure damage of the monolayer during the acquisition, the evolution of the photoelectron emission intensities was recorded starting on a fresh spot for each kinetic energy. This was achieved by using in-sequence acquisition, effectively correlating sample stage movement (xy) with kinetic energy tuning of the analyser. In this way, stacks of data of photoelectron intensity versus dose at fixed kinetic energy were obtained. Finally, spectra

were reconstructed from these stacks of data by extracting the values of intensity at identical dose for each kinetic energy.
Theoretical calculations on the HFDT molecule were performed with Gaussian 16[13] using Density Functional Theory (DFT), and employing the B3LYP functional and 6-311G basis set.

3.3 Results and discussion

Photoelectron spectroscopy (PES), owing to its surface sensitivity was chosen to identify and quantify chemical changes induced by EUV photons on a self-assembled monolayer of fluorinated thiol adsorbed on polycrystalline gold, HFDT/Au. By using 92 eV as excitation energy, both the damage and the monitoring of the damage were conducted simultaneously, effectively reducing the possibility of undesired degradation commonly occurring when sample irradiation and PES measurement take place individually. The photoemission spectra recorded from the Au substrate and from HFDT/Au pristine sample (exposure of *ca.* 1 mJ/cm^2) are shown in Figure 3.2. The zero of binding energy scale was set at the onset (Fermi level) of the bare Au valence spectrum.

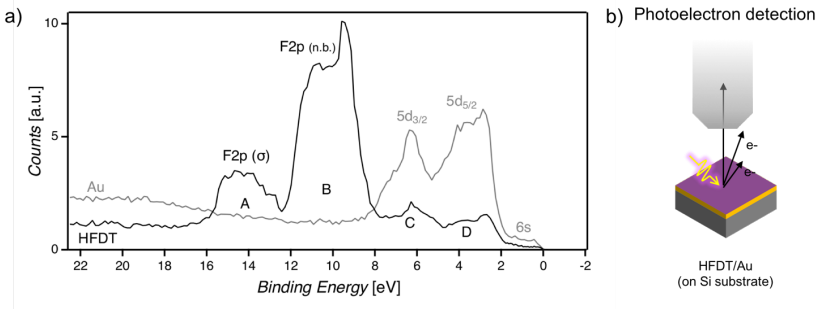

Figure 3.2: a) Experimental photoelectron spectra recorded with 92 eV photon energy of the Au-coated substrate (grey) and pristine HFDT/Au sample **b)** Basic scheme of the PES experiment.

In the spectrum of Au, two main broad non-symmetric peaks are observed from photoelectrons emitted by the 5 d orbitals ($5d_{5/2}$, 3 – 5 eV and $5d_{3/2}$, 5 – 8.5 eV).[14–17] A broad feature arises from 14 eV on, that can either be attributed to the presence of nanometric aggregates on Au surface or to the detection of electrons generated during the photoelectron scattering through the Au. The spectrum of HFDT on Au clearly differs from the Au one. Two prominent peak envelopes in the 12.7 – 16.0 eV (A) and 8.0 – 12.7 eV (B) binding energy range are clearly distinguishable in the monolayer's spectrum. These exact features had been previously observed in photoelectron studies performed on analogous molecules with silane as anchoring group for silicon substrates.[9] In addition, the peaks arising from the

Au 5d photoelectrons (C and D) are also visible, although with much lower intensity, reasonably ascribable to scattering attenuation through the film, as discussed below. It is expected that photoelectrons coming from the upmost levels of the valence band of the HFDT/Au system also contribute to the spectral lineshape in this region (see fittings below). No evident energy shifts are detected in the Au 5d peaks.

To assign the peaks in the PE spectrum of HFDT, the molecular orbitals (MO) of the molecule in the gas phase were calculated with density functional theory (B3LYP functional, 6-311G basis set). The representation of some selected MOs in the 25 eV to 0 eV binding energy range is shown in Figure 3.3. The actual energy of the MOs can vary when the molecule is embedded in a monolayer adsorbed on Au, due to intermolecular interactions and to the bonding of the sulphur atom to the Au atoms at the substrate surface. Yet, despite the energy shift in the theoretical calculations, it is reasonable to assign the broad peaks A and B to photoelectrons generated from the F 2p orbitals that are participating in different molecular orbitals, in line with previous assignments in the literature.[9] It is tempting to further distinguish between types of F 2p orbitals for these two regions. Photoelectrons contributing to peak B could be assigned to F 2p orbitals with a "non-bonding" character, as the calculated MOs in the range from 10 to 15 eV (represented by red lines in the energy diagram in Fig. 3.3) seem to be located on the F 2p orbital with a perpendicular orientation regarding the C-F bond.

DFT calculations also show that for MOs with lower energies (delimited by the purple lines in the energy diagram) the F 2p orbitals participate in what looks like σ bonds along the C-F bond. We presume that binding orbitals of this kind are the origin of the broad peak A at a higher binding energy range.

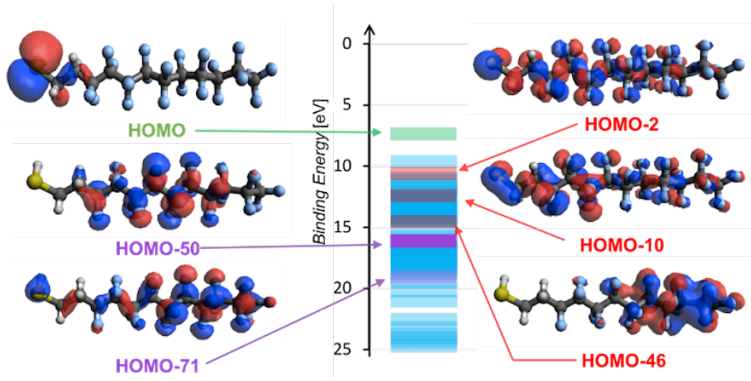

Figure 3.3: Energy diagram of the HFDT molecular orbitals (MO) calculated with DFT in the gas phase (B3LYP, basis set 6-311G). Some selected MOs are represented.

Although F s and p electrons have relatively high photon absorption cross-sections at 92 eV (~0.8 Mbarn/atom), and despite the high concentration of F atoms in the HFDT self-assembled monolayer (17 fluorine atoms per molecule), a high transmittance is estimated for this monolayer (~1.2 - 1.5 nm thickness, depending on the molecular packing). Using the atomic photon absorption cross-section as reported in the literature,[18] the molar cross-section for the HFDT molecule is calculated to be 3.7×10^7 cm^2/mol. Assuming that there are approximately 3 - 4 molecules per square nm[19,20] ($5.0 - 6.6 \times 10^{-10}$ mol/cm^2), and taking into account the angle of incidence of the impinging photons, the estimated transmittance for such a layer would be in the range of 97-98%. Therefore, most of the light goes through the HFDT monolayer and is absorbed by the Au substrate (50 nm thickness, ~0% transmittance). However, the number of photoelectrons generated at the Au layer that reach the detector is much lower in the presence of the HFDT monolayer. We attribute this loss of intensity (~ 65%) of the Au 5d peaks to the scattering of the primary photoelectrons through the monolayer.

The evolution of the HFDT photoelectron spectrum with exposure at 92 eV is shown in Figure 3.4. A clear bleach of the peaks assigned to the F 2p orbitals is observed, indicating that fluorine concentration in the monolayer decreases.

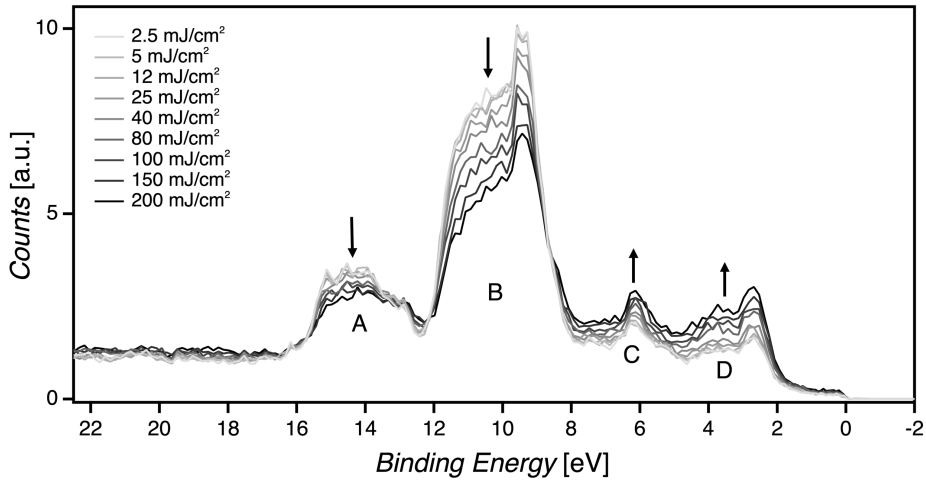

Figure 3.4: Evolution of the photoelectron spectrum of HFDT/Au with EUV exposure (some selected doses are shown).

It has been previously reported that exposure of SAMs based on thiols featuring semi-fluorinated carbon-chains to low-energy electrons (10 eV) leads to the cleavage of C-F bonds and outgassing of fluorine, as well as C-C cleavage leading to the desorption of small fluorinated carbon chains.[8] Therefore, we assume that the fluorine loss induced by EUV exposure of the HFDT/Au system likely occurs via similar processes, as most of the chemical reactions that the monolayer undergoes are expected to be induced by the low-energy photoelectrons (typically ~< 80 eV) generated at the monolayer and the underlaying Au layer.[21]

To estimate the rate of the EUV-induced changes, we calculated the relative areas (A/A_0) of peaks A, B, C and D and plotted them as a function of dose in Figure 3.5. The bleach of the peaks assigned to F 2p orbitals (A and B) reaches ~60% at 200 mJ/cm^2. Some molecular levels associated to sulphur and carbon atoms overlap with the Au valence peaks. Although the cross sections at 92 eV as well as the densities of sulphur and carbon atoms are lower than those of Au, these overlaps would explain the apparent different intensity ratio between $5d_{3/2}$ and $5d_{5/2}$ peaks in the pristine HFDT/Au sample compared to Au, as well as the slightly different increase rate of the two peaks upon EUV exposure.[11]

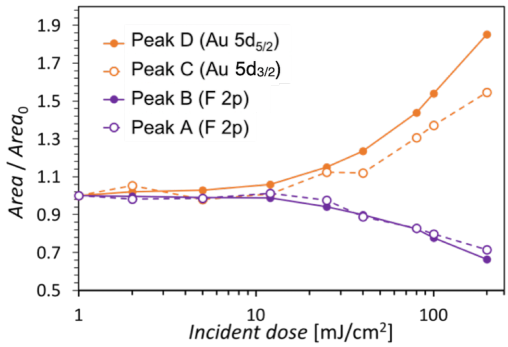

Figure 3.5: Relative area of all peaks as a function of dose.

In addition to the bleaching of peaks A and B, which we attribute to F loss, the spectra display changes at 13 eV and 17 eV (Fig. 3.4), which could be due to the creation of new electronic levels, *i.e.,* new molecular orbitals. Partial loss of F-atoms is followed by the formation of highly reactive carbon-sites that can lead to the formation of mono-fluorinated carbon atoms and unsaturated C=C bonds and to cross-linking reactions between neighbouring molecules. These examples have all been showed to take place under low-energy electron irradiation for similar systems.[8] And, as mentioned earlier, we expect similar events to happen under EUV irradiation of the HFDT/Au system as a result of the interaction between the monolayer and the low-energy electrons (KE range from ~80 eV to 0 eV), mostly generated by the Au

substrate.[22,23] These new molecular orbitals deriving from new bonds and chemical species can thus contribute to the modification of the spectral shape with increasing dose. However, the elucidation of the exact products that result from the 92 eV irradiation is out of the scope of this work.

3.4 Conclusions

Photoelectron spectroscopy at a photon energy of 92 eV on monolayers of fluorinated thiols adsorbed on polycrystalline gold surfaces (HFDT/Au) revealed that EUV exposure of such a system leads to a remarkable loss of fluorine-containing species, reaching approximately 40% of fluorine content after a dose of 200 mJ/cm^2. We attribute the chemical processes that the monolayer undergoes upon EUV irradiation to the action of photoelectrons and secondary electrons generated both within the monolayer and the underlaying Au layer. While further work is needed to fully elucidate these phenomenon, the extent of fluorine loss in the studied EUV dose range suggests that a considerable chemical contrast between exposed and unexposed areas is attained with this type of molecules, which could be used for lithography purposes.

Bibliography

(1) Ashby, P. D.; Olynick, D. L.; Ogletree, D. F.; Naulleau, P. P. Resist Materials for Extreme Ultraviolet Lithography: Toward Low-Cost Single-Digit-Nanometer Patterning. *Adv. Mater.* **2015**, *27* (38), 5813–5819. https://doi.org/http://dx.doi.org/10.1002/adma.201501171.

(2) van Dorp, W. F. Chapter 3 - Theory: Electron-Induced Chemistry. In *Frontiers of Nanoscience*; Elsevier, **2016**; Vol. 11, pp 115–133.

(3) Zahlten, C.; Gräupner, P.; van Schoot, J.; Kuerz, P.; Stoeldraijer, J.; Kaiser, W. High-NA EUV Lithography: Pushing the Limits. *Proc. SPIE*; **2019**; p 43. https://doi.org/10.1117/12.2536469.

(4) Turchanin, A.; Schnietz, M.; El-Desawy, M.; Solak, H. H.; David, C.; Gölzhäuser, A. Fabrication of Molecular Nanotemplates in Self-Assembled Monolayers by Extreme-Ultraviolet-Induced Chemical Lithography. *Small* **2007**, *3* (12), 2114–2119. https://doi.org/10.1002/smll.200700516.

(5) Böhler, E.; Warneke, J.; Swiderek, P. Control of Chemical Reactions and Synthesis by Low-Energy Electrons. *Chem. Soc. Rev.* **2013**, *42* (24), 9219–9231. https://doi.org/10.1039/c3cs60180c.

(6) Langer, J.; Stano, M.; Gohlke, S.; Foltin, V.; Matejcik, S.; Illenberger, E. Reactions in Trifluoroacetic Acid (CF_3COOH) Induced by Low Energy Electron Attachment. *Chem. Phys. Lett.* **2006**, *419* (1–3), 228–232. https://doi.org/10.1016/j.cplett.2005.11.073.

(7) Rosenberg, S. G.; Barclay, M.; Fairbrother, D. H. Electron Induced Surface Reactions of Organometallic Metal $(hfac)_2$ Precursors and Deposit Purification. *ACS Appl. Mater. Interfaces* **2014**, *6* (11), 8590–8601. https://doi.org/10.1021/am501457h.

(8) Frey, S.; Heister, K.; Zharnikov, M.; Grunze, M. Modification of Semifluorinated Alkanethiolate Monolayers by Low Energy Electron Irradiation. *Phys. Chem. Chem. Phys.* **2000**, *2* (9), 1979–1987. https://doi.org/10.1039/a910314g.

(9) Haruyama, Y.; Matsui, S. Electronic Structure of Fluorinated Self-Assembled Monolayer Investigated by Photoelectron Spectroscopy in the Valence Band Region. *Jpn. J. Appl. Phys.* **2015**, *54* (7), 075202. https://doi.org/10.7567/JJAP.54.075202.

(10) Pasquali, L.; Mukherjee, S.; Terzi, F.; Giglia, A.; Mahne, N.; Koshmak, K.; Esaulov, V.; Toccafondi, C.; Canepa, M.; Nannarone, S. Structural and Electronic Properties of Anisotropic Ultrathin Organic Films from Dichroic Resonant Soft X-Ray Reflectivity. *Phys. Rev. B - Condens. Matter Mater. Phys.* **2014**, *89* (4), 1–7. https://doi.org/10.1103/PhysRevB.89.045401.

(11) Pasquali, L.; Terzi, F.; Seeber, R.; Nannarone, S.; Datta, D.; Dablemont, C.; Hamoudi, H.; Canepa, M.; Esaulov, V. A. UPS, XPS, and NEXAFS Study of Self-Assembly of Standing 1,4-Benzenedimethanethiol SAMs on Gold. *Langmuir* **2011**, *27* (8), 4713–4720. https://doi.org/10.1021/la105063u.

(12) http://www.elettra.trieste.it/elettra-beamlines/bear.html.

(13) Frisch, M. J.; Trucks, G. W.; Schlegel, H. B.; Scuseria, G. E.; Robb, M. A.; Cheeseman, J. R.; Scalmani, G.; Barone, V.; Petersson, G. A.; Nakatsuji, H.; Li, X.; Caricato, M.; Marenich, A. V.; Bloino, J.; Janesko, B. G.; Gomperts, R.; Mennucci, B.; Hratch, D. J. Gaussian 16, Revision C.01. Wallingford CT, p Gaussian, Inc., Wallingford CT (2016).

(14) Piao, H.; McIntyre, N. S. High-Resolution Valence Band XPS Studies of Thin Film Au-Al Alloys. *J. Electron Spectros. Relat. Phenomena* **2001**, *119* (1), 29–33. https://doi.org/10.1016/S0368-2048(01)00234-1.

(15) Visikovskiy, A.; Matsumoto, H.; Mitsuhara, K.; Nakada, T.; Akita, T.; Kido, Y. Electronic D-Band Properties of Gold Nanoclusters Grown on Amorphous Carbon. *Phys. Rev. B - Condens. Matter Mater. Phys.* **2011**, *83* (16), 1–9. https://doi.org/10.1103/PhysRevB.83.165428.

(16) Wang, D.; Cui, X.; Xiao, Q.; Hu, Y.; Wang, Z.; Yiu, Y. M.; Sham, T. K. Electronic Behaviour of Au-Pt Alloys and the 4f Binding Energy Shift Anomaly in Au Bimetallics- X-Ray Spectroscopy Studies. *AIP Adv.* **2018**, *8* (6). https://doi.org/10.1063/1.5027251.

(17) Lindau, I.; Pianetta, P.; Yu, K. Y.; Spicer, W. E. Photoemission of Gold in the Energy Range 30-300 eV Using Synchrotron Radiation. *Phys. Rev. B* **1976**, *13* (2), 492–495. https://doi.org/10.1103/PhysRevB.13.492.

(18) Henke, B. L.; Gullikson, E. M.; Davis, J. C. X-Ray Interactions: Photoabsorption, Scattering, Transmission, and Reflection at E=50-30000 eV, Z=1-92. *At. Data Nucl. Data Tables* **1993**, *54* (2), 181–342.

(19) Barton, S. W.; Goudot, A.; Bouloussa, O.; Rondelez, F.; Lin, B.; Novak, F.; Acero, A.; Rice, S. A. Structural Transitions in a Monolayer of Fluorinated Amphiphile Molecules. *J. Chem. Phys.* **1992**, *96* (2), 1343–1351. https://doi.org/10.1063/1.462170.

(20) Hinterwirth, H.; Kappel, S.; Waitz, T.; Prohaska, T.; Lindner, W.; Lämmerhofer, M. Quantifying Thiol Ligand Density of Self-Assembled Monolayers on Gold Nanoparticles by Inductively Coupled Plasma-Mass Spectrometry. *ACS Nano* **2013**, *7* (2), 1129–1136. https://doi.org/10.1021/nn306024a.

(21) Thorman, R. M.; Kumar TP, R.; Fairbrother, D. H.; Ingolfsson, O. The Role of Low-Energy Electrons in Focused Electron Beam Induced Deposition : Four Case Studies of Representative Precursors. *Beilstein J. Nanotechnol.* **2015**, *6*, 1904–1926.

https://doi.org/10.3762/bjnano.6.194.

(22) Ogletree, D. F. Chapter 2 - Molecular Excitation and Relaxation of Extreme Ultraviolet Lithography Photoresists. In *Materials and Processes for Next Generation Lithography*; Robinson, A., Lawson, R. B. T.-F. of N., Eds.; Elsevier, 2016; Vol. 11, pp 91–113. https://doi.org/https://doi.org/10.1016/B978-0-08-100354-1.00002-8.

(23) Torok, J.; Del Re, R.; Herbol, H.; Das, S.; Bocharova, I.; Paolucci, A.; Ocola, L. E.; Ventrice, C.; Lifshin, E.; Denbeaux, G.; Brainard, R. L. Secondary Electrons in EUV Lithography. *J. Photopolym. Sci. Technol.* **2013**, *26* (5), 625–634. https://doi.org/10.2494/photopolymer.26.625.

Chapter 4

Bottom-Up Nanofabrication with Extreme Ultraviolet Light: Metal-Organic Frameworks on Patterned Monolayers*

Abstract

The fabrication of integrated circuits with ever smaller (sub-10 nanometer) features poses fundamental challenges in chemistry and materials science. As smaller nanostructures are fabricated, thinner layers of materials are required, and surfaces and interfaces gain a more important role in the formation of nanopatterns. We present a new bottom-up approach in which we use the high optical resolution offered by extreme ultraviolet (EUV) lithography to print patterns on self-assembled monolayers (SAM). Upon irradiation, low-energy electrons induce chemical changes in the SAM so that the projected image is transferred to the substrate's surface. We use the chemical differences between exposed and unexposed regions—chemical contrast—to promote a selective growth of inorganic-organic hybrid structures that can act either as an etch-resistant layer for further pattern transfer or that can be used as functional nanostructures. The method demonstrated its ability to produce nm-scale line/space patterns in thin films of metal-organic frameworks (MOFs). Moreover, its potential for independent tuning of the different steps of the EUVL process (photo-induced chemistry, spatially resolved chemical contrast, and formation of nanopatterns) represent an advantage over current top-down approaches, in which the same material plays all roles, by providing numerous opportunities for optimization.

* Lugier, O.; Thakur, N.; Wu, L.; Vockenhuber, M.; Ekinci, Y.; Castellanos, S.; "Bottom-up nanofabrication with extreme ultraviolet light: metal-organic frameworks on patterned monolayers"; manuscript under revision.

4.1 Introduction

The semiconductor industry has become a point of intersection between economics and fundamental science as a result of a prediction known as Moore's law.[1] The claim that the number of transistors in a computer chip had to double every two years now translates into a demand for integrated circuits of 8 nm size by 2028.[2] To satisfy this economic interest, a long path of technological challenges culminated in the shift of the light source used in photolithography from 193 nm to 13.5 nm wavelength (extreme ultraviolet, EUV), in order to gain optical resolution. The release of the first devices branded "EUV-inside" to the consumer market in 2020 marked a significant milestone for EUV lithography (EUVL). However, manufacturing nanostructures of sub-10 nm dimensions with such energetic photons opens fundamental questions at the interface of chemistry, physics, and materials science.

Detailed knowledge on how EUV radiation interacts with matter is crucial to design photosensitive materials that resolve the projected images into nanopatterns, *i.e.* photoresists.[3–7] In particular, the role of the electron cascade generated after photoionization, the mechanisms leading to the resist's solubility switch, the influence of applied post-exposure procedures, and the blur resulting from the aforementioned processes are still being investigated.[8,9] Furthermore, as the nanopatterns' size decreases, thinner photoresists are required to avoid high aspect ratios and pattern collapse,[10,11] which has two main consequences from a scientific perspective: 1) a more efficient EUV absorptivity is needed; 2) the roles of interfaces (photoresist-vacuum and photoresist-wafer) become more important for the formation of the nanostructures. Consequently, new concepts and designs of systems that can effectively react to radiation with nanoscale spatial resolution should be explored and accompanied by investigations of the fundamental aspects of their functioning to fulfil the requirements of upcoming nanofabrication technologies.

Here, we propose an alternative to the classical photoresist concept by using an organic Self-Assembled Monolayer (SAM) as photoresist material in a novel bottom-up approach consisting of three main patterning steps: 1) exposure; 2) thiol exchange; 3) selective growth (Fig. 4.1). Monolayers of thiols are virtually transparent to 92 eV photons[12] but sensitive to low energy electrons, which are generated mainly from the photoionization of the substrate underneath. Upon irradiation (step 1), thiol SAMs undergo multiple chemical and structural changes, including packing disorder and decrease of the SAM stability, which create chemical differences between the exposed and unexposed areas at the surface of the functionalized substrate, referred to as chemical contrast.[13–16] Thanks to this, the exposed areas can be selectively replaced by different thiol species through immersion of the substrate in a solution containing the new thiols (step 2, post-exposure exchange). In this way, the chemical contrast of the patterns is enhanced, enabling subsequent surface modifications on

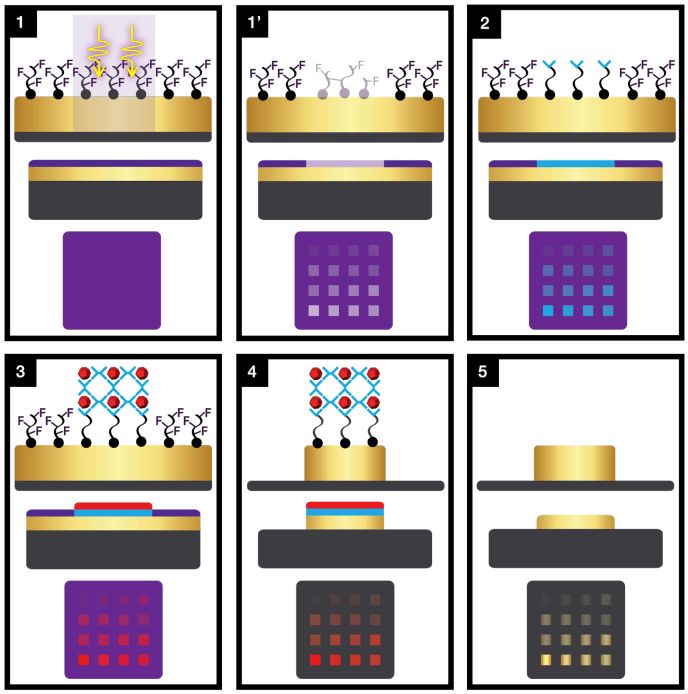

Figure 4.1: Schematic representation of a sample through each step of the bottom-up procedure. **(1)** EUV exposure of the sample; **(1')** structure of the sample post EUV irradiation; **(2)** selective exchange procedure by replacing thiols on the damaged SAM areas; **(3)** selective SURMOF growth on exchanged areas; **(4)** etching of the areas not protected by the SURMOF; **(5)** stripping of remaining SURMOF material. In each box, from top to bottom, the drawings represent the sample at the molecular level, its cross-section, and its top view. In this work, steps 1 to 3 are investigated in detail and steps 4 and 5 are presented as a proof of concept.

exposed or unexposed areas.[17] DNA,[18,19], nanoparticles,[20,21] quantum dots,[22,23] and materials such as surface-mounted metal-organic frameworks (SURMOFs)[24] or perovskites[25,26] can be deposited with various levels of selectivity on surfaces endowed with spatially resolved chemical contrast.[27] In this work, the chemical contrast obtained from the EUV exposure and thiol-exchange procedure is used to promote the growth of a SURMOFs on the exposed areas (step 3), which can later act as a protective layer for the etching step and enable the transfer pattern to the underlying substrate (step 4 and 5). Notice that our approach can also be used to fabricate nanostructures of functional SURMOFs for other applications if the sequence is terminated at step 3 or 4.

We observed that surface chemical contrast is obtained at doses near the industry target (20-25 mJ/cm^2). Furthermore, an advantage of this strategy is that each step can be tuned

independently—the type of initial SAM and that of the replacing thiol, type of structure grown on the patterned monolayer—, thus giving a large room for optimization and opportunities for fundamental investigations. We believe that the bottom-up approach here presented to be a breakthrough for building nanostructures over large areas in a cost-effective time.

4.2 Experimental

The chemical reagents used in this work were ordered from Sigma Aldrich and used as such.

4.2.1 Sample preparation and thiol functionalization

Polycrystalline gold surfaces were prepared by sputter coating (Leica EM ACE600) clean silicon substrates with a 5-nm adhesion layer of chromium followed by a 50-nm layer of gold.

Initial functionalization of the gold surfaces was conducted by immersion in an ethanol solution of 1H,1H,2H,2H-Perfluoro-1-decanethiol (HFDT) at a concentration of 2 mM during 24h, following reported standard procedures.[117] The hydrophobicity of the monolayers was determined using simple static water contact angle measurements. Typical values ranged from 100° to 110°.

The exchange of the EUV-exposed thiols was similarly conducted by immersion in ethanol solutions of 4-mercaptomethyl benzoic acid or 4-pyridylethyl mercaptan, at a concentration of 6 mM for 18 h or 48 h.

4.2.2 EUV exposure

Open frame exposures (pads) were performed by exposing areas of 1.7 × 1.7 mm^2 (pinhole 70 μm) or 0.5 × 0.5 mm^2 (pinhole 30 μm) while line/space patterns were obtained via EUV interference lithography. Both pads and line/space patterns were exposed to a wide range of EUV doses.

All EUV exposures were done at the XIL-II beamline at the Swiss Light Source (SLS) synchrotron in the Paul Scherrer Institute (PSI).[78]

4.2.3 Post-exposure procedures and analysis

Thiol exchange

The exchange procedures consist in the immersion of the samples into a 6 mM ethanol solution of either 4-mercatptomethyl benzoic acid (MBA) or 4-pyridylethyl mercaptan (4pyr), at room temperature during 18h or 48h. After the procedure, the samples are gently rinsed with pure ethanol and dried with under nitrogen flow.
The reference samples are treated following the same procedure with pure ethanol solutions.

Imaging

The features on exposed-only or exposed-and-exchanged monolayers were characterized by SEM (FEI VERIOS 460) at energies of 2 keV or 5 keV and beam currents of 0.1 nC or 0.4 nC. The SEM images of grown SURMOFs were then taken at 5 keV and beam current of 100 nC.
AFM images were taken on a Bruker Scan-Assist AFM in contact mode with the silicon nitride Bruker Scan Assist-Air tips and the data treatment was carried on using Nanoscope software version 9.0.

SURMOF growth

SURMOFs were grown using layer-by-layer Liquid Phase Epitaxy using a homemade automatized system with control over the temperature, time of immersion, stirring and sonication. Up to six samples can be subjected to the synthetic procedure at the same time, allowing for simultaneous growth and more reliability in results comparison.
A growth cycle consists in 15 minutes of immersion in a 1 mM copper acetate hexahydrate solution, $Cu(OAc)_2 \bullet 6H_2O$, followed by 3 minutes of rinsing in pure ethanol, followed by 30 minutes of immersion in a 0.2 mM solution of trimesic acid (TMA), ended by 3 minutes of rinsing in pure ethanol.
The reagents solutions were kept at 50 °C. Each sample went through 15 cycles of growth.

X-Ray Photoelectron Spectroscopy (XPS)

XPS spectra were obtained on a homebuilt system from the Zernike Institute for Advanced Material at the University of Groningen (The Netherlands) with a VG Microtech CLAM 2 hemispherical analyzers and a non-monochromatic Al Kα source (1486.6 eV, operating at 10 kV, 34 mA, 30° source).
The fittings of the spectra were done using the Unifit software version 2018.

Profilometer

The thickness measurements of the SURMOF layers for the growth curves (SURMOF thickness as a function of the initial EUV dose) were obtained using a KLA-Tencor alpha-step 500 profilometer.

Static water angle contact (WCA)

The WCA pictures were taken using a homebuilt system. Images were taken with an Apple camera and the software miXscope. Image analysis was conducted with the software imageJ using the drop analysis LB-ADSA plug-in.

4.3 Results and discussion

4.3.1 Steps 1, 1' and 2: EUV exposure and post-exposure exchange

In our previous study,[28] we showed that a thiol monolayer rich in fluorine, 1H,1H,2H,2H-Perfluoro-1-decanethiol (HFDT), on Au is chemically changed when exposed to EUV light and found that at a dose of 200 mJ/cm^2 ~ 40% of fluorine is lost. The secondary electrons and holes generated upon EUV absorption trigger these chemical changes. Such changes in the chemical composition of the SAM necessarily introduce disorder in its packing, as reported in studies on the impact of low-energy electron irradiation on similar systems.[13]

Thiol monolayers are known to undergo desorption and exchange when immersed in a solution containing another thiol species, creating a mixed monolayer composed of both thiols. The rate of that desorption depends on various parameters such as the temperature, the type of solvent, the type of thiols used, and, most importantly, the quality of the packing of the initial monolayer.[29] Regarding the influence of the packing, faster exchange rates are observed for increasing disorder while defect-free regions remain integer.[30]

In this work, we study the exchange process of EUV-irradiated HFDT monolayers using 4-mercaptomethyl benzoic acid (MBA) and 4-pyridylethyl mercaptan (4pyr) as replacing thiols. Their distinct chemical structures, as compared to HFDT, are expected to limit intermolecular interactions between the different SAMs, hence disfavor the formation of mixed domains and increase the chemical contrast between areas coated with HFDT and MBA or 4pyr. More importantly, both MBA and 4pyr act as nucleation sites for surface-anchored metal-organic frameworks (SURMOFs) such as HKUST-1(Cu); an essential property for step 3 of our bottom-up approach (see below).

For a first assessment of the exchange procedure, a "hydrophobicity test" was performed following the step 2 of the procedure (Fig. 4.2a). SAMs composed of MBA and 4pyr have opposite wetting properties to the ones of HFDT. The former are hydrophilic (static water contact angle ~20° and ~60°, respectively), while fluorinated SAMs are highly hydrophobic (static water contact angle ~120°).[31] Soaking the surface of the samples with a polar solvent revealed the exchanged areas. The solvent drips away from the highly hydrophobic pristine monolayers while small volumes remain confined on the hydrophilic domains (Fig 4.2b and Fig. S4.1 and Video S1 in Supporting Information). Although for certain processing conditions this phenomenon was also observed in non-exchanged samples, the dose threshold is significantly lowered with the exchange step (from ~250 mJ/cm^2 to ~75 mJ/cm^2 in samples with 500 µm × 500 µm exposed areas). The hydrophobicity of HFDT monolayers originates from their high concentration of fluorine atoms. Thus, this hydrophobicity test supports our previous *in-situ* XPS study, in which the F-loss was evidenced,[28] and reveals on a macroscopic scale the chemical contrast between unexposed and exposed and exchanged areas. This fact also evidences that the replacement of thiols on exposed areas by a different thiol species is favored.

Aiming at a more detailed inspection of the chemical contrast between exposed (and exchanged) and unexposed regions, Scanning Electron Microscopy (SEM) was performed on selected samples (Fig. 4.2c). We could image the different SAM domains present at the surface of the substrates. The exposed/exchanged areas appear darker than the unexposed background in the images. The observed trend is that higher contrast is obtained for increasing exposure doses, regardless of the exchange procedure. Even the reference samples, immersed in pure ethanol after exposure instead of a thiol-containing solution, show contrasting exposed areas. This is another indication that EUV radiation induces chemical changes in the SAM, even at relatively low doses (25 mJ/cm^2).

MBA-exchanged samples display a less marked contrast. We speculate that this phenomenon might originate from a faster exchange of the unexposed areas for this species, in agreement with the aforementioned reports on the stability of thiol SAMs in solution.[30] Another hint for this is the erosion of the Au layer for these samples. We conclude that the degradation of the Au layer by this acidic thiol also is a consequence (and an accelerating factor) of the exchange on unexposed regions. In general, darker regions originate from a lower density of backscattered electrons. Whether this is due to fewer electrons from the Au substrate escaping through the SAM (*e.g.*, because the irradiated thiols generate a crosslinked C-network) or from fewer electrons being generated from the SAM (*e.g.*, because of fewer F-atoms present) cannot be easily distinguished. Therefore, although SEM proved a good method to spot dose thresholds and qualitative trends, a quantitative analysis cannot be extracted from SEM data.

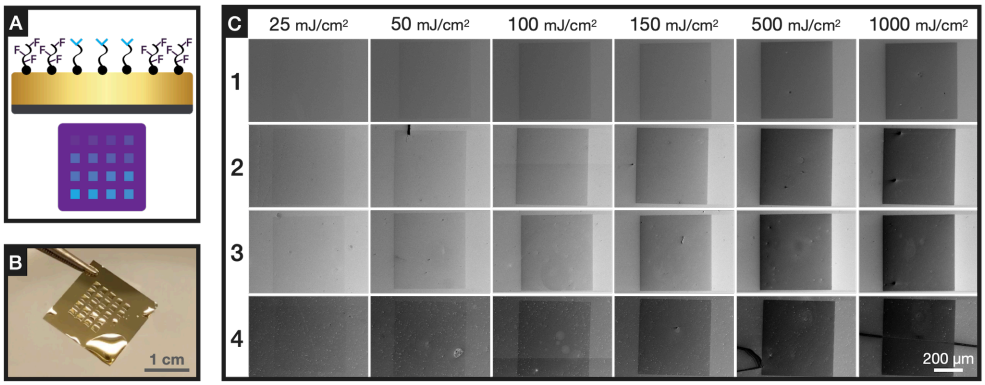

Figure 4.2: (**A**) Schematic representation of the samples (molecular level and top view) after the EUV-exposure (multidose) and exchange procedure of our bottom-up approach for EUVL. (**B**) Photograph of an HFDT-functionalized gold substrate after EUV exposure and exchange procedure in an MBA solution. The picture shows the sample a few seconds after being taken out of ethanol. The difference in hydrophobicity between pristine areas and EUV-exposed and MBA-exchanged areas (1.7 mm × 1.7 mm pads) is revealed as the hydrophilic solvent drips away from hydrophobic surfaces (non-exchanged areas) but remains on hydrophilic surfaces (exchanged areas). (**C**) Compilation of SEM images of 500 µm × 500 µm pads obtained on HFDT monolayers via EUV exposure and exchange in a solution of MBA or 4pyr. Different exchange procedures were conducted, such as (1) non-exchanged, (2) pure ethanol 48 h, (3) 4pyr (6 mM) 18 h, (4) MBA (6 mM) 18 h. On these images, the exposed/exchanged areas appear darker than the pristine background.

In an attempt to monitor the efficiency of the post-exposure exchange process, we used X-ray photoelectron spectroscopy (XPS) on MBA-exchanged samples for various EUV doses and exchange procedures. In XPS, the position of the peaks in the binding energy scale reveals which elements are present in a sample, and small variations around that position indicate the oxidation state of each specific element or the propensity for electron withdrawing of its substituents (chemical shift). Monitoring the area of the peak in the F 1s region of the spectra allows for detecting changes in the concentration of fluorine. In addition, HFDT and MBA display distinctive features in the C 1s spectrum as they contain C-F and COO species, respectively, which give rise to peaks with different chemical shifts. The C 1s spectra in Figure 4.3a are normalized in intensity to detect changes in the number of components with different chemical shifts in the C 1s envelope, as an indication of changes in the chemical composition of the samples after each step. Notice that the signal at 285 eV is most likely mainly arising from adventitious carbon. The F 1s spectra in Figure 4.3b are normalized to the area of the Au 4f peak to capture the relative fluorine loss and show, as a function of the dose, how much of this loss is induced by the post-exposure exchange procedures

The C 1s spectra after EUV irradiation show a decrease in the intensity of the CF_2/CF_3 components (*ca.* 290 eV). The F 1s spectra show a significant decrease in intensity of the fluorine peak (687.6 eV, see also Fig. S4.9 in Supporting Information), in line with our previous *in-situ* irradiation studies, denoting the partial desorption of full HFDT molecules and/or outgassing of fluorine-containing fragments.[28] The + 0.3 eV blueshift of the F 1s peak implies slight changes in the chemical environment of F atoms, presumably from structural reorganizations of the fluorocarbon chains of the monolayer upon exposure.[32]

The 18 h exchange procedure yields a widening of the C 1s components assigned to C-H sp^2/sp^3 carbon species as the dose increases. This is an indication that new carbon species are incorporated in the SAM, thus adding components on the higher energy range. We hypothesize that exchanged samples consist of a mixture of partially fluorinated and unsaturated carbon chains and MBA thiols. Thus, although pure MBA does not display prominent features at this BE, such assortment of molecules generates a distribution of intermolecular interactions that lead to a broadening and shift of the C 1s signal. In addition, the carboxylic carbons (COO) of the MBA molecules have binding energies around 288 eV,[32,33] so that a certain contribution of these electrons is expected. We also observe a decrease in intensity for the CF_2/CF_3 components and of the F 1s peak along with the dose increase. Yet, the + 0.3 eV shift seems unaffected. This might indicate that some of the fluorine-containing products remain after exchange. The same trends are registered in the 48 h exchange procedure yet with a more significant loss of fluorine content (Fig. 4.3b).

The qualitative comparison of the chemical composition of the various systems provides valuable insights on the mechanisms that take place during the procedure. Combined with the previously discussed hydrophobicity test, SEM inspection and our previous F-loss studies[28], these XPS results indicate that both desorption and incorporation of new species occur during the exchange procedure on areas irradiated by EUV photons.

4.3.2 Step 3: SURMOF growth

For the final step of the bottom-up procedure, HKUST-1(Cu) is grown as a SURMOF on the surface of the EUV-exposed (and exchanged) samples via layer-by-layer (LbL) liquid phase epitaxy (LPE).[34] Contrarily to pyridyl- and carboxyl-terminated SAMs, CF_3-terminated SAMs such as HFDT are known to be unsuitable for the growth of most SURMOFs, including SURMOFS of the HKUST-1 family.[35] As a result, when an HFDT-functionalized substrate that has been exposed to EUV (multiple pads with increasing dose) is used for the LbL-LPE step, HKUST grows preferably on the exposed areas. As discussed earlier, EUV irradiation of fluorinated alkane thiols triggers the loss of fluorine and fluorine-containing fragments through bond cleavage and outgassing. In other words, exposing HFDT to increasing EUV doses depletes the SAM of its fluorine content, effectively transforming the

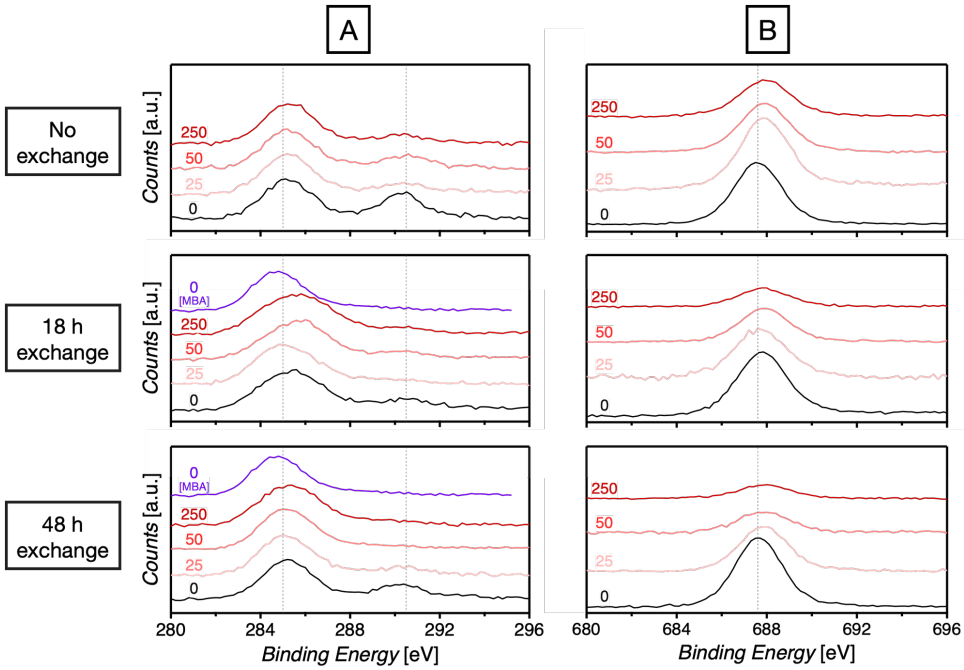

Figure 4.3: XPS spectra of (**A**) the C 1s region and (**B**) the F 1s region of the exposed samples (left), 18 h MBA-exchanged samples (middle) and 48 h MBA-exchanged samples (right) for various EUV doses. The numbers on each curve indicate the EUV dose received by the sample in mJ/cm2. The C 1s spectra of a pristine MBA-functionalized gold sample was added for comparison. The C 1s spectra (**A**) are normalized to their maximum intensity and the F 1s spectra (**B**) are normalized to the intensity of the gold signal of the substrate. Indicators are set at 285.0 eV and 290.3 eV for the C 1s spectra (A) and 687.5 eV for the F 1s spectra (B).

fluorinated thiols of such areas into alkane/alkene-rich thiols and creating favourable domains for HKUST-1(Cu) growth.

The effect is clearly enhanced when the exposed HFDT SAM is exchanged with 4pyr or MBA (Fig. S4.6 in Supporting Information). That is, the SURMOF growth is favored at lower EUV doses if the new thiols are incorporated during an exchange procedure. The homogeneity of the SURMOF layers of the pads improves with increasing EUV dose. Usually, low doses yield colorless chips of transparent material randomly placed within the exposed area and high doses yield brown, fully homogeneous and opaque thin films. The aspect of intermediate doses can vary depending on the size of the exposed area, the exchange method and the growth conditions. But, in general, it gives blue-ish, mostly homogeneous and opaque layers of HKUST-1(Cu) (Fig. S4.6 and S4.7 in Supporting Information).

Profilometer and atomic force microscopy (AFM) reveal that the transparent films formed on areas exposed to medium doses are thicker and composed of bigger crystals than the opaque layers obtained when high EUV doses were used (Fig. 4.4 and 4.6d). As each MBA or 4pyr thiol is a potential nucleation point for the SURMOF, the number of nucleation points available for MOF crystals to nucleate is correlated to the efficiency of the thiol exchange step. We hypothesize that the differences in thickness and roughness between layers grown on areas exposed to high and low doses stem from disparities in the availability of such nucleation sites at the surface. On high-dose areas where a larger number of photons hits the surface, the crystals nucleate closer to each other resulting in an early coalescence and the formation a smoother, more homogeneous film. While, with fewer nucleation points available over the same area, low dose patterns promote the development of discrete islands of material. Similar observations were reported on the properties of SURMOFs grown on seeded substrates, another synthetic method used to grow MOFs on a surface.[36]

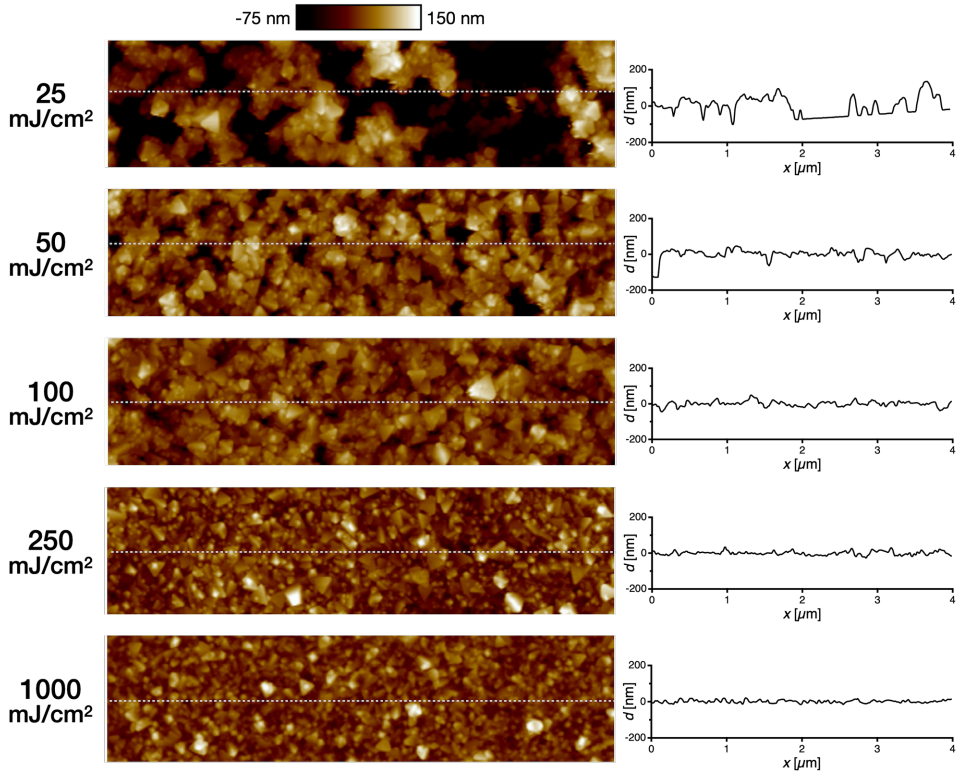

Figure 4.4: AFM images (4 µm × 1 µm; contact mode) of the thin films of HKUST-1(Cu) taken at the centre of the pads (exchange procedure: 4pyr, 6 mM, 48 h). The height profiles along the white dotted lines are displayed on the right and illustrate the evolution of the surface roughness as a function of the EUV dose.

It is worth mentioning that extensive crosslinking is expected to take place at high doses as the SAM experiences more fragmentation and desorption from sustained EUV irradiation. This might prevent the full exchange of the exposed thiol, as indicated by the presence of F after long exchange in the XPS spectra (Fig. 4.3). The same phenomenon was reported on thiol SAMs following their exposure to high doses of low energy electrons.[37] In this situation of over-exposure, the surface of the sample is expected to be covered by polymerized alkane or alkene species which form matrices bonded to the substrate at multiple points, thus disfavor exchange with other thiols. Nonetheless, the chemical contrast created at such high doses between the now CH_2/CH_3 terminated exposed areas and the CF_2/CF_3 terminated pristine areas can be sufficient to enable preferential growth or deposition (Fig. 4.5). For example, HKUST-1(Cu) has been shown to grow with remarkable efficiency on alkane terminated SAM.[38]

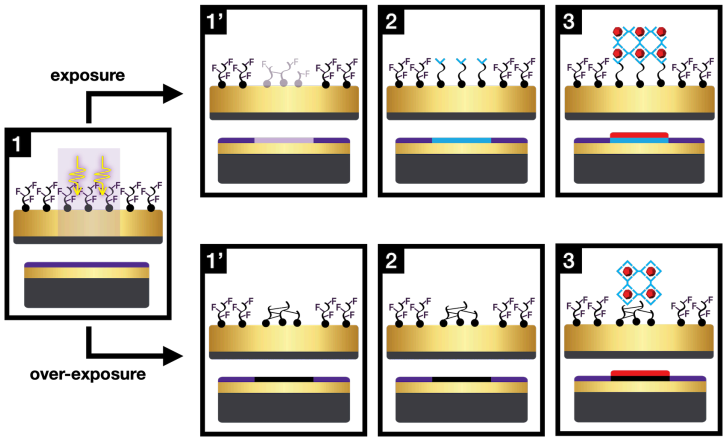

Figure 4.5: Schematic representations of samples exposed at an optimal dose (top) and samples that were over-exposed (bottom) at the various steps of our bottom-up approach for EUVL.

Although preferential nucleation is obtained on exposed and exchanged areas, the pristine domains of the samples are not devoid of material. Thin chips of material are found on pristine areas. They are either weakly bonded to the substrate or sprouting from the edges of homogeneous SURMOF layers; sometimes bridging two adjacent exposed areas (Fig. S4.2 in Supporting Information). They are clearly not attached to the surface, as sonication in pure solvent removes them without apparent damage to HKUST-1(Cu) layers grown on exposed areas. Undesired deposition of MOF on unexposed areas could be avoided by further optimizing the SURMOF growth conditions.

4.3.3 Nanolithographic performance

The thickness of the SURMOF layer grown on exposed samples after two different procedures (18 h and 48 h of exchange step with MBA) as a function of dose are plotted in Figure 4.6. This plot is the equivalent of the contrast curve of a photoresist in conventional lithography and provides information regarding the sensitivity of a resist material in specific conditions. Here, the key information is the minimum dose required to favor HKUST growth. We noticed that, in the tested conditions and for the specific exposed area sizes (1.7 × 1.7 mm^2), this dose threshold is *ca.* 55 mJ/cm^2 for the 18 h-exchange (inhomogeneous patches are found already at 7.5 mJ/cm^2, empty squares in Fig. 4.6) and *ca.* 35 mJ/cm^2 for the 48 h-exchange one. Assuming a packing of 2 to 4 molecules of HFDT per square nanometer, 40 mJ/cm^2 corresponds to approx. 12 to 6 incident photons per molecule, respectively. However, it should be noticed that the SAM has an EUV transmittance of *ca.* 98%. Most photons are thus absorbed by the gold substrate and lead to an electron cascade in the Au layer, from which only the escaping electrons induce damage to the SAM on top. Taking into account that the inelastic mean free path of electrons of 80 eV is estimated ~ 5 Å in Au,[39,40] electrons generated in Au upon absorption of EUV photons would only escape from the upmost 1.5 nm. This thin layer would absorb 7% of the photons that go through the SAM, meaning that overall approximately only 9% of the incident photons are absorbed by the SAM/Au system. Yet, it is not straightforward to determine how many of these escaping electrons interact with the SAM. Therefore, the actual efficiency of the process is not yet known but can be further tuned using other substrates and monolayers. Remarkably, the dose thresholds for growth are close to the values targeted by the semiconductor industry (20 mJ/cm^2).[41,42]

Dense lines patterning was performed with EUV interference lithography as a preliminary investigation of the nanolithographic capability, in terms of resolution, of the bottom-up approach in the studied conditions. Line/space optical patterns created with EUV interference lithography were projected on the HFDT monolayer at various half-pitch (HP) values, *i.e.*, 22 nm, 30 nm, 40 nm and 50 nm, using different EUV doses (on wafer), namely 25 mJ/cm^2, 50 mJ/cm^2, 100 mJ/cm^2, 250 mJ/cm^2 and 500 mJ/cm^2. Only the 50 nm-HP patterns exposed at 500 mJ/cm^2 are resolved enough to be observed with SEM after MBA-exchange (Fig. 4.7a). On 4pyr-exchanged samples, SEM images reveal 50 nm HP lines from 100 mJ/cm^2 onward, 40 nm HP from 250 mJ/cm^2 onward and 22 nm HP for 500 mJ/cm^2 only (Fig. S4.4 and S4.5 in the Supporting Information).

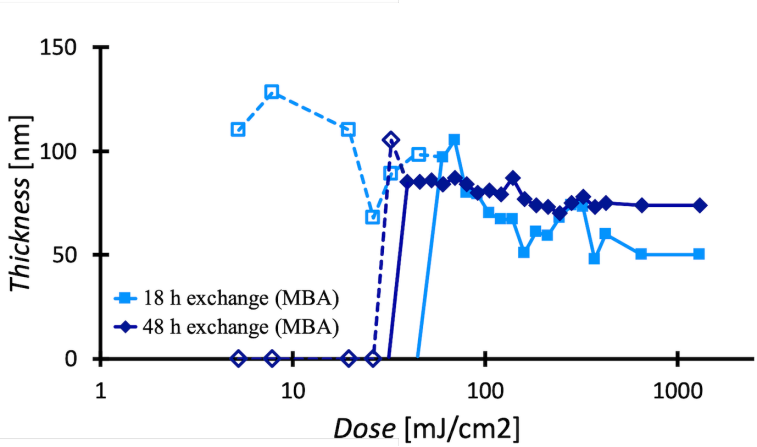

Figure 4.6: Thickness of HKUST-1(Cu) on MBA-exchanged pads as a function of EUV dose. The MBA pads were obtained from open-frame EUV exposures and MBA-exchange on a HFDT monolayer on Au. The hollow markers and dotted lines represent thickness values of inhomogeneous HKUST-1(Cu) layers. The dose thresholds for homogeneous HKUST-1(Cu) layers are indicated by the continuous lines crossing the x-axis at around 35 mJ/cm^2 and 55 mJ/cm^2, respectively, for the 48 h procedure and 18 h procedure.

The limited resolution of the SEM images, due to the invasive nature of this technique and the low contrast between exposed (and exchanged) lines and unexposed spaces (comprising HFDT), hinders the evaluation of the pattern quality. Therefore, defects related to photoelectron blur and defects like bridging or line discontinuity cannot be properly assessed from these images, especially for the lowest pitches and doses. Nevertheless, these images confirm that nanometre-scale patterns can be obtained with this method.

After the exposure and exchange steps, HKUST-1(Cu) was grown on the line/space patterned monolayers to study whether the chemical contrast provided by the surface can be propagated to the SURMOF structure and to study the impact of the growth step on the pattern resolution. On MBA-exchanged samples, SEM images show the crystals at the surface of the thin films arranged following a repetitive pattern of parallel lines (Fig. 4.7b and 4.7c). The spatial alignment of individual crystals indicates that the SURMOF growth was influenced by the underlying patterned SAM. However, the HKUST-1(Cu) crystal shape hinders the formation of straight edges in the line/space patterns. When anchoring points are present in the substrate, this MOF tends to grow in the [111] crystalline direction. This growth leads to the formation of cube-like crystals with one corner pointing upwards, as it can be observed in the AFM images (Fig. 4.4). This causes the horizontal expansion of the lines and their subsequent merging (Fig. 4.6b), a phenomenon also observed between some patterns obtained via open-frame exposures (Fig. S4.2 in Supporting Information). In addition, the size (40 nm to 250 nm) of the crystallites of HKUST-1 obtained from these synthetic

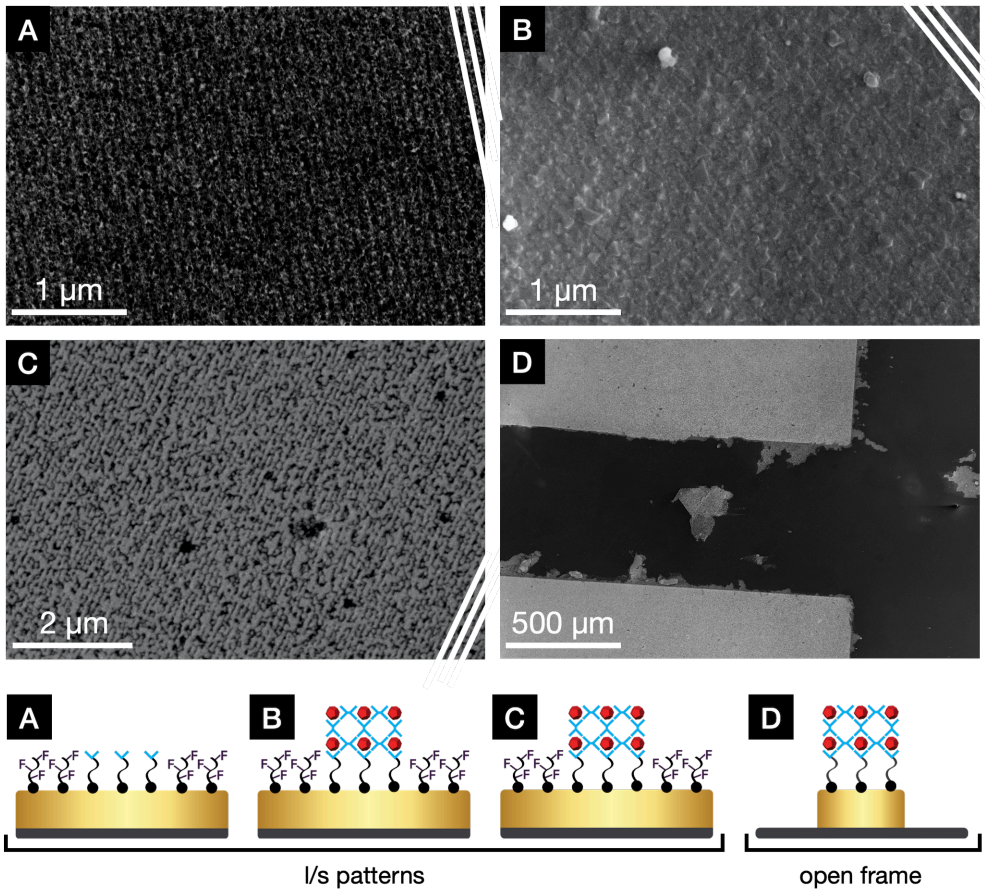

Figure 4.7: (A) Edited (contrast and brightness) SEM picture of line/space patterns (half-pitch: 50 nm; dose: 500 mJ/cm^2) obtained via EUV patterning and exchange procedure (MBA, 6 mM, 48 h) on a HFDT monolayer on Au. The original image is available in Fig. S4.3 in the Supporting Information. **(B)** and **(C)** SEM images of line/space patterns (half-pitch: 50 nm; dose: 500 mJ/cm^2) in a thin film of HKUST-1(Cu) obtained with the following procedure: EUV patterning on a HFDT monolayer on Au, exchange in ethanol (MBA, 6 mM, 48 h) and 15 cycles or 7 cycles, respectively for **(B)** and **(C)**, of layer-by-layer LPE growth. **(D)** SEM pictures of two adjacent pads after Au etching. Au appears white and the underlying substrate (5 nm layer of Cr on Si) black.

conditions is larger than the printed HP. The smaller crystallites obtained from a shorter growth procedure (Fig. 4.7 c) enable the formation of distinct lines of HKUST-1(Cu) and confirms the presence of the nanometer-scale chemical pattern in the SAM. Using a different SURMOF platform with a preferred anisotropic growth, *i.e.*, pillar-layered MOFs such as DMOF (Cu, Co, Zn),[43] is expected to improve the resolution and overall performance of the procedure.

Note that to use the bottom-up approach as an alternative to traditional photoresists, the primary objective of the material deposition for contrast enhancement is to provide an etch resistance for future pattern transfer. Thus, the most relevant threshold here is the minimal dose needed to obtain a homogeneous layer of HKUST deposited on the exposed areas, which stands at around 35 mJ/cm^2 for the conditions investigated in this work.

Step 4 and 5

Finally, as a proof of concept for steps 4 and 5 of the procedure (Fig. 4.1), we tested HKUST-1(Cu) as an etch-mask for the transfer of the pattern to the substrate, the ultimate role of a photoresist. Samples prepared with the bottom-up approach were etched in a potassium iodide solution, a common etching agent for Au. After etching, SEM images show that the gold layer remains only on the areas that were previously covered by MOF layers while the pristine domains of the substrate are stripped. (Fig. 4.7d and Fig. S4.8 in Supporting Information).

Only samples exposed with open frame exposures were etched as the resolution of the l/s patterns post growth was too poor to enable pattern transfer to the substrate.

4.4 Conclusions

In this work, we have demonstrated that surface chemical contrast can be attained by exposing monolayers of fluorinated thiols on Au substrates to EUV light at doses close to the industrial requirements for the fabrication of future integrated circuits using EUV lithography. Although the metrology of dense-line patterns on monolayers needs to be optimised, we observed the printing of 50 nm lines on such systems. Exchanging the damaged fluorinated thiols after EUV exposure with N-terminated or COO-terminated thiols favors the selective growth of anchored metal-organic frameworks on the exposed areas. In the particular conditions used in the present work, the dose threshold to obtain homogeneous growth is 35 mJ/cm^2. Yet, we presume that at high doses, the crosslinking induced by EUV radiation on the fluorinated thiol is sufficient to promote such growth without the need of an exchange step. The chosen material for the growth step, HKUST-1(Cu), proved to act as an etch-protective layer for Au etching.

The efficiency and resolution capabilities of the bottom-up method have strong potential for improvement thanks to the high number of variables for optimisation that it conveys. One could, for example, tune the experimental conditions of the exchange step to improve pattern quality by increasing the purity of the SAM domains or select SURMOF species that grow anisotropically normal to the substrate, preventing lateral resolution loss. Even the core-principles of the method can be tuned by choosing different types of monolayers, materials

or substrates. Finally, because our bottom-up approach stands out as compared to more conventional EUVL methods, we are confident that its optimisation and fine-tuning will unravel valuable insights on the fundamental aspects of this nanopatterning technique.

Bibliography

(1) Moore, G. Cramming More Components onto Integrated Circuits. *Electronics* **1965**, *38* (8).

(2) IEEE International Roadmap for Devices and Systems™ https://irds.ieee.org (accessed Jan 2, 2020).

(3) Narasimhan, A.; Wisehart, L.; Grzeskowiak, S.; Ocola, L. E.; Denbeaux, G.; Brainard, R. L. What We Don't Know About EUV Exposure Mechanisms. *J. Photopolym. Sci. Technol.* **2017**, *30* (1), 113–120. https://doi.org/10.2494/photopolymer.30.113.

(4) Wood, O. R. EUVL: Challenges to Manufacturing Insertion. *J. Photopolym. Sci. Technol.* **2017**, *30* (5), 599–604. https://doi.org/10.2494/photopolymer.30.599.

(5) Xu, H.; Kosma, V.; Giannelis, E.; Ober, C. K.; Sakai, K. EUV Photolithography: Resist Progress and Challenges. *Proc. SPIE 10583*, **2018**. https://doi.org/10.1117/12.2302759.

(6) Levinson, H. J.; Brunner, T. A. Current Challenges and Opportunities for EUV Lithography. *Proc. SPIE; 10809*; **2018**. https://doi.org/10.1117/12.2502791.

(7) Li, L.; Liu, X.; Pal, S.; Wang, S.; Ober, C. K.; Giannelis, E. P. Extreme Ultraviolet Resist Materials for sub-7 nm Patterning. *Chem. Soc. Rev.* **2017**, *46* (16), 4855–4866. https://doi.org/10.1039/c7cs00080d.

(8) Fallica, R.; Rezvani, S. J.; Nannarone, S.; Borisov, S.; De Simone, D.; Babin, S.; Lorusso, G.; Vandenberghe, G. The Hidden Energy Tail of Low Energy Electrons in EUV Lithography. *Proc. SPIE*; 10960; **2019**. https://doi.org/10.1117/12.2514998.

(9) Ashby, P. D.; Olynick, D. L.; Ogletree, D. F.; Naulleau, P. P. Resist Materials for Extreme Ultraviolet Lithography: Toward Low-Cost Single-Digit-Nanometer Patterning. *Adv. Mater.* **2015**, *27* (38), 5813–5819. https://doi.org/10.1002/adma.201501171.

(10) Bilski, B.; Zimmermann, J.; Roesch, M.; Liddle, J.; van Setten, E.; Bottiglieri, G.; van Schoot, J. High-NA EUV Imaging: Challenges and Outlook. *Proc. SPIE*; **2019**; p 42. https://doi.org/10.1117/12.2536329.

(11) Zahlten, C.; Gräupner, P.; van Schoot, J.; Kuerz, P.; Stoeldraijer, J.; Kaiser, W. High-NA EUV Lithography: Pushing the Limits. *Proc. SPIE*; **2019**; p 43. https://doi.org/10.1117/12.2536469.

(12) Henke, B. L.; Gullikson, E. M.; Davis, J. C. X-Ray Interactions: Photoabsorption, Scattering, Transmission, and Reflection at E = 50-30,000 eV, Z = 1-92. *At. Data Nucl. Data Tables* **1993**, *54* (2), 181–342. https://doi.org/10.1006/adnd.1993.1013.

(13) Frey, S.; Heister, K.; Zharnikov, M.; Grunze, M. Modification of Semifluorinated Alkanethiolate Monolayers by Low Energy Electron Irradiation. *Phys. Chem. Chem. Phys.* **2000**, *2* (9), 1979–1987. https://doi.org/10.1039/a910314g.

(14) Zharnikov, M.; Frey, S.; Heister, K.; Grunze, M. Modification of Alkanethiolate Monolayers by Low Energy Electron Irradiation: Dependence on the Substrate Material and on the Length and Isotopic Composition of the Alkyl Chains. *Langmuir* **2000**, *16* (6), 2697–2705. https://doi.org/10.1021/la991034r.

(15) Harnett, C. K.; Satyalakshmi, K. M.; Craighead, H. G. Low-Energy Electron-Beam Patterning of Amine-Functionalized Self-Assembled Monolayers. *Appl. Phys. Lett.* **2000**, *76* (17), 2466–2468. https://doi.org/10.1063/1.126378.

(16) Yildirim, C.; Füser, M.; Terfort, A.; Zharnikov, M. Modification of Aromatic Self-Assembled Monolayers by Electron Irradiation: Basic Processes and Related Applications. *J. Phys. Chem. C* **2017**, *121* (1), 567–576. https://doi.org/10.1021/acs.jpcc.6b11269.

(17) Smith, R. K.; Lewis, P. A.; Weiss, P. S. Patterning Self-Assembled Monolayers. *Prog. Surf. Sci.* **2004**, *75* (1–2), 1–68. https://doi.org/10.1016/j.progsurf.2003.12.001.

(18) Szymonik, M.; Davies, A. G.; Walti, C. DNA Self-Assembly-Driven Positioning of Molecular Components on Nanopatterned Surfaces. *Nanotechnology* **2016**, *27* (39). https://doi.org/10.1088/0957-4484/27/39/395301.

(19) Shaali, M.; Woller, J. G.; Johansson, P. G.; Hannestad, J. K.; De Battice, L.; Aissaoui, N.; Brown, T.; El-Sagheer, A. H.; Kubatkin, S.; Lara-Avila, S.; Albinsson, B.; Jesorka, A. Site-Selective Immobilization of Functionalized DNA Origami on Nanopatterned Teflon AF. *J. Mater. Chem. C* **2017**, *5* (30), 7637–7643. https://doi.org/10.1039/c7tc01015j.

(20) Lee, S. H.; Rho, W. Y.; Park, S. J.; Kim, J.; Kwon, O. S.; Jun, B. H. Multifunctional Self-Assembled Monolayers via Microcontact Printing and Degas-Driven Flow Guided Patterning. *Sci. Rep.* **2018**, *8* (1), 1–8. https://doi.org/10.1038/s41598-018-35195-9.

(21) Yang, J.; Ichii, T.; Murase, K.; Sugimura, H. Site-Selective Assembly and Reorganization of Gold Nanoparticles along Aminosilane-Covered Nanolines Prepared on Indium-Tin Oxide. *Langmuir* **2012**, *28* (20), 7579–7584. https://doi.org/10.1021/la301042y.

(22) Ito, H.; Iio, A.; Tokuhara, K.; Sakaue, H.; Kadoya, Y.; Suzuki, H. Estimation of the Number of Quantum Dots Immobilized on an Ultra-Flat Au Surface. *Nanoscale Res. Lett.* **2017**, *12*, 0–5. https://doi.org/10.1186/s11671-017-2056-2.

(23) Wu, C.; Wang, Y.; Han, X.; Hu, X.; Cheng, Q.; Han, B.; Liu, Q.; Ren, T.; He, Y.; Sun, S.; Ma, H. Site-Selective Assembly of Quantum Dots on Patterned Self-Assembled Monolayers Fabricated by Laser Direct-Writing. *Nanotechnology* **2012**, *23* (23). https://doi.org/10.1088/0957-4484/23/23/235302.

(24) Zhuang, J. L.; Terfort, A.; Wöll, C. Formation of Oriented and Patterned Films of Metal-Organic Frameworks by Liquid Phase Epitaxy: A Review. *Coord. Chem. Rev.* **2016**, *307*, 391–424. https://doi.org/10.1016/j.ccr.2015.09.013.

(25) Wang, N.; Cheng, L.; Si, J.; Liang, X.; Jin, Y.; Wang, J.; Huang, W. Morphology Control of Perovskite Light-Emitting Diodes by Using Amino Acid Self-Assembled Monolayers. *Appl. Phys. Lett.* **2016**, *108* (14). https://doi.org/10.1063/1.4945330.

(26) Kim, G.; An, S.; Hyeong, S. K.; Lee, S. K.; Kim, M.; Shin, N. Perovskite Pattern Formation by Chemical Vapor Deposition Using Photolithographically Defined Templates. *Chem. Mater.* **2019**, *31* (19), 8212–8221. https://doi.org/10.1021/acs.chemmater.9b03155.

(27) Castellanos, S.; Verhoeven, J.; Frenken, J.; Antonov, P.; Ten kate, N.; Lugier, O. Method and Apparatus for Forming a Patterned Layer of Carbon, Method of Forming a Patterned Layer of Material. WO 2019/166409 A1, 2019.

(28) Vericat, C.; Vela, M. E.; Benitez, G.; Carro, P.; Salvarezza, R. C. Self-Assembled Monolayers of Thiols and Dithiols on Gold: New Challenges for a Well-Known System. *Chem. Soc. Rev.* **2010**, *39* (5), 1805–1834. https://doi.org/10.1039/b907301a.

(29) Gronheid, R.; Solak, H. H.; Ekinci, Y.; Jouve, A.; Van Roey, F. Characterization of Extreme Ultraviolet Resists with Interference Lithography. *Microelectron. Eng.* **2006**, *83* (4–9), 1103–1106. https://doi.org/10.1016/j.mee.2006.01.149.

(30) Lugier, O.; Troglia, A.; Sadegh, N.; van Kessel, L.; Bliem, R.; Mahne, N.; Nannarone, S.; Castellanos, S. Extreme Ultraviolet Photoelectron Spectroscopy on Fluorinated Monolayers: Towards Nanolithography on Monolayers. *J. Photopolym. Sci. Technol.* **2020**, *33* (2), 229–234. https://doi.org/10.2494/photopolymer.33.229.

(31) Srisombat, L.; Jamison, A. C.; Lee, T. R. Stability: A Key Issue for Self-Assembled Monolayers on Gold as Thin-Film Coatings and Nanoparticle Protectants. *Colloids Surfaces A Physicochem. Eng. Asp.* **2011**, *390* (1–3), 1–19. https://doi.org/10.1016/j.colsurfa.2011.09.020.

(32) Baralia, G. G.; Duwez, A. S.; Nysten, B.; Jonas, A. M. Kinetics of Exchange of Alkanethiol Monolayers Self-Assembled on Polycrystalline Gold. *Langmuir* **2005**, *21* (15), 6825–6829. https://doi.org/10.1021/la050245v.

(33) Chidsey, C. E. D.; Loiacono, D. N. Chemical Functionality in Self-Assembled Monolayers: Structural and Electrochemical Properties. *Langmuir* **1990**, *6* (3), 682–691. https://doi.org/10.1021/la00093a026.

(34) Ford, K.; Battersby, B. J.; Wood, B. J.; Gentle, I. R. The Production and Verification of Pristine Semi-Fluorinated Thiol Monolayers on Gold. *J. Colloid Interface Sci.* **2012**, *370* (1), 162–169. https://doi.org/10.1016/j.jcis.2011.10.081.

(35) Barriet, D.; Yam, C. M.; Shmakova, O. E.; Jamison, A. C.; Lee, T. R. 4-Mercaptophenylboronic Acid SAMs on Gold: Comparison with SAMs Derived from Thiophenol, 4-Mercaptophenol, and 4-Mercaptobenzoic Acid. *Langmuir* **2007**, *23* (17), 8866–8875. https://doi.org/10.1021/la7007733.

(36) Wang, Z.; Wöll, C. Fabrication of Metal–Organic Framework Thin Films Using Programmed Layer-by-Layer Assembly Techniques. *Adv. Mater. Technol.* **2019**, *4*

(5), 1–22. https://doi.org/10.1002/admt.201800413.

(37) Bradshaw, D.; Garai, A.; Huo, J. Metal–Organic Framework Growth at Functional Interfaces: Thin Films and Composites for Diverse Applications. *Chem. Soc. Rev.* **2012**, *41* (6), 2344–2381. https://doi.org/10.1039/c1cs15276a.

(38) Li, Q.; Gies, J.; Yu, X. J.; Gu, Y.; Terfort, A.; Kind, M. Concentration-Dependent Seeding as a Strategy for Fabrication of Densely Packed Surface-Mounted Metal–Organic Frameworks (SURMOF) Layers. *Chem. - A Eur. J.* **2020**, *26* (23), 5185–5189. https://doi.org/10.1002/chem.202000594.

(39) Zharnikov, M.; Geyer, W.; Gölzhäuser, A.; Frey, S.; Grunze, M. Modification of Alkanethiolate Monolayers on Au-Substrate by Low Energy Electron Irradiation: Alkyl Chains and the S/Au Interface. *Phys. Chem. Chem. Phys.* **1999**, *1* (13), 3163–3171. https://doi.org/10.1039/a902013f.

(40) Biemmi, E.; Scherb, C.; Bein, T. Oriented Growth of the Metal Organic Framework $Cu_3(BTC)_2(H_2O)_3 \cdot xH_2O$ Tunable with Functionalized Self-Assembled Monolayers. *J. Am. Chem. Soc.* **2007**, *129* (26), 8054–8055. https://doi.org/10.1021/ja0701208.

(41) Tanuma, S.; Powell, C. J.; Penn, D. R. Calculations of Electron Inelastic Mean Free Paths (IMFPS). IV. Evaluation of Calculated IMFPs and of the Predictive IMFP Formula TPP-2 for Electron Energies between 50 and 2000 EV. *Surf. Interface Anal.* **1993**, *20* (1), 77–89. https://doi.org/10.1002/sia.740200112.

(42) Naumkin, A.; Kraut-Vass, A.; Gaarenstroom, S.; Powell, C. NIST X-ray Photoelectron Spectroscopy Database https://srdata.nist.gov/xps/Default.aspx (accessed Jan 1, 2017).

(43) Lio, A. EUV Photoresists: A Progress Report and Future Prospects. *Synchrotron Radiat. News* **2019**, *32* (4), 9–14. https://doi.org/10.1080/08940886.2019.1634431.

(44) De Simone, D.; Vanelderen, P.; Vandenberghe, G. Photo Material Readiness at the Eve of EUVL HVM. *J. Photopolym. Sci. Technol.* **2017**, *30* (5), 613–617. https://doi.org/10.2494/photopolymer.30.613.

(45) Lugier, O.; Pokharel, U.; Castellanos, S. Impact of Synthetic Conditions on the Morphology and Crystallinity of FDMOF-1(Cu) Thin Films. *Cryst. Growth Des.* **2020**, *20* (8), 5302–5309. https://doi.org/10.1021/acs.cgd.0c00529.

Chapter 5

Effect of the Linkers' Functionalization on the Synthesis of SURMOFs from the DMOF-1(Cu) Family*

Abstract

Metal-organic frameworks (MOFs) have received a great amount of attention for their numerous properties that material scientists are trying to exploit in various applications ranging from catalysis to electronics. However, the synthesis of surface-mounted metal-organic frameworks, created to enable the integration of MOFs into devices, and the effect of synthesis conditions on their properties remain vaguely understood and hinder the development of MOF-containing devices. In this study, we synthesize five $[M_2L_2P]$ type SURMOFs of the DMOF-1(Cu) family with different functional groups attached to their dicarboxylate linkers using identical growth conditions to investigate the effect of the linker's nature on the properties of MOFs' thin films. Scanning electron microscopy, x-ray diffraction and infrared reflection absorption spectroscopy show significant differences in crystallinity and topography between materials. Yet, the level of influence that each synthesis parameters have over the properties of the SURMOFs remain elusive. The comparison these results with other studies on the growth of SURMOFs provides perspective on the matter and emphasize the need for the development of growth models that take into account all interactions among the functionalized surfaces and the MOF precursor locally and at the molecular level to solve the challenges of SURMOF synthesis.

* Lugier, O.; Amairi, M.N.; Castellanos, S.; "Effect of the linkers' functionalization on the synthesis of SURMOFs from the DMOF-1(Cu) family"; manuscript in preparation.

5.1 Introduction

Metal-organic frameworks (MOFs) are organic-inorganic crystalline materials first discovered in the late 1990s.[1] They are composed of inorganic clusters, commonly metal oxo clusters, linked to each other by organic ligands, also called linkers, forming 1D, 2D or, usually, 3D structures. The prototypical MOF is crystalline with an astonishing porosity that provides a very high surface to volume ratio.

MOFs have quickly gained steam in the scientific and industrial communities alike because of their great potential for structural and chemical tuning. Their tunability can be used to optimize the material for its intended application by adjusting key features, *e.g.*, conductivity,[2,3] fluorescence[4] or catalytic potential,[5,6] without major impact on its general structural properties. For these reasons, these materials captured the interest of material scientists as evidenced by the more than 90,000 synthesized MOF structures and 500,000 modeled ones in the last 30 years.[7]

Yet, MOFs' device integration remains a challenge as these materials are mostly synthesized in the form of crystalline powders or monocrystals. Even though, the development of surface-mounted metal-organic frameworks (SURMOFs) partially solved this issue, progress is required to better understand and control the mechanisms governing their synthesis.[8,9]

SURMOFs are nanometer- to micrometer-thick thin films of MOFs grown directly attached to the surface of a substrate. Their anchoring is often attained by covalent bonding through a Self-Assembled Monolayer (SAM). SAMs are composed of individual molecules bearing a functional group with high affinity for the substrate, usually located at one end of the molecule. When the adequate substrate is brought in contact with SAM molecules in favorable conditions, they self-assemble to form a continuous monolayer with well-defined packing and long-range order. The functional group located at surface of the SAM acts as a nucleation point for SURMOF crystals. The two main SAM species are thiols and silanes, functionalizing coinage metals and hydroxylated surfaces, respectively.[10,11]

Liquid phase epitaxy (LPE) is the main method used to grow SURMOFs. LPE enables a relatively accurate control over the thickness, coverage, homogeneity and even crystalline orientations of the thin films. Most SURMOFs are synthesized via layer-by-layer (LBL) methods using LPE technics as they proved the most efficient for a controlled growth.[12,13]

To complicate matters, experimental growth studies have shown that synthetic parameters are not easily transferable from SURMOF to SURMOF, even for specimens of the same MOF-family. This means that tedious experimental screenings are often needed to synthesize an optimized SURMOF for its intended application. Moreover, help from growth models is

limited as only few simulations and theoretical studies have been conducted on these materials, although the field is rapidly developing.[14,15]

For most applications, MOFs thin films have requirements regarding their coverage, thickness and crystallinity for optimum performance. The crystallinity comprises two parameters, the crystalline quality and the crystalline orientation. The former describes the size and purity of the crystalline domains and the latter their orientation relative to the surface of the substrate. Crystalline orientation requires consideration in certain applications for MOFs with anisotropic unit cells. This is because the nature and dimensions of the channels and pores accessible at the surface of such a SURMOF are different depending on its growth orientation in relation to the substrate's surface. Therefore, the diffusion of selected guests (molecules, ions, polymers, *etc.*) inside such material is regulated by the SURMOF's crystal orientation through size or chemical selectivity. Examples of applications where this property is critical include membranes, gas storage/separation, sensors, in-pore polymerization, dipoles modulation, and enantiomer separation, among others.[16–20]

DMOF-1(Cu), or [Cu(bdc)(dabco)$_{0.5}$] (bdc = 1,4-benzenedicarboxylate, dabco = 1,4-diazabicyclo[2.2.2]octane), is one of the simplest system of pillar-layer-based MOFs with the following formula [M_2L_2P] (M: Cu, Zn, Co, Ni; L: dicarboxylate linker; P: dinitrogen linker).[21] They form 2D sheets of four dicarboxylate linkers binding the metal dimers at their equatorial coordination sites while the dinitrogen linkers act as "pillars" that coordinate the apical coordination sites, effectively bonding neighboring 2D sheets (Fig. 5.1 and Fig. 5.4). One of the advantages of DMOF-1, and many [M_2L_2P] species comes from their tuneability. For instance, in DMOF-1, the aromatic ring of the bdc linker is relatively easy to functionalize enabling the inclusion of selected functional groups in the material and the fine-tuning of some properties of the material.[22]

Here, we investigate the influence of the functional group of the dicarboxylate linker on the crystalline orientation of five X-DMOF-1(Cu) thin films. The homogeneity of the coverage was also considered, although the limited number of growth cycles used during the layer-by-layer LPE synthesis led to low amounts of material deposited and a greater inhomogeneity. The dicarboxylate linkers tested are 1,4-benzenedicarboxylate, 2-nitroterephthalate (NO_2), 2-fluoroterephthalate (F), 2-bromoterephthalate (Br) and tetrafluoroterephthalate (F_4). They form DMOF-1(Cu), NO_2-DMOF-1(Cu), F-DMOF-1(Cu), Br-DMOF-1(Cu) and F_4-DMOF-1(Cu), respectively.

Each SURMOF was grown on a carboxyl-terminated and a pyridyl-terminated SAM of thiols, namely 4-mercaptomethyl benzoic acid (MBA) and 4-pyridylethyl mercaptan (4pyr), respectively. Surface coverage and topography were characterized by scanning electron microscopy (SEM) and atomic fore microscopy (AFM) while crystalline orientation and

quality were assessed with powder x-ray diffraction (PXRD). Infrared reflection absorption spectroscopy (IRRAS) provided additional information on the chemical compositions and crystalline orientation of the SURMOFs.

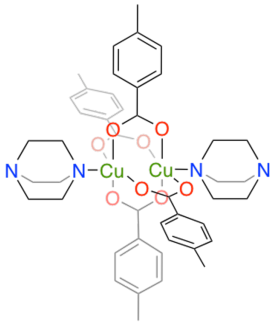

Figure 5.1: Chemical structure of one node in DMOF-1(Cu). Hydrogen atoms omitted for clarity.

5.2 Experimental

5.2.1 Sample preparation

Substrate preparation

1 × 1 cm^2 silicon substrates were sputter coated with a Leica EM ACE600 with a 5 nm- or 10 nm-thick chromium adhesion layer, then with a gold layer of 40 nm to 100 nm. The samples were then functionalized with Self-Assembled Monolayers of thiols, either 4-pyridylethyl mercaptan (4pyr) or 4-mercaptomethyl benzoic acid (MBA), by immersion in a 2 mM ethanol solution of the chosen thiol for 24 hours. A few drops of hydrochloric acid were added to the MBA solution to lower its pH to approx. 3.
Prior to the functionalization, all samples were cleaned using common UV-ozone procedure (30 min).

SURMOF growth

The SURMOFs were synthesized using the Liquid Phase Epitaxy (LPE) method[23] with ethanol solutions of the reagents. A growth cycle consists of 15 minutes of immersion in a copper acetate hexahydrate solution (1 mM), 4 minutes of rinsing in pure ethanol, 30 minutes of immersion in an equimolar solution of DABCO and the dicarboxylate linker (0.2 mM), 4 minutes of rinsing in pure ethanol.
A total of 20 cycles were used for each sample. The solutions were heated up to 50 °C with sonication (80 Hz) during the rising step.

Automatized LPE

A home-made automatized system with control over the temperature, time of immersion, stirring and sonication was used to ensure a reproducible synthesis of the samples.

5.2.2 Sample analysis

Powder X-Ray Diffraction (PXRD)

The crystalline phase purity and crystalline orientation of the SURMOFs were identified by Powder X-ray Diffraction. The measurements were conducted on a Bruker PXRD at room temperature, using Cu−Kα radiations, at angles in the range of $2\theta = 7-35°$, at a step of 0.02°, with accumulation time 0.15 s per step.

Atomic Force Microscopy (AFM)

AFM images were acquired in contact mode in air on a Bruker Scan Assist AFM using the silicon nitride Burker ScanAsyst-Air tips. The measured data were treated with the software Nanoscope Analysis version 2.0.

Scanning Electron Microscopy (SEM)

SEM images were taken using a FEI VERIOS 460 scanning electron microscope allowing for the investigation of the SURMOFs' surface topologies. The pictures were taken with 5 keV electrons at a beam current on 100 pA.

Infrared Reflection Absorption Spectroscopy (IRRAS)

IRRA spectra were taken using the Bruker A513/Q variable angle reflection accessory on a FT-IR spectrometer Bruker Vertex 80v at an angle of 70° (more grazing angle could not be used due to limitations in the set up and the dimension of the samples) with a resolution of 8 cm^{-1}. The incident light was not polarized.

5.3 Results

To simplify the discussion, code names are used to distinguish between SURMOFs grown on MBA from those grown on 4pyr. A thin film of F-DMOF-1(Cu) grown on 4-pyridylethyl mercaptan (4pyr) is written as F-4pyr and a thin film of NO_2-DMOF-1(Cu) grown on MBA is written as NO_2-MBA. The full name, X-DMOF-1(Cu), is used when describing the material regardless of the type of substrate functionalization. Finally, to avoid confusion, samples of DMOF-1(Cu) are written as H-DMOF-1(Cu).

5.3.1 Layer coverage and morphology (SEM)

SEM analysis (Fig. 5.2 and Fig. S5.1 in Supporting Information) shows that, regardless the functionalization of the linker, some material is always deposited on the substrate. However, the extent of the surface coverage significantly differs with the type of linker. Films of H-DMOF-1(Cu) and F-DMOF-1(Cu) are composed of tightly packed, intergrown nanocrystals providing a continuous coverage of the substrate while NO_2-DMOF-1(Cu), Br-DMOF-1(Cu) and F_4-DMOF-1(Cu) show well-defined µm-scale crystallites randomly dispersed over the surface often forming clusters.

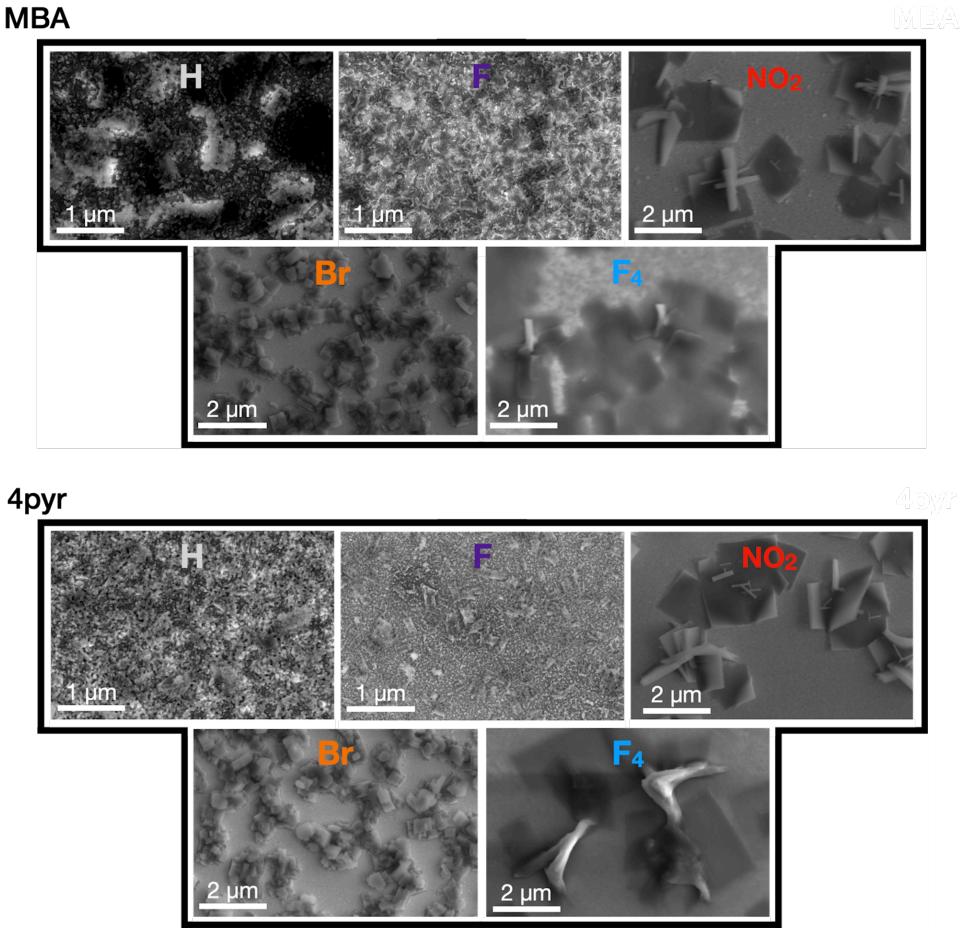

Figure 5.2: SEM micrographs of each SURMOF sample grown on MBA-functionalized (top) and 4pyr-functionalized Au substrates.

The SURMOFs composed of the big crystals can be divided into two groups. On one hand, Br-DMOF-1(Cu) displaying uniform cubic crystals and, on the other hand, NO_2- and F_4-DMOF-1(Cu) composed of distinctive plate-shaped crystals. On the SEM micrographs these plate-shaped crystals either appear as dark tiles lying flat on the surface or as bright tiles tilted upright.

5.3.2 Crystalline orientation (PXRD)

As explained in the introduction, DMOF-1 is composed of two distinct linkers and an anisotropic crystalline lattice with two distinct crystalline directions. This means that the crystals and thin films of the MOF that form on a substrate can have one of two possible crystalline orientations relative to the substrate (Fig. 5.4a). The [001] orientation (dabco in the plane perpendicular to the surface) and the [100] orientation (dabco in the plane parallel to the surface). Therefore, DMOF-1 has two main diffraction peaks observed in PXRD, one at $2\theta = 8.4°$ corresponding to the [100] orientation, and the other at $2\theta = 9.1°$ corresponding to the [001] orientation (Fig. 5.3). The shorter distance between parallel crystalline planes in the [001] orientation ($L_{dabco} < L_{bdc}$) yields a bigger 2θ angle. In addition, the surface pores of a [001]-oriented film of DMOF-1, formed by the four terephthalate linkers, and those of a [100]-oriented film, formed by two terephthalates and two dabco linkers, have diameters of ~0.7 nm and ~0.4 nm, respectively.[24–26]

All five X-DMOF-1(Cu) specimens studied here are expected to share comparable crystalline lattices, and thus similar 2θ values. H-MBA is predominantly [100]-oriented with a relatively small contribution of [001]-oriented domains while the exact opposite is observed for H-4pyr. In the selected growth conditions, H-DMOF-1(Cu) follows the trend expected by the templating effect of each of the SAMs (see discussion for more details). However, the results obtained for the other X-DMOF-1(Cu) specimens are not as consistent. The films of NO2-, F- and Br-DMOF-1(Cu) display crystalline orientations that are independent from the type of functionalization. NO_2-DMOF-1(Cu) remains mainly [001]-oriented with a sizeable amount of [100]-oriented domains, as evidenced by the relatively intense diffraction peak detected at 9.3°. F-DMOF-1(Cu) shows a unique diffraction peak at $2\theta = 8.7°$, although a second peak seems to appears above the noise level at $2\theta = 9.3°$ for F-4pyr. Br-DMOF-1(Cu) displays two almost identical peaks, suggesting an equal concentration of [100]-oriented and [001]-oriented domains. For unclear reasons, NO_2- and Br-DMOF-1(Cu) have stronger [200] diffraction peaks ($2\theta = 16.5°$) than [002] diffraction peaks ($2\theta = 18.6°$). F_4-MBA grows in the [001] direction with traces of [100]-oriented crystallites while a third unassigned diffraction peak is detected at $2\theta = 10.2°$. F_4-4pyr also is mainly [001]-oriented, but the concentration of the unidentified domains increases significantly while no [100]-oriented domains are detected. We speculate that the unassigned peak might be caused by catenation

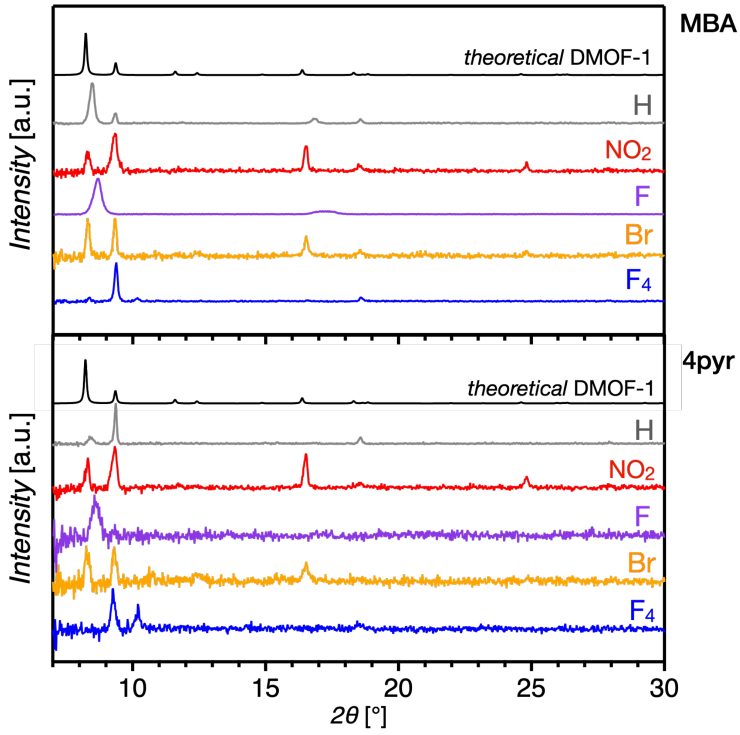

Figure 5.3: Normalized PXRD diffractograms. Each specimen is described by the code name of its linker. Theoretical H is the diffractogram of the theoretical crystalline lattice of DMOF-1(Cu).

(interpenetration or interweaving of MOF frameworks),[27] although the investigation of this phenomenon was out of the scope of these experiments.

Overall, we observe a significant decrease in signal to noise for the diffractograms of SURMOFs grown on pyridyl-functionalized substrates. A similar observation was made in our previous study on the growth of thin films of F-DMOF-1(Cu) where it was suggested that the SURMOFs grows slower (thinner) or with smaller crystalline domains on pyridyl-terminated thiols, based on complementary AFM analysis and previous reports.[28,29]

Slight shifts are observed for some diffraction peaks. They can be caused by slight discrepancies in measurement conditions (sample height) or by differences in the interplanar distances between materials. Interactions between linkers, metal centers and other moieties potentially present in the pores are also known to distort the angles of the unit-cell in metal-organic frameworks.[30,31] The widening of the diffraction peaks stems from the convolution of the instrumental profile and sample-related contributions like an inhomogeneous

distribution of the crystallite sizes or the presence of defects such as stacking faults and microstrains.[32,33]

5.3.3 Spectroscopic analysis (IRRAS)

Infrared Reflection Absorption Spectroscopy (IRRAS) was performed on the samples. In this technique, the electric field vector of the infrared radiation perpendicular to the surface of the substrate is enhanced.[34] This means that, for the molecules close to the surface, the detection of IR modes with dipole transition moments perpendicular to the Au-coated substrate is increased. Inversely, the modes with dipole transition moments parallel to the substrate's surface are strongly attenuated, or suppressed. Consequently, IRRAS can provide information on the crystalline orientation of the SURMOFs, in addition to the chemical information typically obtained from IR measurements.[30]

As described in other studies (chapter 6)[28], for a [001]-oriented X-DMOF-1(Cu), the symmetric vibration dipole moments of the COO groups are parallel to the surface, yielding attenuated ν_sCOO bands, while their asymmetric counterparts are perpendicular to the surface, yielding amplified ν_{as}COO bands. This effect is also seen for other bands such as the ν_{as}C=C or the fingerprint of the terephthalate linker as well as other material-specific bands. The effect of the crystalline orientations over ν_{as}COO, ν_sCOO and the aromatic C-H bending modes, δC-H at ~750 cm^{-1}, for the ideal X-DMOF-1(Cu) are listed in Table 1. The crystalline structure of X-DMOF-1(Cu) is displayed in Figure 5.4b.

A first look at the IRRAS data reveals notable shifts in wavenumbers between the spectra of SURMOFs featuring different functional groups. Each functional group has a unique influence over the bond vibrations of the aromatic ring and carboxylates. Their electron withdrawing or donating effects weakens or strengthens the metal-linker bond, respectively. A copper-carboxylate bond that is weakened by an electron withdrawing group, like NO_2, yields red-shifted COO vibrational bands, as seen Figure 5.4b. Moreover, we speculate that differences in crystalline structures and in-phase or out-of-phase vibrations of the extended crystalline lattice of each type of DMOF-1(Cu) can have and additional effect on the IR frequencies.[35]

The influence of the type of functionalization on each type of DMOF-1(Cu) was investigated by comparing the spectra of their thin films on MBA and 4pyr. For H-DMOF-1(Cu), we observe notable differences in the intensity of the absorption bands of their ν_{as}COO for both free carboxylic acids and Cu-bonded carboxylates at 1700 cm^{-1} and 1630 cm^{-1}, respectively. The relative intensity of the ν_sCOO mode at 1436 cm^{-1}, the 19a absorption band (a mix of ν_{as}C=C and νC-H from the aromatic ring)[36] at 1585 cm^{-1} and the fingerprint region of the terephthalate between 700 cm^{-1} and 850 cm^{-1} are all influenced by the SAM.

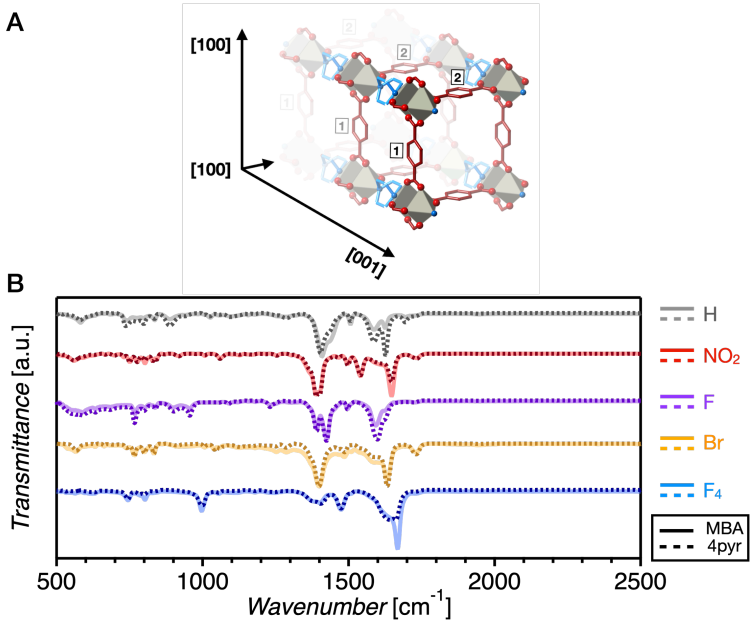

Figure 5.4: (A) 3D representation of DMOF-1(Cu) with the DABCO linker in blue and the two terephthalate linkers in red and labelled (1) and (2) to distinguish the contribution of their symmetric and asymmetric COO stretching vibrations in IRRAS (see Table 5.1). Hydrogen atoms omitted for clarity. **(B)** IRRAS spectra of the X-DMOF-1(Cu) taken at an angle of incidence of 70° using non-polarized light.

Table 5.1: *Comparison of the orientation relative to the substrate's surface of the transition dipole moments of the terephthalate linkers of X-DMOF-1(Cu).*

	BDC-(1)			BDC-(2)		
	ν_{as}(COO)	ν_{s}(COO)	δC-H	ν_{as}(COO)	ν_{s}(COO)	δC-H
[100]	∥	⊥	∥*	∥	∥	⊥*
[001]	⊥	∥	⊥*	⊥	∥	⊥*

Transition dipole moments that are close and parallel to the surface (∥) are attenuated while those perpendicular (⊥) to it are enhanced.
** the aromatic rings flip 180° along their C_2 axis.*

As shown in Table 5.1, the differences in the terephthalate fingerprint arise from the orientation of the terephthalate linkers relative to the surface. In a purely [100]-oriented film, 50% of the terephthalates are located in planes parallel to the surface against 100% in a purely [001]-oriented film. This means that, although the rings are flipping alongside the C_2 axis of the molecule,[37] the number of transition dipole moment potentially aligned with the surface normal differs depending on the orientation. Hence the discrepancies in the intensities of the bands associated to the aromatic rings.

NO_2-MBA and NO_2-4pyr are almost identical with a slight attenuation of ν_{as}COO at 1650 cm^{-1} for NO_2-4pyr. This was expected as PXRD showed a higher concentration of [100]-oriented domains in NO_2-4pyr than in NO_2-MBA. Exclusive to NO_2-DMOF-1(Cu), the NO_2 stretching vibration modes are observed at 1540 cm^{-1} and at 1350 cm^{-1} (shoulder). As mentioned before, the strongly electron withdrawing nitro group is responsible for weakening the metal-ligand bond strength resulting in the blue-shift of the ν_{as}COO of NO_2-DMOF-1(Cu) compared to H-DMOF. A similar effect is observed for F_4-DMOF-1(Cu).

For F-DMOF-1(Cu), the asymmetric COO stretching and asymmetric C=C stretching modes at 1627 cm^{-1} and 1595 cm^{-1}, respectively, appear less intense in F-MBA than in F-4pyr suggesting that F-4pyr has a higher concentration of [001]-oriented domains, relatively to F-MBA. This observation echoes with the weak diffraction peak detected above the noise level at $2\theta = 9.4°$ on the diffractogram of F-4pyr (Fig. 5.3).

For Br-DMOF-1(Cu), the IRRAS spectra are identical besides small baseline discrepancies. Again, these results were expected based on their diffractograms showing identical crystalline orientation regardless of the type of functionalization.

The main difference between the spectra of F4-MBA and F_4-4pyr is the significantly higher intensity of ν_{as}COO at 1670 cm^{-1} for F_4-MBA due to differences in their orientations. Minor differences are also observed in the terephthalate fingerprints, most likely stemming from the unassigned crystalline domains of F_4-4pyr that yielded a diffraction peak at $2\theta = 10.2°$.

The band at 1000 cm^{-1}, also detected for F-DMOF-1(Cu) at slightly lower wavenumbers, is assigned to the stretching vibration mode of C-F.

The weak bands detected at 1730 cm^{-1} for NO_2-DMOF-1(Cu), Br-DMOF-1(Cu) and F_4-DMOF-1(Cu), and at 1700 cm^{-1} for DMOF-1(Cu), indicate that non-bonded carboxylate groups are present in the structure from incomplete synthesis and structural defect in the material. In each pair, except for DMOF-1(Cu), the amount of free acid seems to be independent of the type of functionalization.

5.4 Discussion

SEM micrographs confirmed that the layer-by-layer LPE growth conditions tested in this study successfully deposit material regardless of the synthesized DMOF-1(Cu) derivative, although homogeneous coverage could only be obtained for H-DMOF-1(Cu) and F-DMOF-

1(Cu). The growth of other X-DMOF-1(Cu) analogues yielded agglomerated µm-scale crystallites scattered on the surface.

PXRD and IRRAS analysis, showed that the type of surface functionalization has little influence on the shapes, numbers and primary crystalline growth direction of the SURMOFs. Only the thin films of H-DMOF-1(Cu), F_4-DMOF-1(Cu) and, to a lesser extent, F-DMOF-1(Cu) grew differently on carboxyl-terminated thiols and pyridyl-terminated thiols.

On the other hand, the functional group attached to the terephthalate proved strongly influential to both the surface coverage and the crystalline orientation of the films. While the surface coverage, usually attributed to different nucleation rates or growth rates, is expected to improve with the addition of growth cycles to our relatively short procedure, the lack of clear trend regarding the crystalline orientation of the films complicates the identification of its determining parameters. Nevertheless, comparing our results with hypotheses proposed in previous reports on SURMOF growth can provide some insights.

Table 5.2: *Summary of the measured coverage and crystalline properties of each X-DMOF-1(Cu) thin film synthesized in this study.*

MOF		Coverage	Crystal shape	Crystalline orientation *main (secondary)*
H	MBA	homogeneous	undistinguishable	100 (001)
	4pyr			001 (100)
NO_2	MBA	poor	tiles	001 (100)
	4pyr			
F	MBA	homogeneous	undistinguishable	100
	4pyr			100 (001*)
Br	MBA	poor	cubes	100 / 001
	4pyr			
F_4	MBA	poor	tiles	001 (100 / unassigned)
	4pyr			001 (unassigned)

**very weak diffraction peak*

Multiple studies identified the templating effect of the SAM as the dominant parameter for the crystalline growth direction of SURMOF. There, the authors postulate that the growth direction is given by the terminal groups of the SAM during the nucleation phase and solely depends on how the SAM molecules coordinate the metal-clusters.[21,38,39] Taking the growth of X-DMOF-1(Cu) as an example, the hypothesis states that the carboxyl-terminated thiols featuring the same coordination groups than dicarboxylate linkers would bind to the first

copper dimers at the equatorial position, thus commanding a growth towards the [100] crystalline direction to the entire system. Contrarily, pyridyl-terminated thiols would preferentially bind to the axial positions and promote the [001] orientation. However, the experimental results obtained in the conditions of our study refute this hypothesis.

Another report on the growth of X-DMOF-1(Cu) and X-DMOF-1(Zn) on pyridyl-terminated SAMs, proposed the pKa of the dicarboxylate linker as determining factor for the orientation of the films. Although the cause of this effect remains unclear, the authors showed that purely [001]-oriented films could only be obtained for materials which bdc linkers have a pKa value higher than 2.5.[40] Again, our results disagree with this hypothesis. Four of our samples are predominantly [001]-oriented, namely H-4pyr, NO_2-4pyr, F_4-4pyr and F_4-MBA. The pKa values of their respective dicarboxylate linkers are 3.5, 1.79 and 1.42. Moreover, F_4-MBA, the sample made out of the most acidic linker tested and a [001]-unfavorable thiols, displayed one of the purest [001] orientation of the batch.

A third hypothesis suggests that the minimization of surface energies and ripening (recrystallization) combine as determining factor for the crystalline orientation of [M_2L_2P] type SURMOFs.[41] The authors commented that as long as the energy provided to the system remains below the threshold for Ostwald ripening and recrystallization, the orientation of the film is determined by the phenomenon of surface energies minimization. Another study on thin films of DMOF-1(Cu) also reported on the major influence of temperature on the crystalline orientation [42]

The pKa and ripening hypotheses are likely to be related. Indeed, the growth of SURMOFs is a ligand-exchange equilibrium between the original ligands of the metal clusters and the new linkers which yields the thermodynamic product, *i.e.*, the MOF. Because the carboxylate-metal coordination bond weakens with decreasing pKa (increasing acidity), acidic linkers favor ripening and recrystallization. We observed a similar behavior in our samples. H-DMOF-1(Cu) and F-DMOF-1(Cu), the specimens with the less acidic linkers, form layers of packed nanocrystals as expected from a system with limited recrystallization. On the other hand, the SURMOFs comprising more acidic linkers exclusively display large µm-scale crystals as the less thermodynamically stable nanocrystals (high surface to volume ratio) were dissolved and redeposited during synthesis.

Regardless, neither of these hypotheses can be verified nor rejected with certainty because of slight differences in the synthetic conditions or type of SURMOF used in each study. For instance, experiments in which the templating effect of the SAM was shown to govern the orientation of the SURMOF were mostly conducted on HKUST-1(Cu). The authors of the surface energy minimization hypothesis suggested that the templating effect has a relatively

greater importance for materials with an isotropic unit cell, such as HKUST-1(Cu). They argued that there is less energy to be gained from reorientation for such crystals.[41]

The hypothesis combining temperature and metal-linker bond strength appears to be the most probable due to the known relationship between these parameters and crystal growth rates or recrystallization. Moreover, the influence of surface energy minimization is a common notion in the field of crystal growth. Nevertheless, its influence appears constrained to $[M_2L_2P]$ type SURMOFs.

Finally, it is important to remark that the aforementioned studies, as well as ours, overlooked synthetic parameters known to affect SURMOF growth (*e.g.*, water concentration in reagent solutions, length of the SAM molecules)[43,44] as well as other behavioral phenomena observed in bulk MOFs that could also influence films of these materials (*e.g.*, catenation, swealing/breathing, flexibility).[27,45,46]

Although our observations and comparisons do not provide a definitive answer, they highlight that many of the variables surrounding the growth of SURMOFs can be intercorrelated. This interdependency observed between the synthesis parameters complicates the assessment of their precise nature and influence, and emphasize the need for extensive experimental screenings and the development growth models. For as mentioned earlier, the successful device integration of the promising materials that are metal-organic frameworks remains limited by the effectiveness of the available growth methods.

5.5 Conclusions

In this work, we investigated how the functional group of the terephthalate linkers impacts the crystalline orientation and coverage of copper-based SURMOFs of the DMOF-1(Cu) family, or $Cu(bdc)(dabco)_{0.5}$ where bdc = 1,4-benzenedicarboxylate and dabco = 1,4-diazabicyclo[2.2.2]octane, using identical liquid phase epitaxy (LPE) layer-by-layer (LBL) growth conditions. Each SURMOF was grown on a pyridyl-functionalised Au-substrate and a carboxyl-functionalized Au-substrate. The following functional groups were tested: NO_2, F, Br and tetrafluoro (F_4).

We show that, for our set of synthesis conditions, the SAM has little influence over the SURMOFs' properties as opposed to the nature of the dicarboxylate linkers. We observe a correlation between the sizes of the crystallites and the pKa of the linkers. Homogeneous layers of tightly packed nanocrystals could only be obtained using the less acidic linkers. The parameters controlling the crystalline orientation of the SURMOFs are more complicated to identify with precision. Nevertheless, the relationship between linker's pKa and crystallite's properties suggests that crystalline orientation and acidity could be related.

Comparing the hypotheses proposed in previous studies on the growth of SURMOF to the results obtained here provided some perspective. Yet, no clear answer could be provided besides that the properties of the films depend on a blend of synthetic conditions which influence seemingly varies depending on the general conditions of the synthesis and the type of MOF. Theoretical calculations could help to precisely describe the mechanisms defining the growth of these materials.

With this work we emphasize the need for extensive experimental screening of SURMOF synthesis and for the development of growth models to unlock the full potential of these promising materials.

Bibliography

1. Li, H., Addaoudi, M., O'Keeffe, M. & Yaghi, O. M. Design and synthesis of an exceptionally stable and highly porous metal-organic framework. *Nature* **402**, 276–279 (1999).
2. Talin, A. A. *et al.* Tunable electrical conductivity in metal-organic framework thin-film devices. *Science.* **343**, 66–69 (2014).
3. Bhardwaj, S. K. *et al.* An overview of different strategies to introduce conductivity in metal-organic frameworks and miscellaneous applications thereof. *J. Mater. Chem. A* **6**, 14992–15009 (2018).
4. Cornelio, J., Zhou, T.-Y., Alkaş, A. & Telfer, S. G. Systematic Tuning of the Luminescence Output of Multicomponent Metal–Organic Frameworks. *J. Am. Chem. Soc.* **140**, 15470–15476 (2018).
5. Cirujano, F. G. & Llabrés i Xamena, F. X. Tuning the Catalytic Properties of UiO-66 Metal–Organic Frameworks: From Lewis to Defect-Induced Brønsted Acidity. *J. Phys. Chem. Lett.* **11**, 4879–4890 (2020).
6. Song, F., Wang, C., Falkowski, J. M., Ma, L. & Lin, W. Isoreticular Chiral Metal−Organic Frameworks for Asymmetric Alkene Epoxidation: Tuning Catalytic Activity by Controlling Framework Catenation and Varying Open Channel Sizes. *J. Am. Chem. Soc.* **132**, 15390–15398 (2010).
7. Moosavi, S. M. *et al.* Understanding the diversity of the metal-organic framework ecosystem. *Nat. Commun.* **11**, 1–10 (2020).
8. Gliemann, H. & Wöll, C. Epitaxially grown metal-organic frameworks. *Mater. Today* **15**, 110–116 (2012).
9. Frameworks for commercial success. *Nat. Chem.* **8**, 987–987 (2016).
10. Ulman, A. Formation and structure of self-assembled monolayers. *Chem. Rev.* **96**, 1533–1554 (1996).
11. Gooding, J. J., Mearns, F., Yang, W. & Liu, J. Self-assembled monolayers into the 21st century: Recent advances and applications. *Electroanalysis* **15**, 81–96 (2003).
12. Heinke, L., Gliemann, H., Tremouilhac, P. & Wöll, C. SURMOFs: Liquid-Phase Epitaxy of Metal-Organic Frameworks on Surfaces. in *The Chemistry of Metal-Organic Frameworks: Synthesis, Characterization, and Applications* 523–550 (Wiley-VCH Verlag GmbH & Co. KGaA, 2016). doi:10.1002/9783527693078.ch17.
13. Zhuang, J. L., Terfort, A. & Wöll, C. Formation of oriented and patterned films of metal-organic frameworks by liquid phase epitaxy: A review. *Coord. Chem. Rev.* **307**, 391–424 (2016).
14. Hill, A. R. *et al.* CrystalGrower : a generic computer program for Monte Carlo modelling of crystal growth . *Chem. Sci.* (2021) doi:10.1039/d0sc05017b.

15. Keskin, S. & Altinkaya, S. A. A review on computational modeling tools for MOF-based mixed matrix membranes. *Computation* **7**, (2019).
16. Ohhashi, T., Tsuruoka, T., Fujimoto, S., Takashima, Y. & Akamatsu, K. Controlling the Orientation of Metal-Organic Framework Crystals by an Interfacial Growth Approach Using a Metal Ion-Doped Polymer Substrate. *Cryst. Growth Des.* **18**, 402–408 (2018).
17. Liu, B., Tu, M. & Fischer, R. A. Metal-organic framework thin films: Crystallite orientation dependent adsorption. *Angew. Chemie Int. Ed.* **52**, 3402–3405 (2013).
18. Huelsenbeck, L. *et al.* Modulating and orienting an anisotropic Zn-based metal organic framework for selective CH_4/CO_2 gas separation. *Crystals* **9**, 7–11 (2019).
19. Chen, S.-M., Liu, M., Gu, Z.-G., Fu, W.-Q. & Zhang, J. Chiral Chemistry of Homochiral Porous Thin Film with Different Growth Orientations. *ACS Appl. Mater. Interfaces* **8**, 27332–27338 (2016).
20. Chen, S. M., Liu, M., Gu, Z. G., Fu, W. Q. & Zhang, J. Chiral Chemistry of Homochiral Porous Thin Film with Different Growth Orientations. *ACS Appl. Mater. Interfaces* **8**, 27332–27338 (2016).
21. Shekhah, O. Layer-by-Layer Method for the Synthesis and Growth of Surface Mounted Metal-Organic Frameworks (SURMOFs). *Materials.* **3**, 1302–1315 (2010).
22. Noh, J. *et al.* Three Component Controls in Pillared Metal-Organic Frameworks for Catalytic Carbon Dioxide Fixation. *Catalysts* **8**, 565 (2018).
23. Ohnsorg, M. L., Beaudoin, C. K. & Anderson, M. E. Fundamentals of MOF Thin Film Growth via Liquid-Phase Epitaxy: Investigating the Initiation of Deposition and the Influence of Temperature. *Langmuir* **31**, 6114–6121 (2015).
24. Witherspoon, V. J., Xu, J. & Reimer, J. A. Solid-State NMR Investigations of Carbon Dioxide Gas in Metal-Organic Frameworks: Insights into Molecular Motion and Adsorptive Behavior. *Chem. Rev.* **118**, 10033–10048 (2018).
25. Seki, K. & Mori, W. Syntheses and characterization of microporous coordination polymers with open frameworks. *J. Phys. Chem. B* **106**, 1380–1385 (2002).
26. Dybtsev, D. N., Chun, H. & Kim, K. Rigid and flexible: A highly porous metal-organic framework with unusual guest-dependent dynamic behavior. *Angew. Chemie - Int. Ed.* **43**, 5033–5036 (2004).
27. Yaghi, O. M. A tale of two entanglements. *Nat. Mater.* **6**, 92–93 (2007).
28. Lugier, O., Pokharel, U. & Castellanos, S. Impact of Synthetic Conditions on the Morphology and Crystallinity of FDMOF-1(Cu) Thin Films. *Cryst. Growth Des.* **20**, 5302–5309 (2020).
29. Seoane, B., Castellanos, S., Dikhtiarenko, A., Kapteijn, F. & Gascon, J. Multi-scale crystal engineering of metal organic frameworks. *Coord. Chem. Rev.* **307**, 147–187 (2016).
30. Burrows, A. D. *et al.* Compositional control of pore geometry in multivariate metal–organic frameworks: an experimental and computational study. *Dalt. Trans.* **45**,

4316–4326 (2015).
31. Tan, K. *et al.* Water interactions in metal organic frameworks. *CrystEngComm* **17**, 247–260 (2015).
32. Patterson, A. L. The Scherrer Formula for X-Ray Particle Size Determination. *Phys. Rev.* **56**, 978–982 (1939).
33. Langford, J. I. & Wilson, A. J. C. Scherrer after sixty years: A survey and some new results in the determination of crystallite size. *J. Appl. Crystallogr.* **11**, 102–113 (1978).
34. Nishikawa, Y., Osawa, M., Ataka, K.-I. & Yoshii, K. Surface-Enhanced Infrared Spectroscopy: The Origin of the Absorption Enhancement and Band Selection Rule in the Infrared Spectra of Molecules Adsorbed on Fine Metal Particles. *Appl. Spectrosc.* **47**, 1497–1502 (1993).
35. Hermans, J. J. *et al.* 2D-IR spectroscopy for oil paint conservation: Elucidating the water-sensitive structure of zinc carboxylate clusters in ionomers. *Sci. Adv.* **5**, 1–10 (2019).
36. Tan, K. *et al.* Stability and hydrolyzation of metal organic frameworks with paddle-wheel SBUs upon hydration. *Chem. Mater.* **24**, 3153–3167 (2012).
37. Khudozhitkov, A. E., Kolokolov, D. I., Stepanov, A. G., Bolotov, V. A. & Dybtsev, D. N. Metal-Cation-Independent Dynamics of Phenylene Ring in Microporous MOFs: A 2H Solid-State NMR Study. *J. Phys. Chem. C* **119**, 28038–28045 (2015).
38. Biemmi, E., Scherb, C. & Bein, T. Oriented growth of the metal organic framework $Cu_3(BTC)_2(H_2O)_3 \cdot xH_2O$ tunable with functionalized self-assembled monolayers. *J. Am. Chem. Soc.* **129**, 8054–8055 (2007).
39. Vello, T. P., Strauss, M., Costa, C. A. R., Corrêa, C. C. & Bof Bufon, C. C. Deterministic control of surface mounted metal-organic framework growth orientation on metallic and insulating surfaces. *Phys. Chem. Chem. Phys.* **22**, 5839–5846 (2020).
40. Yu, X. J. *et al.* Liquid-Phase Epitaxial Growth of Highly Oriented and Multivariate Surface-Attached Metal-Organic Frameworks. *J. Am. Chem. Soc.* **141**, 18984–18993 (2019).
41. Yu, X. J., Zhuang, J. L., Scherr, J., Abu-Husein, T. & Terfort, A. Minimization of Surface Energies and Ripening Outcompete Template Effects in the Surface Growth of Metal–Organic Frameworks. *Angew. Chemie - Int. Ed.* **55**, 8348–8352 (2016).
42. Zhuang, J. L. *et al.* Insight into the Oriented Growth of Surface-Attached Metal-Organic Frameworks: Surface Functionality, Deposition Temperature, and First Layer Order. *J. Am. Chem. Soc.* **137**, 8237–8243 (2015).
43. Wang, Z., Rodewald, K., Medishetty, R., Rieger, B. & Fischer, R. A. Control of Water Content for Enhancing the Quality of Copper Paddle-Wheel-Based Metal-Organic Framework Thin Films Grown by Layer-by-Layer Liquid-Phase Epitaxy. *Cryst. Growth Des.* **18**, 7451–7459 (2018).

44. Müller, K. *et al.* Water as a modulator in the synthesis of surface-mounted metal-organic framework films of type HKUST-1. *Dalt. Trans.* **47**, 16474–16479 (2018).
45. Serre, C. *et al.* Role of solvent-host interactions that lead to very large swelling of hybrid frameworks. *Science (80).* **315**, 1828–1831 (2007).
46. Elsaidi, S. K., Mohamed, M. H., Banerjee, D. & Thallapally, P. K. Flexibility in Metal–Organic Frameworks: A fundamental understanding. *Coord. Chem. Rev.* **358**, 125–152 (2018).

Chapter 6

Impact of the synthetic conditions on the morphology and crystallinity of FDMOF-1(Cu) thin films*

Abstract

Metal-organic frameworks (MOFs) have attracted a lot of interest for their numerous properties. However they are usually obtained as a powder (bulk) or as single crystals, which complicates their implementation into devices that could further exploit these properties. The development of surface-mounted MOFs (SURMOFs), allowed to synthesize MOFs' thin films chemisorbed to a substrate, creating a viable solution to the device integration problem. Yet, the fundamental understanding of the mechanisms governing their growth remains limited and the systematic optimization of synthetic parameters is tedious. More studies on SURMOFs growth are needed before MOF-based devices become the norm. In this paper, a pillared-layer MOF with fluorinated terephthalate linkers, $Cu_2(fbdc)_2(dabco)$ or F-DMOF-1(Cu), was synthesized on functionalized gold surfaces using a layer-by-layer method of Liquid Phase Epitaxy (LPE). The effects of temperature, linker concentration, type of surface functionalization and sonication during the rinsing step on coverage, film morphology and crystal orientation were studied. We found that the concentration of the linker has a strong impact on the morphology of the crystallites formed as well as on the surface coverage. It was noticed that the crystalline orientation is not only governed by the functionalization of the substrate, supporting the hypothesis that SURMOF thin films can switch their crystalline orientation during growth. This study adds information on which variables affect the formation of the first layers of a prototypical SURMOF.

*Lugier, O.; Pokharel, U.; Castellanos, S. Impact of Synthetic Conditions on the Morphology and Crystallinity of FDMOF-1(Cu) Thin Films. Cryst. Growth Des. 2020, 20 (8), 5302–5309. https://doi.org/10.1021/acs.cgd.0c00529

6.1 Introduction

Metal-organic frameworks (MOFs) have been extensively investigated during the past few decades for their numerous properties that promise ground-breaking applications. MOFs can be conductive, fluorescent, luminescent or possess redox and/or catalytic sites in their channels and/or pores.[1,2] At the same time, the vast majority of them are porous, crystalline, and easily tunable. This opens the possibility of adjusting their macroscopic properties by means of modifying their composition and crystalline structure. This combination of features keeps the interest of the scientific community high, leading to a proliferation of MOF-related publications over the past thirty years since the report of the first specimens in the 1990's.[3,4]

Despite these advantages, MOFs have one main problem when it comes to device integration[5]; they are usually obtained in the form of bulk powder via hydro/solvo thermal synthesis.[6] Surface-mounted metal-organic frameworks (SURMOFs) were developed to solve this technical limitation.[7,8] SURMOFs are grown as thin films on substrates, usually via a liquid phase epitaxy (LPE) procedure.[9] Prior to the synthesis, the substrate's surface is modified with different functional groups, most commonly through the use of self-assembled monolayers (SAMs), such as the ones formed by thiols or silanes.[10] The modification of the substrate's surface is necessary in order to allow a strong bonding with the SURMOF via the coordination of the terminal group of the SAM with the metal clusters of the MOF at the interface. LPE is a general term that comprises a multitude of other sub-methods, the most common being the layer-by-layer (LBL) synthesis. LBL consists of the successive immersion of the functionalized substrates into a solution containing the precursors of the metallic nodes and a solution containing the organic linkers. Between each immersion in each building block solution, the samples are rinsed with pure solvent to remove uncoordinated scaffolds. When used with the right conditions, layer-by-layer synthesis leads to homogenous, highly oriented crystalline thin films of metal-organic frameworks and enables an accurate control over their thicknesses. Liquid Phase Epitaxy gives these materials the possibility to be incorporated and exploited in devices, as well as in various supports for other applications such as catalysis, and gas purification or separation.[10,11] MOFs still remain mainly produced in laboratory scale for fundamental studies but the development of SURMOF thin films started the transition from wet bench experiments to commercially available devices, like ION-X by NuMat or TruPick™ by MOF Technologies.[12,13]

Regardless of these devices and the impressive list of MOFs reported in the literature, there is relatively limited amount of theoretical and experimental understanding about their growth processes.[14] And this understanding is even more limited on surfaces which compels the optimization of synthesis procedures to be conducted through tedious systematic screenings.[15–20]

In this paper, we report the synthesis and first systematic study on the growth of Cu(2-fluorobenzene-1,4-dicarboxylic acid)(DABCO)$_{0.5}$ or F-DMOF-1(Cu) as thin films (< 100 nm). The interest of using the terephthalate linker with a single fluorine atom arises from the dipole moment that results from having the fluorine substituent in the benzene ring, while negligible steric hindrances are added compared to the non-functionalized terephthalate, given the small size of the fluorine atom. This characteristic can potentially enable the control of the dipole orientation in the framework with an external electric field.[21] Such control can have a significant impact on the material properties, such as for example enabling control of guest diffusion.[22] The DMOF crystalline lattice is particularly interesting for this purpose because, due to its pillared-layer structure, by choosing the right orientation of the crystal growth, the linkers that bear the dipoles can be contained in a plane parallel to the substrate. Because these linkers can rotate, the dipoles direction (up/down) can be controlled by applying an external electric field perpendicular to the substrate. Therefore, having a good control on the growth of such a SURMOF is of high relevance.

Therefore, we explored how the characteristics of the SURMOF (substrate coverage, morphology, and crystalline orientation) are affected by the substrate functionalization, growth temperature, concentration of the reagents, and use of sonication during the rinsing step of the LPE method. As a result of our investigations, the first highly oriented thin film of this fluorinated MOF was attained and some correlations between the layer morphology and reagent concentrations as well as between crystalline orientation and substrate functionalization were found.

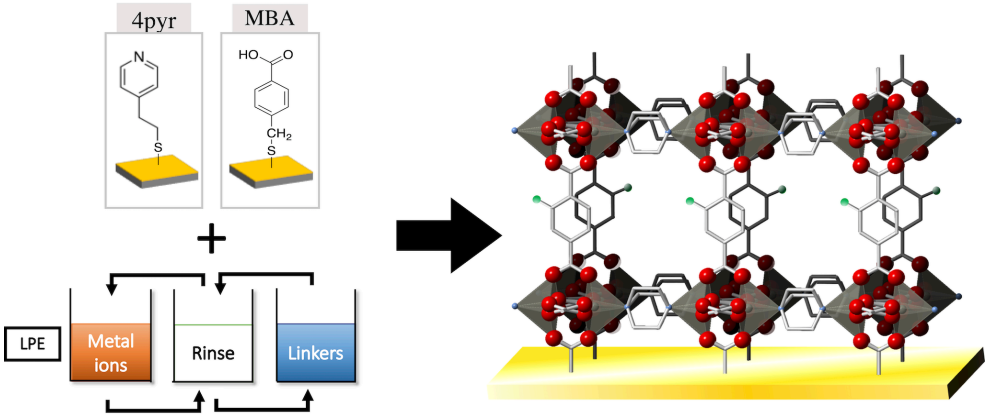

Figure 6.1: Schematic representation of the LBL growth method and the used variables and the observables with their corresponding characterization techniques.

6.2 Experimental

6.2.1 Sample preparation

Substrate preparation

1 × 1 cm^2 silicon substrates were sputter coated with a Leica EM ACE600 with a chromium adhesion layer 10 nm thick, then with a gold layer of 40 nm to 100 nm. The samples were then functionalized with Self-Assembled Monolayers (SAM) of thiols, either 4-pyridylethyl mercaptan (4pyr) or 4-mercaptomethyl benzoic acid (MBA), shown in Figure 6.1, by immersion in a 2 mM ethanol solution of the chosen thiol for 24 hours. A few drops of hydrochloric acid (HCl) were added to the MBA solution until the pH was approximately 3. Prior to the functionalization, all samples were cleaned using common UV-ozone procedur.

SURMOF growth

FDMOF-1(Cu) was synthesized using the Liquid Phase Epitaxy (LPE) method[23] employing ethanol solutions of the reagents. A cycle of growth consists in: 15 minutes of immersion in a copper acetate hexahydrate solution, $Cu(OAc)_2 \bullet 6H_2O$, followed by 3 minutes of rinsing in pure ethanol, followed by 30 minutes of immersion in an equimolar solution of 2-fluoroterephtalic acid (fbdc) and 1,4-diazabicyclo[2.2.2]octane (dabco), ended by 3 minutes of rinsing in pure ethanol. Samples underwent 20 cycles of growth. With all solutions in ethanol. A schematic representation of the procedure can be found in Figure 6.1.

The synthesis conditions varied for each sample. The solutions for the LPE were either heated up to 50 °C or remained at room temperature (~20 °C). The concentrations used were 2 mM for $Cu(OAc)_2 \bullet 6H_2O$, and equimolar 0.2 mM or 0.02 mM concentrations for the solutions containing the two organic ligands. The rinsing step was conducted either with or without sonication and for every batch the SURMOF was grown on substrates previously functionalized with 4-pyridylethyl mercaptan (4pyr) or with 4-mercaptomethyl benzoic acid (MBA). All possible combinations of these four variables (substrate functionalization, concentration, temperature, sonication during rinsing) were used to grow the F-DMOF(Cu) (Table 6.1).

Automatized LPE

The synthesis of the SURMOFs was conducted using a home-made automatized system with control over the temperature, time of immersion, stirring and sonication. The sample holder can accommodate up to 6 substrates at the same time allowing growth of multiple samples in identical conditions for direct comparison.

6.2.2 Sample analysis

Powder X-Ray Diffraction (PXRD)

The phase purity (crystallinity) and crystalline orientation of the SURMOFs were identified by Powder X-ray Diffraction. The measurements were conducted on a Bruker PXRD at room temperature, using Cu−Kα radiations, at angles in the range of 2θ = 7−33°, at a step of 0.02°, with accumulation time 0.15 s per step.

Atomic Force Microscopy (AFM)

AFM images were acquired in contact mode in air on a Bruker Scan Assist AFM using the silicon nitride Burker ScanAsyst-Air tips. The measured data were treated with the software Nanoscope Analysis version 2.0.

Scanning Electron Microscopy (SEM)

SEM images were taken using a FEI VERIOS 460 scanning electron microscope allowing for the investigation of the SURMOF's surface topologies. The pictures were taken with 5 keV electrons at a beam current on 100 pA.

Infrared Reflection Absorption Spectroscopy (IRRAS)

IRRA spectra were taken using the Bruker A513/Q variable angle reflection accessory on a FT-IR spectrometer Bruker Vertex 80v at an angle of 70° (more grazing angle could not be used due to limitations in the set up and the dimension of the samples) with a resolution of 8 cm^{-1}. Each spectrum is the result of an accumulation of 200 scans. The incident light was not polarized.

6.3 Results and discussion

Pillar-layer-based MOFs with the following formula $[M_2L_2P]$ (M: Cu, Zn, Co, Ni; L: dicarboxylate linker; P: dinitrogen linker) form 2D sheets composed of four dicarboxylate linkers binding to the metallic cation dimers at the equatorial coordination sites. These sheets are connected by the dinitrogen linkers coordinating the metal dimers at the apical coordination sites, acting as pillars (Fig. 6.4b and Fig. 5.1 in Chapter 5). Generally, 1,4-benzenedicarboxylate units (BDC), also known as terephthalate, play the role of the linkers in the 2D sheets while 1,4-diazabicyclo[2.2.2]octane (dabco) or 4,4'-bipyridine play the role of the pillars. A prototypical MOF with such structure that has been reported as SURMOF is $Cu_2(bdc)_2(dabco)$ or DMOF-1(Cu).[24]

Table 6.1: *List of synthetic conditions used for the preparation of the samples and reference for sample labels.*

Synthetic parameters	Values	Code
Linkers concentration	0.02 mM	c
	0.2 mM	C
*Sonication	yes	Y
	no	N
Temperature	20 °C	20
	50 °C	50
SAM	MBA	-M
	4pyr	-P

* *during the rinsing step.*

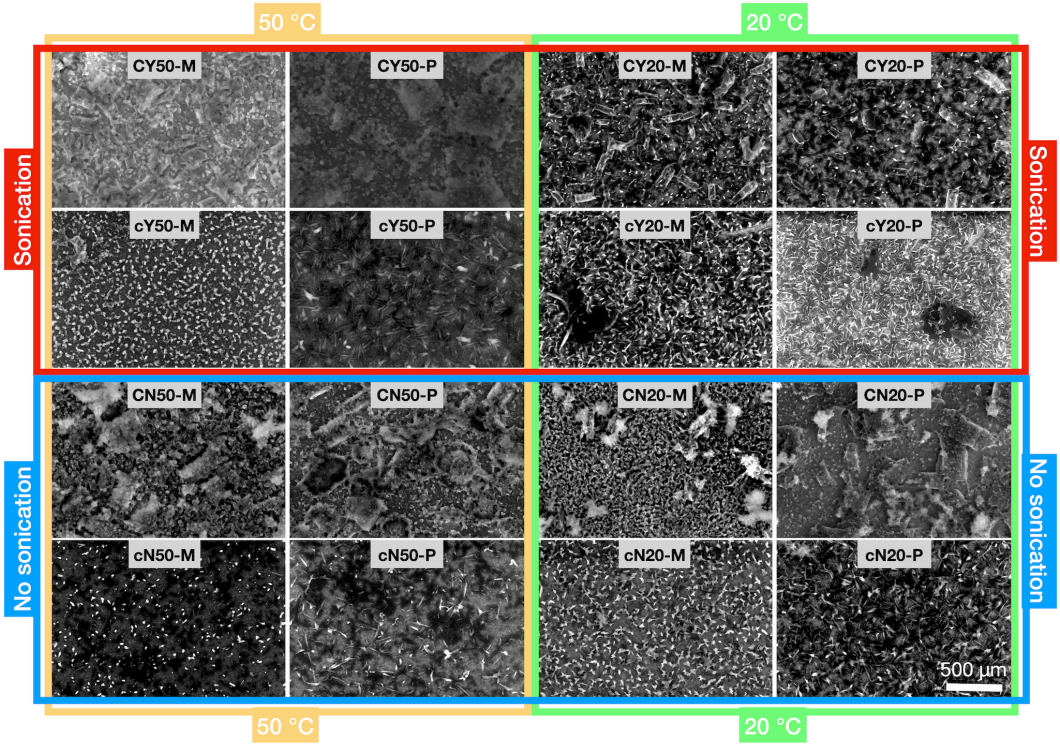

Figure 6.2: SEM pictures of the different FDMOF-1(Cu) samples.

F-DMOF-1(Cu) or $Cu_2(fbdc)_2(dabco)$ (where fbdc stands for 1,4-(2-fluorobenzene) dicarboxylate) is an analogous MOF where the terephthalate linker is replaced by a functionalized version of it, the 2-fluoroterephtalate (fbdc). When anchored on a substrate, the 2D sheets formed with fbdc can grow parallel (DABCO pillars perpendicular) or perpendicular (DABCO pillars parallel) to the substrate. It should be highlighted that, although many versions of tailored DMOF-1(Cu) or $Cu_2(bdc)_2(dabco)$ were reported, to the best of our knowledge the singly fluorinated version of the material has not been yet reported, neither as a bulk material nor as a SURMOF.

In general, for any potential application of a SURMOF, the thin film should be grown homogeneously over the whole functionalized area. Furthermore, for particular cases, such as for modulation of the dipoles orientation, proton/electron conductivity, gas detection, enantiomer separation/adsorption and others, it is necessary to have good control over the orientation of the SURMOF crystalline lattice. Therefore, the two main aspects studied in this work were the coverage of the SURMOF on the substrate and the SURMOF crystalline orientation.[25–28] The four variables tested were: the type of functionalization of the substrate, the temperature during immersion in the reagents solutions, the concentration of linkers in solution, and the use of sonication (or not) during the rinsing step. Temperature and concentration are expected to mainly influence the growth kinetics and thus to strongly affect the coating coverage (extension, continuity, and thickness) and the size of the crystalline domains forming the thin film. Likewise, the functionalization of the substrate is expected to mostly influence the orientation of the SURMOF. The effect of sonication during rinsing is harder to predict. Although it is mainly used to remove non-covalently bonded species, it is also known to induce the growth of MOFs through the creation of hot-spots that initiate crystal nucleation.[29,30] In addition, previous studies involving HKUST-1(Cu), have pointed out that sonication while rinsing has a positive influence over the properties of the thin film such as the surface roughness, overall morphology, optical properties and quality.[31] The list of variables used for SURMOF growth and the code used to label each sample are listed in Table 6.1.

The different samples resulting from the combination of these variables were evaluated by SEM, PXRD, and IRRAS. Specifically, coverage of the substrate and morphology of the crystallites were evaluated with SEM and AFM, the orientation of the crystalline lattice with PXRD and, indirectly, with IRRAS, and to some extent the chemical composition of the MOF with IRRAS.

6.3.1 Layer coverage and morphology

Essential requirements for device integration are the homogeneity and surface coverage of the SURMOF thin film. SEM analysis (Figure 6.2) shows that, regardless of the synthesis

conditions, there is always deposited material but the extent of the surface coverage differs. A first observation is that the low concentration of the linker has a detrimental effect on surface coverage when 50 °C are used for the synthesis. Yet, the crystallites population seems to increase at low concentration if sonication is applied. This might indicate that when sufficient energy is given to the system, the concentration of the linker is a limiting factor for the growth. In the case of sonication, additional energy is given in the form of hotspots that most likely create nucleation points where unwashed reagents still adsorbed at the surface (or trapped within the pores in later cycles) react. In fact, various ultrasound technics have proven to be an efficient method for the synthesis of MOFs.[29,31,32]

Further differences between samples can be found within the morphology of the crystallites observed on the surface. In general, for identical sets of temperature, surface functionalization, and rinsing conditions, a decrease in the concentration of the linkers solution has an important impact on the morphology of the crystallites. While samples prepared with a higher linkers' concentration yielded rectangular/square-shaped blocks with granular texture, samples prepared with low concentration yielded needle-shaped crystallites (Figure 6.2).

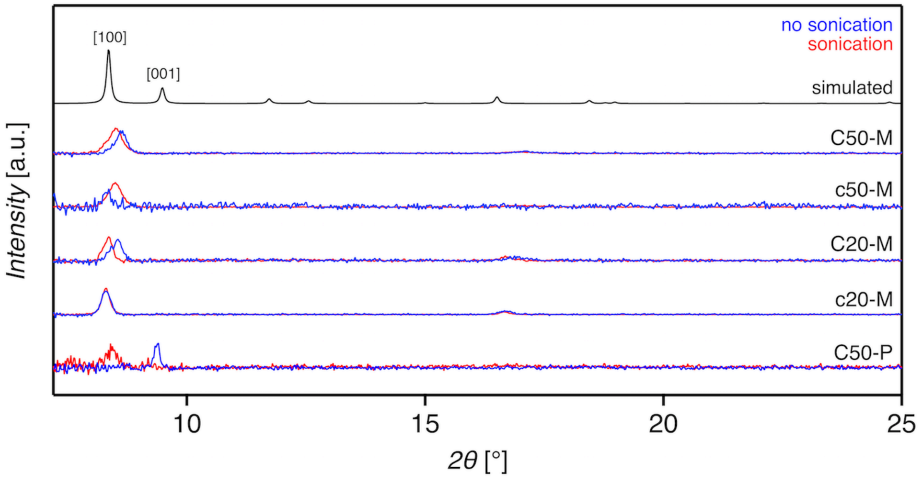

Figure 6.1: Normalized PXRD diffractograms of the FDMOF samples that show clear crystalline peaks. The diffractograms of samples sharing equivalent synthetic conditions in terms of concentration, temperature, and thiol species but that differ in the rinsing conditions are paired (without sonication blue, with sonication red). The simulated diffractogram of DMOF-1(Cu), a MOF with identical interplanar distances, is used as reference.

The impact of the temperature is more subtle. The thin films grown at lower temperature seemingly display poorer coverage. In particular for the samples that were sonicated there is a certain trend of lower amount of large structures when the growth is performed at 20 °C compared to the 50 °C samples. Finally, no clear difference in morphology and coverage can be attributed to the type of functionalization of the substrate.

Therefore, in these series, the best conditions to obtain thin films of FDMOF-1(Cu) in terms of coverage are higher temperature and higher concentration of linker, that is, the samples with code CY/N50. The nature of the surface-functionalizing-thiols seems to have little to no influence over the crystallite shape of this SURMOF.

On a side note, the thickness and roughness of the aforementioned samples (CY/N50-M/P) were respectively measured to be in the range of 70-90 nm and 30-35 nm, excepted for CN50-P displaying a thickness of 30 nm and a roughness of 35 nm as measured by AFM (see Table S6.2 and Figure S6.2). The differences in synthetic conditions, and associated differences in the kinetics of growth, explain the range of thicknesses obtained for the three thicker films. The significantly smaller thickness and higher roughness of CN50-P indicates that the sample is composed of a thin fragmented layer or a collection of big individual crystallites on a thin layer. We found a growth rate of 2.3 layer to 3 layers per cycle for the thick samples and 1.5 layers per cycle for CN50-P, although the latter needs to be considered with precaution due to the high roughness of the SURMOF layer. Based on its lattice parameters (a = c = 15.48 Å; b = 9.64 Å; $\alpha = \beta = \gamma = 90°$)[33,34], a pure epitaxial growth of FDMOF-1(Cu) should lead to an increase in thickness of about 1.6 nm per cycle or 0.96 nm per cycle, depending on its crystalline orientation.

Non-linear growth rate, inhomogeneous growth and the growth of more than one layer per cycle are phenomena that were reported for various SURMOFs, in particular during the early stage of the growth.[23,24,35]

6.3.2 Crystalline orientation

Having control over the crystalline orientation can be of critical importance in several potential SURMOFs applications. For DMOF, the different length of each type of linker (terephthalate and dabco, Figure 6.1 and 6.4b) makes the crystalline structure anisotropic. This means that, for a thin film, the channels that will be accessible from the surface of the SURMOF will be different depending on the crystalline orientation on the substrate. The dimension and nature of the accessible channel determine whether or not specific guests will diffuse in the pores. In some cases, these differences in the channel sizes of DMOFs could be used for selectivity in guest diffusion by controlling the crystalline orientation of the corresponding SURMOF. This argument would concern, for example, applications like gas

storage/separation, sensors, membranes, molecular transport/storage, proton/electron conduction, in-pore polymerization and others.[25–27]

The nature of the end group of the self-assembled monolayer on the substrate has proven to have a significant impact on the crystalline growth direction of multiple SURMOFs.[24,36] Metal clusters coordinate to the terminal functional group at the surface of the monolayer during the very first steps of the LPE. Therefore, the SAM usually acts as a molding template to control the orientation of the whole thin film.

For the pillared-layer SURMOFs of the DMOF family, a SAM featuring terminal hydroxyl groups or nitrogen-based groups (amine, pyridyl) mimics the monodentate DABCO ligand and binds the copper acetate dimers to their axial positions, thus promoting the [001] growth orientation (layers parallel to the substrate). Contrarily, for carboxyl-terminated SAMs, the most favored coordination mode is as a bidentate ligand that bridges the two metallic cations of the metal dimer. Therefore, on such SAM, the paddle-wheel unit of the $Cu_2(OAc)_4$ precursor is coordinated at its equatorial positions and promotes the [100] growth direction (layers perpendicular to the substrate).

Here, the Au surfaces were functionalized with 4-mercaptomethyl benzoic acid (MBA) or 4-pyridylethyl mercaptan (4pyr) prior to the growth of the thin film by LPE. The resulting orientations of the different samples were determined by PXRD. The diffractogram of DMOF-1(Cu) has two major diffraction peaks at 2θ = 8.4° corresponding to the [100] crystalline plane and at 2θ= 9.1° corresponding to the [001] crystalline plane. Since replacing one of the hydrogen atoms of the terephthalate ligand by a fluorine atom should not lead to any changes in the crystalline lattice, the detection of diffraction peaks at the aforementioned 2θ values are used to determine the crystalline orientation of F-DMOF-1(Cu) grown on the functionalized substrates.

All samples grown on the carboxyl-terminated thiols gave clear diffraction peaks (samples with -M in their label), confirming their crystalline nature. Their diffractograms (Figure 6.3) showed peaks at around 8.4º and 16.8º, evidencing a pure [100] crystalline orientation regardless of any other synthetic conditions of temperature, concentration or sonication and despite clear differences in crystal morphologies as observed with SEM (Figure 6.2). For instance, taking sample CY50-M as reference, using lower temperature and lower linker concentrations (cY20-M) during the synthesis leads to a SURMOF with an identical diffractogram, although significant morphology differences are observed between the two samples.

In the case of pyridyl-functionalized substrates, X-ray diffraction is only observed from samples prepared at high linker concentration and temperature (CY50-P and CN50-P).

Taking into account the observations made in the SEM analysis (Figure 6.2), where similar coatings and crystallite morphologies were detected on carboxylate- and pyridyl-terminated SAMs, these results suggest that F-DMOF(Cu) grows slower (thinner) or with a lower degree of crystallinity on pyridyl-terminated thiols.[14] Moreover, although pyridyl-terminated thiols usually lead to [001] oriented thin films for the DMOF family, we observe a clear [100] orientation for CY50-P (Figure 6.3). The diffractograms of the other samples grown on 4-pyridylethyl mercaptan can be found in Figure S6.3 of the supporting information.

Similar behavior was observed in growth studies performed on the prototypical DMOF (no substitution in the terephthalate linker) and on an analogous SURMOFs with perfluorinated terephthalate linkers, F_4DMOF-1(Cu).[16,36] These studies showed that these materials are prone to twinning defects, a type of crystalline defect that can happen when one of the COO groups in the terephthalate linkers rotates 90° relative to the phenyl plane. The rotation forces the next Cu(I) dimer that coordinates to this COO group to be oriented perpendicular to the Cu(I) dimer at the other end of the ditopic linker. This then leads to an inversion in the local crystalline orientation that can further propagate during the growth of the next layers, eventually shifting the orientation of the entire film. Thus, to synthesize a [001]-oriented film, the number of twinning defects created with each cycle of growth has to be kept to a minimum in order to prevent the gradual reordering of the film to the [100] orientation. This would explain why CN50-P is the only sample to show [001] crystalline orientation. Indeed, with no sonication during the rinsing step, CN50-P was kept free from turbulences or disruptions while the high concentration of the linkers solution and high temperature allowed efficient growth of the film, leading to a strong diffraction peak. CY50-P shows the reverse behavior, bringing up the hypothesis that sonication triggered twinning defects and the subsequent reorientation of the lattice of CY50-P towards the [100] direction. These observations, in agreement with the previously cited studies[16,36], are suggesting the FDMOF-1(Cu) to also be sensitive to twinning defects.

Slight shifts (~ 0.2°) between the diffraction peaks of the samples are observed. We speculate that perhaps different amounts of defects within the crystal structures of the samples, resulting from different growth conditions, are responsible for these shifts. Or, as it was reported for halogenated DMOF-1(Zn),[37] interactions between the fluorine and hydrogen atoms of neighboring linkers could also affect interplanar distances, leading to a shift in diffraction angles. Also, there are some differences in the width of the peaks that are likely to arise from differences in crystallite sizes between samples (Scherrer equation), as observed on SEM images.[38,39] Other factors may also contribute to the observed peak profile but we have not further investigated these phenomena.

Table 6.2: *Comparison of the three linkers of FDMOF-1(Cu) and the orientation of their transition dipole moments of interest relative to the surface of the substrate.*

	DABCO	BDC-(1)		BDC-(2)	
	ν(NCC)	ν_{as}(COO)	ν_{s}(COO)	ν_{as}(COO)	ν_{s}(COO)
[100]	∥	∥	⊥	∥	∥
[001]	⊥	⊥	∥	⊥	∥

Transition dipole moments that are close and parallel to the surface (∥) are attenuated while those perpendicular (⊥) to it are enhanced.

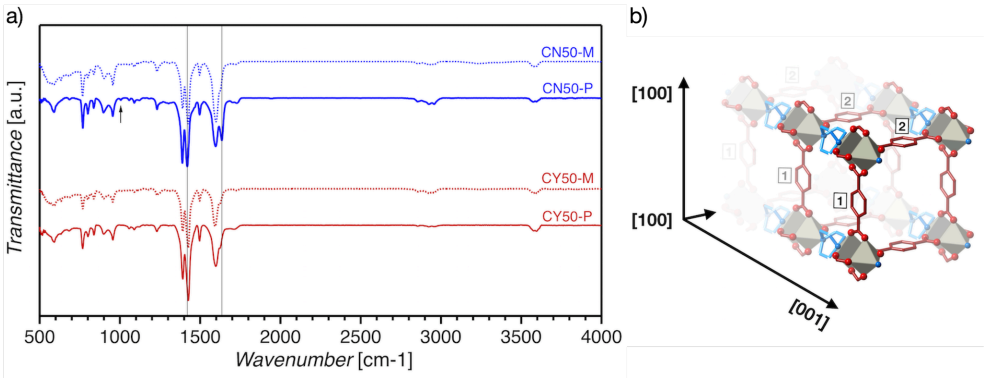

Figure 6.4: (a) IRRAS spectra of CY50-M/P (in red) and CN50-M/P (in blue) taken at an angle of incidence of 70° using non-polarized light. The arrow points at the ν_{s}N-C-C or $\nu_{s}NC_3$ vibrational mode, from the dabco linker, whereas the ν_{s}COO mode and the ν_{as}COO mode in CN50-P are respectively labelled at 1420 cm^{-1} and 1635 cm^{-1}. **(b)** 3D representation of FDMOF-1(Cu) with the DABCO linker in blue and the two terephthalate linkers in red and labelled (1) and (2) to distinguish the contribution of their symmetric and asymmetric COO stretching vibrations in IRRAS (see Table 6.2). Hydrogen and fluorine atoms omitted for clarity.

Infrared Reflection Absorption Spectroscopy (IRRAS) was performed on the best thin films, that is, the ones showing the crystalline structure expected from FDMOF in the PXRD analysis as well as a good coverage in SEM inspection. In IRRAS, the reflection of an infrared beam at low angle (or near grazing incidence) is used on a mirror-like metal surface on top of which the material lays. In such conditions, the electric field vector of the infrared radiation perpendicular to the surface of the substrate is enhanced.[40] Therefore, the detection of IR modes with dipole transition moments perpendicular to the Au-coated substrate from molecules close to the surface is increased, whereas the modes with dipole transition moments parallel to the substrate become strongly attenuated, or suppressed.

In Figure 6.4a, the main differences in the IRRAS spectra of the selected FDMOF samples are the intensity ratio of the carboxylate symmetric to asymmetric stretching modes (respectively at 1425 cm^{-1} and 1625 cm^{-1}) and the presence of the vibrational mode associated to ν_sN-C-C or $\nu_s NC_3$ bond vibration in the spectrum of CN50-P (indicated by the arrow at 1005 cm^{-1} in Figure 6.4a).[41,42] These differences likely arise from the different directions of the transition dipole moments of those vibrational modes related to the surface at each of the two crystalline orientations of the prepared SURMOFs.

The transition dipole moment of the symmetric COO stretching modes is in-plane and along the longitudinal axis of the terephthalate unit, whereas the transition dipole moment of the asymmetric COO stretching mode is also in-plane but perpendicular to the longitudinal axis.[36] On the other hand, the vibrational mode at 1005 cm^{-1} related to the DABCO linker, has a transition dipole moment along the longitudinal axis of the DABCO.

In the [001] configuration, all dicarboxylate linkers are found in the crystalline plane parallel to the surface. However, given the geometry of the copper paddlewheel, the plane containing the carboxylic groups lays perpendicular to the surface. This means that, close to the surface, the asymmetric stretching mode will be enhanced and the symmetric one attenuated. In contrast, for the [100] crystalline orientation, the dicarboxylate linkers are in a plane perpendicular to the substrate, with one terephthalate linker (1) perpendicular to the surface and the other (2) parallel to it. Consequently, the ν_s(COO) of terephthalate (1) could be enhanced and the ones in (2) attenuated, whereas in all cases the ν_{as}COO would be attenuated. In the case of the vibrational mode related to the DABCO linker, only the [001] orientation would show a surface enhancement of the IR absorption. The different combinations are summarized in Table 6.2 and the structure of the material is displayed in Figure 6.4b.

We thus assign the band at 1635 cm^{-1} in CN50-P to the ν_{as}COO. This band is either suppressed or appears as a shoulder at 1626 cm^{-1} (9 cm^{-1} red shift) in the other samples, overlapping with the phenyl vibrational modes (1597 cm^{-1}). The higher intensity of ν_{as}COO in CN50-P is attributed to the different crystalline orientation of this sample compared to the others. As explained above, for a [001] oriented thin film, an enhancement of the ν_{as}COO mode is expected. An analogous behavior for the absorbance ratio between ν_sCOO and ν_{as}COO peaks has been observed in similar SURMOFs.[17] In line with these results, the weak absorption of the vibration mode related to the stretching of the N-C/C-C bonds of the DABCO (1005 cm^{-1}) is only visible for CN50-P, the only thin film in which the diamine linker is found to be perpendicular to the surface.

Regarding the frequency shift of ν_{as}COO and some other bands (see Table S6.1 for the complete peaks assignment), we speculate that they could originate from various sources. In-

phase and out-of-phase vibrations within the crystalline lattice of the MOF can have an effect in the IR frequencies.[43] We can also not dismiss that different defects might be present when the SURMOF is grown in distinct orientations. Yet, the exact origin of the slight shift is outside the scope of this work.

6.4 Conclusions

In this work, we investigated how the characteristics (substrate coverage, morphology, and crystalline orientation) of thin films of Cu(2-fluoroterephthalic acid)(dabco)$_{0.5}$, FDMOF-1(Cu), are affected by factors such as the substrate functionalization, growth temperature, reagents concentration, and use of sonication during the rinsing step of the Liquid Phase Epitaxy method. As a result, highly oriented SURMOFs layers of FDMOF-1(Cu) were obtained while relationships between layer morphology and reagent concentrations, as well as between crystalline orientation and substrate functionalization were highlighted. To the best of our knowledge, this is the first report of the synthesis of Cu(2-fluoroterephthalic acid)(dabco)$_{0.5}$.

We showed that 20 cycles of growth using the Liquid Phase Epitaxy method on thiol-functionalized Au substrates yield better layers when the synthesis is performed at 50 °C and common linkers' concentrations than at 20 °C or using low linkers' concentration. The temperature of the solutions also influenced the morphology of the crystal, yielding needle-shaped crystals at 20 °C and square-shaped crystals at 50°C. Surprisingly, PXRD analysis revealed that both carboxylic- and pyridine-functionalized substrates yielded the [100] orientation. Only a unique set of conditions (high linkers' concentration, high temperature, no sonication, pyridyl-terminated SAM) lead to a [001] oriented film. This suggests that FDMOF is sensitive to twinning defects occurring at early stages of the growth of the thin film, similarly to previously reported studies on other specimens of the DMOF family. These observations suggest that the nature of the SAM used to functionalize the substrate does not always play the main role in the determination of the orientation of the thin film as the final properties of the SURMOF rely on a delicate combination of various parameters, that even varies if other linkers are used.

Bibliography

1. Furukawa, H. *et al.* The chemistry and applications of metal-organic frameworks. *Science (80).* **341**, (2013).
2. Yuan, S. *et al.* Stable Metal–Organic Frameworks: Design, Synthesis, and Applications. *Adv. Mater.* **30**, 1–35 (2018).
3. Li, H., Addaoudi, M., O'Keeffe, M. & Yaghi, O. M. Design and synthesis of an exceptionally stable and highly porous metal-organic framework. *Nature* **402**, 276–279 (1999).
4. Moghadam, P. Z. *et al.* Development of a Cambridge Structural Database Subset: A Collection of Metal-Organic Frameworks for Past, Present, and Future. *Chem. Mater.* **29**, 2618–2625 (2017).
5. Ameloot, R. *et al.* An updated roadmap for the integration of metal-organic frameworks with electronic devices and chemical sensors. *Chem. Soc. Rev.* **46**, 3185–3241 (2017).
6. Stock, N. & Biswas, S. Synthesis of metal-organic frameworks (MOFs): Routes to various MOF topologies, morphologies, and composites. *Chem. Rev.* **112**, 933–969 (2012).
7. Münch, A. S. *et al.* Room temperature preparation method for thin MOF-5 films on metal and fused silica surfaces using the controlled SBU approach. *Microporous Mesoporous Mater.* **159**, 132–138 (2012).
8. Zacher, D., Shekhah, O., Wöll, C. & Fischer, R. A. Thin films of metal-organic frameworks. *Chem. Soc. Rev.* **38**, 1418–1429 (2009).
9. Heinke, L., Gliemann, H., Tremouilhac, P. & Wöll, C. SURMOFs: Liquid-Phase Epitaxy of Metal-Organic Frameworks on Surfaces. in *The Chemistry of Metal-Organic Frameworks: Synthesis, Characterization, and Applications* 523–550 (Wiley-VCH Verlag GmbH & Co. KGaA, 2016). doi:10.1002/9783527693078.ch17.
10. Gu, Z. G. & Zhang, J. Epitaxial growth and applications of oriented metal–organic framework thin films. *Coord. Chem. Rev.* **378**, 513–532 (2019).
11. Liu, J. & Wöll, C. Surface-supported metal-organic framework thin films: Fabrication methods, applications, and challenges. *Chem. Soc. Rev.* **46**, 5730–5770 (2017).
12. Frameworks for commercial success. *Nat. Chem.* **8**, 987 (2016).
13. Urquhart, J. World's first commercial MOF keeps fruit fresh. *Chemistry World* (2016).
14. Seoane, B., Castellanos, S., Dikhtiarenko, A., Kapteijn, F. & Gascon, J. Multi-scale crystal engineering of metal organic frameworks. *Coord. Chem. Rev.* **307**, 147–187 (2016).

15. Meshkov, I. N. *et al.* Understanding Self-Assembly of Porphyrin-Based SURMOFs: How Layered Minerals Can Be Useful. *Langmuir* **34**, 5184–5192 (2018).
16. McCarthy, B. D., Liseev, T., Beiler, A. M., Materna, K. L. & Ott, S. Facile Orientational Control of M_2L_2P SURMOFs on <100> Silicon Substrates and Growth Mechanism Insights for Defective MOFs. *ACS Appl. Mater. Interfaces* **11**, 38294–38302 (2019).
17. Yu, X. J. *et al.* Liquid-Phase Epitaxial Growth of Highly Oriented and Multivariate Surface-Attached Metal-Organic Frameworks. *J. Am. Chem. Soc.* **141**, 18984–18993 (2019).
18. Summerfield, A., Cebula, I., Schröder, M. & Beton, P. H. Nucleation and Early Stages of Layer-by-Layer Growth of Metal Organic Frameworks on Surfaces. *J. Phys. Chem. C* **119**, 23544–23551 (2015).
19. Wang, Z., Rodewald, K., Medishetty, R., Rieger, B. & Fischer, R. A. Control of Water Content for Enhancing the Quality of Copper Paddle-Wheel-Based Metal-Organic Framework Thin Films Grown by Layer-by-Layer Liquid-Phase Epitaxy. *Cryst. Growth Des.* **18**, 7451–7459 (2018).
20. Wang, Z. *et al.* Directing the hetero-growth of lattice-mismatched surface-mounted metal–organic frameworks by functionalizing the interface. *J. Mater. Chem. A* **6**, 21295–21303 (2018).
21. Gonzalez-Nelson, A., Coudert, F. X. & van der Veen, M. A. Rotational dynamics of linkers in metal–organic frameworks. *Nanomaterials* **9**, (2019).
22. Namsani, S. & Yazaydin, A. O. Electric field induced rotation of halogenated organic linkers in isoreticular metal-organic frameworks for nanofluidic applications. *Mol. Syst. Des. Eng.* **3**, 951–958 (2018).
23. Ohnsorg, M. L., Beaudoin, C. K. & Anderson, M. E. Fundamentals of MOF Thin Film Growth via Liquid-Phase Epitaxy: Investigating the Initiation of Deposition and the Influence of Temperature. *Langmuir* **31**, 6114–6121 (2015).
24. Shekhah, O. Layer-by-Layer Method for the Synthesis and Growth of Surface Mounted Metal-Organic Frameworks (SURMOFs). *Materials.* **3**, 1302–1315 (2010).
25. Ohhashi, T., Tsuruoka, T., Fujimoto, S., Takashima, Y. & Akamatsu, K. Controlling the Orientation of Metal-Organic Framework Crystals by an Interfacial Growth Approach Using a Metal Ion-Doped Polymer Substrate. *Cryst. Growth Des.* **18**, 402–408 (2018).
26. Liu, B., Tu, M. & Fischer, R. A. Metal-organic framework thin films: Crystallite orientation dependent adsorption. *Angew. Chemie Int. Ed.* **52**, 3402–3405 (2013).
27. Huelsenbeck, L. *et al.* Modulating and orienting an anisotropic Zn-based metal organic framework for selective CH_4/CO_2 gas separation. *Crystals* **9**, 7–11 (2019).
28. Chen, S.-M., Liu, M., Gu, Z.-G., Fu, W.-Q. & Zhang, J. Chiral Chemistry of Homochiral Porous Thin Film with Different Growth Orientations. *ACS Appl. Mater. Interfaces* **8**, 27332–27338 (2016).

29. Vaitsis, C., Sourkouni, G. & Argirusis, C. Metal Organic Frameworks (MOFs) and ultrasound: A review. *Ultrason. Sonochem.* **52**, 106–119 (2019).
30. Safarifard, V. & Morsali, A. Applications of ultrasound to the synthesis of nanoscale metal-organic coordination polymers. *Coord. Chem. Rev.* **292**, 1–14 (2015).
31. Gu, Z. G. *et al.* Transparent films of metal-organic frameworks for optical applications. *Microporous Mesoporous Mater.* **211**, 82–87 (2015).
32. Tehrani, A. A., Safarifard, V., Morsali, A., Bruno, G. & Rudbari, H. A. Ultrasound-assisted synthesis of metal-organic framework nanorods of Zn-HKUST-1 and their templating effects for facile fabrication of zinc oxide nanorods via solid-state transformation. *Inorg. Chem. Commun.* **59**, 41–45 (2015).
33. Burtch, N. C., Dubbeldam, D. & Walton, K. S. Investigating water and framework dynamics in pillared MOFs. *Mol. Simul.* **41**, 1379–1387 (2015).
34. Grosch, J. S. & Paesani, F. Molecular-level characterization of the breathing behavior of the jungle-gym-type DMOF-1 metal-organic framework. *J. Am. Chem. Soc.* **134**, 4207–4215 (2012).
35. Shen, C. *et al.* Structure of isophthalic acid based monolayers and its relation to the initial stages of growth of metal–organic coordination layers. *Chem. Sci.* **3**, 1858 (2012).
36. Grytz, C. M. *et al.* Insight into the Oriented Growth of Surface-Attached Metal–Organic Frameworks: Surface Functionality, Deposition Temperature, and First Layer Order. *J. Am. Chem. Soc.* **137**, 8237–8243 (2015).
37. Burrows, A. D. *et al.* Compositional control of pore geometry in multivariate metal–organic frameworks: an experimental and computational study. *Dalt. Trans.* **45**, 4316–4326 (2015).
38. Patterson, A. L. The Scherrer Formula for X-Ray Particle Size Determination. *Phys. Rev.* **56**, 978–982 (1939).
39. Langford, J. I. & Wilson, A. J. C. Scherrer after sixty years: A survey and some new results in the determination of crystallite size. *J. Appl. Crystallogr.* **11**, 102–113 (1978).
40. Nishikawa, Y., Osawa, M., Ataka, K.-I. & Yoshii, K. Surface-Enhanced Infrared Spectroscopy: The Origin of the Absorption Enhancement and Band Selection Rule in the Infrared Spectra of Molecules Adsorbed on Fine Metal Particles. *Appl. Spectrosc.* **47**, 1497–1502 (1993).
41. Guzonas, D. A. & Irish, D. E. A Raman and infrared spectroscopic study of triethylenediamine (DABCO) and its protonated forms. *Can. J. Chem.* **66**, 1249–1257 (1988).
42. McDivitt, J. & Humphrey, G. Spectroscopic studies of the boron trihalide and borane complexes of 1,4-diazabicyclo[2.2.2]octane and quinuclidine. **30**, 1021–1033 (1973).
43. Hermans, J. J. *et al.* 2D-IR spectroscopy for oil paint conservation: Elucidating the

water-sensitive structure of zinc carboxylate clusters in ionomers. *Sci. Adv.* **5**, 1–10 (2019).

Summary

The sustained efforts of the semiconductor industry to continuously downscale the dimensions of transistors and electronic circuitries in computer chips strain photoresist research. We have seen a drastic increase in the performance requirements of photoresists due to the recent development of extreme ultraviolet lithography (EUVL), while the fundamental understanding of the chemical changes triggered in these materials upon EUV exposure remains incomplete. The intricacy of the relevant physical and chemical processes, and the limited opportunities for *in-situ* chemical analysis of the thin resist films hinder the development of optimal EUV photoresists. In this thesis, we explore new methods and materials for EUVL to propose new directions for photoresist research and provide insights on EUV-triggered phenomena.

Chapter 1 introduces photolithography, its central role in the fabrication of computer chips and its close relationship with the economic agenda of the semiconductor industry. The operating principle and limitations of EUV lithography and EUV photoresists are also presented, followed by an introduction on metal-organic frameworks (MOFs), self-assembled monolayers (SAMs) and their possible association to EUVL. MOFs are crystalline, tunable and porous organic-inorganic materials with many attractive properties that material scientists and industrials try to exploit in various applications, such as sensors, catalysis, gas storage, membranes, *etc*. SAMs are monolayers of molecules that can bond to a certain substrate to modify its surface properties. In this work we use them to enable the (local) growth of thin films of MOFs, called surface-mounted metal-organic frameworks (SURMOFs), with the SAM acting as a chemically selective anchor between the substrate and the material. In the next chapters, SURMOFs and SAMs are used to investigate the chemical processes induced during EUV exposure and explore new perspectives for EUVL.

Chapter 2 explores the EUV reactivity and patterning performances of two copper-based SURMOFs, namely copper oxalate, or $Cu(C_2O_4)•nH_2O$, and HKUST-1(Cu), or $Cu_3(BTC)_2$,

where BTC stands for benzene-1,3,5-tricarboxylate. Significant differences of the sensitivities of the two materials were evidenced by X-ray photoelectron spectroscopy (XPS) and we quantify this by calculating their quantum yields for decarboxylation, an essential reaction for the generation of the solubility switch required for patterning in these materials. The differences observed between the quantum yields of the two SURMOFs far exceeded the differences in their EUV absorptivity, suggesting that the efficiency of the fragmentation mechanisms has a larger contribution to the resist's sensitivity. $Cu(C_2O_4)•nH_2O$ proves significantly more reactive, with potential for patterning at doses that are close to those targeted by industry (visible contrast obtained at ~15 mJ/cm^2) while HKUST-1(Cu) remains inert to EUV at conventional doses (up to 250 mJ/cm^2).

Chapter 3 studies the EUV reactivity of perfluorinated SAMs of thiols on gold by means of *in-situ* photoelectron spectroscopy (PES). Although the SAMs are virtually transparent to EUV photons, our experiments showed that the thiol molecules on the surface of the substrates start to fragment around 20 mJ/cm^2. We estimated that ~40% of the fluorine content of the SAM was desorbed after a dose of 200 mJ/cm^2. These observations demonstrate that EUV can simultaneously generate significant structural contrast, by reducing the quality of the molecular packing at the exposed areas, and chemical contrast, by altering the chemical composition of the exposed areas through the fragmentation of thiol molecules. This research was conducted at the BEAR beamline of the ELETTRA synchrotron in Trieste, Italy.

Chapter 4 describes a novel bottom-up method for EUVL that relies on the sensitivity of thiol SAMs towards EUV light, demonstrated in Chapter 3, and their essential role in SURMOF growth. In this method, the substrate absorbs most of the 92 eV photons and serves as a generator of low-energy electrons. The photoelectrons and secondary electrons escaping from the substrate trigger various fragmentation events and chemical reactions in the SAM through inelastic scattering. At this stage of the procedure the nanopatterns are materialized within the SAM as chemical contrast. As the molecular packing of the SAM decreases, their desorption rate increases, thus enabling the selective exchange of the molecules comprised in the exposed areas of the SAM. This procedure, which we call exchange-step, increases the chemical contrast of the patterns and could enable the deposition and/or growth of various materials with nm scale spatial selectivity. Here, we demonstrate the feasibility of our method by growing the SURMOF of HKUST-1(Cu) on EUV exposed and exchanged SAMs.

In the last chapters of this thesis, we investigate how different variables affect the growth of a selected set of SURMOFs. The study of the synthesis of these materials is of major importance for the device integration of MOFs and for the version of the bottom-up method presented in Chapter 4, in which precise synthetic control is required to reach successful nanometer scale spatial precision during growth.

Chapter 5 investigates the influence of the functional group attached to the dicarboxylate linkers of X-DMOF-1(Cu) on the properties of their thin films. X-DMOF-1(Cu) stands for $Cu_2(X\text{-}BDC)_2(DABCO)$ where BDC = benzene dicarboxylic acid, X symbolizes the

functional group attached to the BDC and DABCO = 1,4-diazabicyclo[2.2.2]octane). Layer-by-layer (LbL) liquid phase epitaxy (LPE) is used as synthesis method. We observe significant differences in substrate coverage, topography and crystallinity between films of DMOF-1(Cu), F-DMOF-1(Cu), Br-DMOF-1(Cu), NO_2-DMOF-1(Cu) and F_4-DMOF-1(Cu). We show that synthesis conditions cannot simply be transferred from one SURMOF to another, even for comparable materials. Moreover, in the conditions of our study, the expected templating effect promoted by the terminal functional group of the SAM molecules is not observed. This means that the SURMOF's crystalline orientation relative to the surface is not affected by using SAMs with functional groups that preferentially coordinate to the apical or equatorial position of the inorganic nodes of the hybrid material. These observations contradict previously reported studies on the growth of other species of SURMOFs. Although we could not identify with certainty the nature and amount of influence of the other synthesis parameters, comparing our results to those of the aforementioned studies on the matter shows that the final properties of MOF thin films are governed by an intricate combination of potentially interdependent factors.

In **Chapter 6** we focus on the effects of the synthesis conditions during LbL LPE on the properties of thin films of F-DMOF-1(Cu), or $[Cu_2(FBDC)_2(DABCO)]$ where FBDC = 2-fluoroterephthalic acid, grown on thiol functionalized gold substrates. During LbL synthesis the substrates are successively immersed in solutions containing the inorganic constituents of the SURMOF (copper ions) and solutions containing its organic constituents (linkers). A rinsing step is usually added between immersions in an effort to constrain the growth to a single layer of material per cycle. The effects of the temperature of the solutions, the linkers' concentration, the presence or absence of sonication during the rinsing step and the type of SAM are tested. We report that higher temperatures and concentrations yield layers with relatively better homogeneity and coverage. The temperature of the solution also influences the shape of the crystals contained within the thin films, and thus their topography. As seen in chapter 5, the crystalline orientation of the SURMOFs remains unaffected by the nature of the SAM, with the exception of a unique set of parameters. These observations suggest that the SURMOF's properties are dynamic during growth and rely on interdependent parameters which determination is likely to require extensive systematic for every type of MOF and synthesis method. Chapter 5 and 6 highlight the need for the creation of accurate growth models as the development of many MOF-containing devices heavily relies on precise synthetic control.

Samenvatting

Het voortdurende streven van de halfgeleiderindustrie naar het verkleinen van transistoren en elektronische circuits in computerchips heeft geleid tot de ontwikkeling van Extreem Ultraviolet Lithografie (EUVL). In lithografie worden fotolakken (in het Engels: photoresists) gebruikt om een lichtafbeelding om te zetten in een patroon in de vorm van een dunne laag op een siliciumchip. Door deze recente ontwikkelingen worden steeds hogere eisen gesteld aan de nauwkeurigheid en betrouwbaarheid van fotolakken, terwijl nauwelijks bekend is wat er in deze materialen gebeurt wanneer ze worden blootgesteld aan EUV licht, dat een veel kortere golflengte heeft dan het gebruikelijke ultraviolet licht. De combinatie van een gebrek aan kennis van de fysische en chemische processen en beperkte mogelijkheden voor het onderzoeken van de chemische structuur van dunne laagjes materiaal maakt de ontwikkeling van optimale EUV fotolakken tot een grote uitdaging.

Hoofdstuk 1 introduceert de evolutie van fotolithografie, de centrale rol die deze inneemt in de fabricatie van computerchips en de hechte relatie met de economische agenda van de halfgeleiderindustrie. De grondbeginselen en beperkingen van EUVL en EUV fotolakken worden beschreven. Tevens worden metaal-organische roosters (metal-organic frameworks in het Engels, kortweg MOF's) en moleculaire monolagen (self-assembled monolayers in het Engels, kortweg SAM's) besproken. MOF's en SAM's materialen zijn gebruikt in dit onderzoek om door EUV licht geïnduceerde chemische processen te onderzoeken en nieuwe perspectieven voor EUVL te openen.

Hoofdstuk 2 verkent de EUV reactiviteit en de patroonvorming van twee op koper gebaseerde SURMOF's, namelijk koper oxalaat, ($Cu(C_2O_4)•nH_2O$), en HKUST-1(Cu), oftewel $Cu_3(BTC)_2$, waarin BTC staat voor benzeen-1,3,5-tricarboxylaat. Röntgen foto-elektron spectroscopie (XPS) laat significante verschillen in gevoeligheid zien tussen deze twee materialen. De kwantumopbrengsten voor de decarboxylatiereacties van beide materialen zijn bepaald, aangezien deze reacties essentieel zijn voor de omschakeling van

oplosbaarheid die de basis vormt voor patroonvorming na bestraling met licht. De verschillen in de kwantumopbrengst van de twee SURMOF's blijken aanzienlijk groter dan de verschillen in hun vermogen om EUV licht te absorberen. Dit geeft aan dat de efficiëntie van fragmentatiereacties van groter belang is dan het aantal fotonen dat geabsorbeerd wordt. Voor beide materialen worden reactiemechanismen voorgesteld op basis van eerdere studies naar hun reactiviteit ten opzichte van lage-energie elektronen. $Cu(C_2O_4)•nH_2O$ bleek significant meer reactief, met potentieel voor patroonvorming bij doses die dicht bij de door de industrie beoogde waarden liggen (zichtbaar contrast verkregen bij ca. 15 mJ/cm²), terwijl HKUST-1 (Cu) inert is voor EUV bij conventionele doses (tot 250 mJ/cm²).

Hoofdstuk 3 bestudeert de EUV-reactiviteit van fluor-bevattende SAM's van thiolen op goud door middel van in-situ foto-elektron spectroscopie (PES). Hoewel vrijwel transparant voor EUV-fotonen, worden de thiolmoleculen op het oppervlak van de substraten gesplitst tijdens blootstelling aan EUV. Deze waarnemingen tonen aan dat EUV tegelijkertijd een significant structureel contrast kan genereren, dat voortkomt uit de verminderde kwaliteit van de moleculaire pakking in de blootgestelde gebieden, en een chemisch contrast, veroorzaakt door de verschillende chemische samenstelling van de blootgestelde gebieden, bestaande uit gefragmenteerde thiolmoleculen. Dit onderzoek werd uitgevoerd aan de BEAR bundellijn van het ELETTRA synchrotron in Triëst, Italië.

Hoofdstuk 4 beschrijft een nieuwe "bottom-up" methode voor EUVL gebaseerd op de gevoeligheid van thiol SAM's voor EUV-licht, zoals aangetoond in hoofdstuk 3, en hun essentiële rol bij de groei van SURMOF's. Bij deze methode absorbeert het substraat de meeste van de 92 eV-fotonen en dient het als generator van elektronen met lage energie. De fotoelektronen en secundaire elektronen die uit het substraat ontsnappen veroorzaken verschillende fragmentaties en chemische reacties in de SAM door inelastische verstrooiing. In dit stadium van het proces komen de nanopatronen in de SAM tot uiting als een chemisch contrast. De evenredigheid tussen de desorptiesnelheid in oplossing van thiolen en de pakkingskwaliteit van de monolaag die ze vormen, maakt de selectieve uitwisseling van de moleculen in het blootgestelde gebied door andere thiolmoleculen mogelijk. Deze procedure verhoogt het chemische contrast tussen blootgestelde en niet-blootgestelde gebieden en maakt de afzetting en groei van materialen met ruimtelijke selectiviteit op nanometer-schaal mogelijk. Hier demonstreren we de haalbaarheid van onze methode door SURMOF's van HKUST-1 (Cu) te laten groeien.

In de laatste hoofdstukken van dit proefschrift bestuderen we hoe verschillende variabelen de groei van een selectie van SURMOF's beïnvloeden. Het bestuderen van SURMOF's is van groot belang voor de technische toepassing van MOF's en voor de versie van de "bottom-up" methode gepresenteerd in hoofdstuk 4, waar selectieve groei met ruimtelijke precisie op nanometer-schaal vereist is.

Hoofdstuk 5 onderzoekt het effect van liganden van X-DMOF-1(Cu), of Cu_2 (X-BDC)$_2$(DABCO) waarbij BDC = benzeen dicarbonzuur; DABCO = 1,4-diazabicyclo[2.2.2]octaan en X de functionele groep gehecht aan de dicarboxylaatliganden

symboliseert, op basis van de eigenschappen van hun dunne films. Laag-voor-laag (layer-by-layer in het Engels, kortweg LbL) vloeistof-epitaxie (liquid phase epitaxy in het Engels, kortweg LPE) wordt gebruikt als synthesemethode. We zien significante verschillen in substraatdekking, topografie en kristalliniteit tussen films van DMOF-1(Cu), F-DMOF-1(Cu), Br-DMOF-1(Cu), NO_2-DMOF-1(Cu) en F_4-DMOF-1(Cu). Deze waarnemingen laten zien dat gedetailleerde syntheseprocedures niet eenvoudig van de ene SURMOF naar de andere kunnen worden overgedragen. De vergelijking van onze resultaten met die van eerdere studies over de kwestie bevestigt verder dat de invloed van syntheseomstandigheden op de uiteindelijke eigenschappen van deze films complex is en gebaseerd is op onderling afhankelijke factoren die we nog niet voldoende kennen.

In **hoofdstuk 6** richten we ons op de effecten van de syntheseomstandigheden tijdens LbL LPE op de eigenschappen van dunne films van F-DMOF-1(Cu), of [Cu_2 $(fbdc)_2(dabco)$], gekweekt op thiol gefunctionaliseerde goudsubstraten. Tijdens de LbL-synthese worden de substraten achtereenvolgend ondergedompeld in oplossingen die de anorganische bestanddelen (koperionen) van de SURMOF bevatten en oplossingen die de organische bestanddelen ervan (liganden) bevatten. Doorgaans wordt een spoelstap toegevoegd tussen de onderdompelingen in om de groei te beperken tot een enkele laag materiaal per cyclus. De effecten van de temperatuur van de oplossingen, de concentratie van de liganden, de aan- of afwezigheid van sonificatie tijdens de spoelstap en het type SAM worden getest. De waarnemingen in dit hoofdstuk en in hoofdstuk 5 vragen om uitgebreide experimentele studies naar de groei van SURMOFs en de ontwikkeling van groeimodellen om optimale groeiomstandigheden te achterhalen.

Outlook

The following paragraphs detail additional uses of SURMOFs and SAMs for EUV lithography and beyond. The feasibility of these concepts could not be explored due to limitations in time and resources despite appealing potential.

MOFs as matrices of nm-scale reactors.
Most 3D MOFs display astonishing levels of porosity. These pores and channels can be loaded with various guest molecules, such as polymers, complexes, metal-oxo clusters, etc. One could take advantage of this property to expose compounds to EUV which could otherwise not be easily irradiated as deposited films on a substrate (e.g. volatile compounds) or other limitations. Moreover, the type of matrix of nm scale reactors with a precise spatial ordering can only be provided by metal organic frameworks. Previous reports have shown that in-pore polymerization is possible in MOFs with various benefits to the properties of the final polymer product. SURMOFs such as HKUST-1(Cu) with low EUV reactivity, could provide an interesting platform for such a method as their structural properties would remain mostly unaffected by the exposure while metal and oxygen atoms deliver low energy electrons to the guests.

EUV-tailored SAMs.
Chapters 3 and 4 proved that monolayers of organic molecules chemically bonded to the surface of a substrate can be damaged during EUV exposure, although the organic monolayer is practically transparent to EUV light. In our method, we used highly fluorinated thiol molecules as the exposed self-assembled monolayer (SAM) because their numerous fluorine atoms prevent SURMOF growth and can easily generate strong chemical contrast between exposed and unexposed areas following desorption. The limiting factor of SAM patterning is the efficiency of the chemical reactions leading to desorption or chemical changes. By designing SAM molecules comprising a functional group easily cleavable upon interaction

with low energy electrons, one could create a highly EUV sensitive monolayer. Linear and branched alkane thiols (or silanes) with a peroxide bond included in their spacer or a terminal groups composed of a -CF_3, -COOH or a -CF_2-CF_3 (i.e., 4,4,4-Trifluoro-3-(trifluoromethyl)-1-butanethiol, 4-mercatpobutyric acid and 4,4,5,5,5-Pentafluoro-1-pentanethiol) are a few examples of molecules from which EUV-designed SAMs could be based upon.

Furthermore, if these molecules are designed in such way that the new functional groups at their extremities after cleavage has different chemical properties than this of the pristine molecules, the exchange step is not needed and material can be selectively deposited immediately following exposure. Getting rid of the exchange step will enhance performance as the number of defects is usually proportional to the number of steps in the patterning procedure.

Anisotropic patterning (direction-controlled polymerization)

MOFs composed of more than one type of linker can have anisotropic unit cells. The specimens of [M_2L_2P] MOFs discussed in Chapter 5 and Chapter 6 of this thesis are a good example of such materials. Because their linkers have different lengths, the resulting interplanar distances are also different depending on the crystalline orientation. Therefore, one could design [M_2L_2P] MOFs comprised of "L" linkers longer than the "P" linkers in which interlinker polymerisation would be geometrically constrained to a single direction (vertical or horizontal).

Three conditions are required to design such material; (1) the "L" linkers should be functionalised by functional groups comprising polymerizable units at their extremities capable of crosslinking with units from neighbouring linkers upon EUV irradiation; (2) the functional groups should be too short for their polymerizable units to contact the units of linkers present within the same "L-L" plane, (3) the functional groups should be long enough to enable their polymerizable units to crosslink with those of linkers present within the same "L-P" plane. The following schemes illustrate this concept.

In such MOFs and SURMOFs, the direction of the EUV-triggered polymerisation would be exclusively determined by their crystalline orientations. This means that, in a system that promotes vertical polymerization, the line edge roughness (lateral blur) of the patterns caused by patterning stochastics during exposure would be drastically reduced, if not suppressed. The polymerized areas of the material would remain on the surface of the substrate following a development procedure that targets the inorganic nodes of the SURMOF, similarly to the method used in Chapter 2 of this thesis.

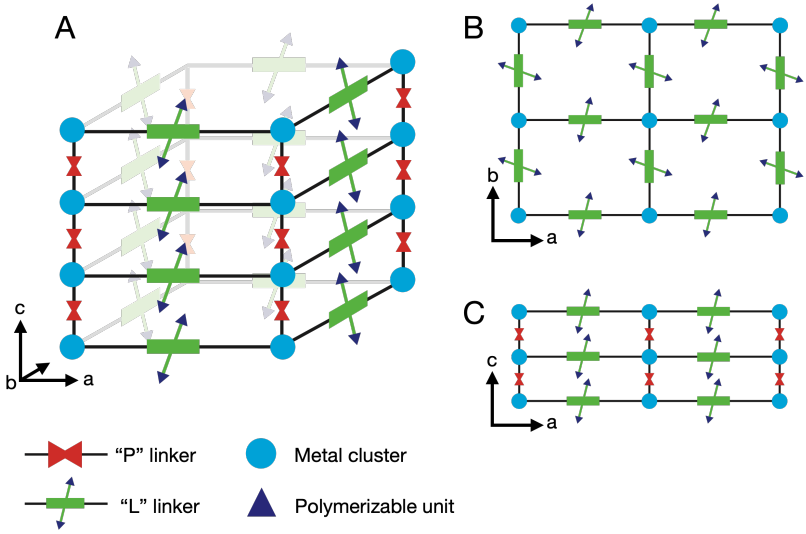

Figure: (A) 3D scheme of the channel of a hypothetical [M_2L_2P] MOF. **(B)** and **(C)** 2D schemes of four channels of the same hypothetical MOF, seen along the c direction and the b direction, respectively. In the text, **(B)** is described as the "L-L" plane and **(C)** the "L-P" plane.

This concept and the aforementioned idea of using MOFs as nm-scale reactors can be combined to obtain directional control over the in-pore polymerization of monomers. Considering an [M_2L_2P] MOF as an example, a specimen could be designed so that the "L-P" pores (made of two L and two P linkers) would be chemically or geometrically shut for any guest to pass through, preventing guest-guest interaction in this direction. In the [M_2L_2P] example, because these MOFs have two "L-P" pores for one "L-L" pore, the polymerization would thus be restricted to a unique direction determined by the crystalline orientation of the SURMOF.

List of publications

This thesis is based on the following publications:

Chapter 2: Lugier, O.; Amairi, M.N.; Castellanos, S.; "Copper-based SURMOFS as photoresists for EUV lithography"; manuscript in preparation.

Chapter 3: Lugier, O.; Troglia, A.; Sadegh, N.; van Kessel, L.; Bliem, R.; Mahne, N.; Nannarone, S.; Castellanos, S. Extreme Ultraviolet Photoelectron Spectroscopy on Fluorinated Monolayers: Towards Nanolithography on Monolayers. *J. Photopolym. Sci. Technol.* **2020**, *33* (2), 229–234.

Chapter 4: Lugier, O.; Thakur, N.; Wu, L.; Vockenhuber, M.; Ekinci, Y.; Castellanos, S.; "Bottom-up nanofabrication with extreme ultraviolet light: metal-organic frameworks on patterned monolayers"; manuscript under revision.

Chapter 5: Lugier, O.; Amairi, M.N.; Castellanos, S.; "Effect of the linkers' functionalization on the synthesis of SURMOFs from the DMOF-1(Cu) family"; manuscript in preparation.

Chapter 6: Lugier, O.; Pokharel, U.; Castellanos, S.; "Impact of Synthetic Conditions on the Morphology and Crystallinity of FDMOF-1(Cu) Thin Films" *Cryst. Growth Des*. **2020**, 20 (8), 5302–5309.

Other publications:

Muscarella, L.; Petrova, D.; Jorge Cervasio, R.; Farawar, A.; Lugier, O.; McLure, C.; Slaman, M.J.; Wang, J.; Ehrler, B.; von Hauff, E.; Williams R.M.; "Air-Stable and Oriented Mixed Lead Halide Perovskite (FA/MA) by the One-Step Deposition Method Using Zinc

Iodide and an Alkylammonium Additive"; *ACS Applied Materials & Interfaces*; **2019**, 11 (19), 17555-17562

Wu, L.; Bespalov, I.; Witte, K.; Lugier, O.; Haitjema, J.; Vockenhuber, M.; Ekinci, Y.; Watts, B.; Brouwer, A.M.; Castellanos, S.; "Unravelling the effect of fluorinated ligands in hybrid EUV photoresists by X-ray spectroscopy"; *J. Mater. Chem. C*, **2020**, 8, 14757-14765

Zhang, Y.; Haitjema, J.; Castellanos, S.; Lugier, O.; Sadegh, N.; Ovsyannikov, R.; Giangrisostomi, E.; Johansson, F.O.L.; Berggren, E.; Lindblad, A.; Brouwer, A.M.; "Extreme Ultraviolet photoemission of a tin-based photoresist"; manuscript submitted

Acknowledgements

Reflecting on the last four and a half years and the defining chapter of my life that my PhD has been, I feel a blend of nostalgia and gratitude. It was an incredible journey, at times quite annoying too, that was made possible by countless interactions with many people. I would like to now express my gratitude to them for their help and support in the completion of this long-time goal of mine.

Firstly, I want to express my deepest gratitude to both my supervisors Dr. Sonia Castellanos and Prof. Fred Brouwer.
Sonia, thank you so much for giving me the opportunity to join your group. Working with you was a pleasure thanks to your relentless encouragements, constant enthusiasm and your amazing personality. I learned as much as I had fun. Fred, thank you for your many advices and remarks, whether they were directed to me as a student, scientist or individual, they have been highly beneficial for my development. Thank you both for teaching me so much and helping me better myself by emulating you.

Thank you to prof. dr. P. Swiderek, dr. S. Grecea, dr. R.M. Williams, prof. dr. M.S. Golden and dr. ir. M.A. van der Veen for reviewing my thesis and participating in the defense committee.

Marjan and Joost, thank you for your availability and continuous efforts to make it easy for us to conduct our research in and out of ARCNL. Romy, Rosa and Cathelijne, thank you for your kind help and support, I enjoyed very much chatting with you at the entrance or coffee machine in the morning.
My special thanks to previous and current group members both from Nanophotochemistry and EUV photoresists group in ARCNL. Regardless of the state of my research (or motivation), you made it easy for me to come to work. Lianjia, four years working with you and you have only made my life easier. Thank you for your help in the lab, wise suggestions

and mental support. Neha, thank you for the laughs, being there to listen to me complain and for the long night shift conversations at the synchrotron (and for being my paranymph). Najmeh, thank you for the good times at the institute, the funny conversations travelling to the synchrotron or conferences and for trying to explain particle physics to me (and for being my paranymph). Yu, thanks for all your synchrotron tips and for being a model of organization and planning to all of us. Jarich, thanks for the synthesis tips and nice chats. Ivan, thanks for the good times at the synchrotron, that moon eclipse was amazing. Aniket, thank you for your extensive AFM help in the early days of my PhD. Robbert, thank you for the amazing food and the outings photos. Maarten, thank you for the random science discussions during lunch. To the students I supervised, Hans, Kendra, Unnati, Wenqian, Marie-Noelle, Felix, it was a pleasure working with you, thank you for the help in the lab.

My gratitude also goes to all of my colleagues from ARCNL/AMOLF/ASML for making the institute such a great place to work. Randy, Mengqi, Feng-Chun, Ruben, Victor, Peter, Stephen, Bo, Oscar, Thomas, Vanessa, Tiago, Jan, Cristina, Ale, the other Ale, John, Fiona, Filippo, Sylvianne, Roland, Stefan, Christian, Claire, Wim, Evgenia, Alexey, Jim and those that I forgot to mention, thank you.

Thank you to my other colleagues from the Molecular Photonics group of UvA for welcoming me as a part-time group member. Thank you to the staff members, Prof. Wybren Jan Buma, Prof. Sander Woutersen, Dr. René Williams (thank you for giving me the opportunity to come to UvA 6 years ago, this is where it all started), Prof. Hong Zhang and Dr. Annemieke Petrignani for your kind help and suggestions during the group meetings or at the coffee machine. Mina, Dina, Bert, Benjamin, Bruno, Roberto, Mark, Floor, Steven, Tomislav, Maximilian, Hernan, Wim, Elena, Aylin, Janita, Aishwarya, Charlotte, Chris, Dongdong, Hung-Cheng, Rafael, Yanni, Jiayun, Ivan, Loretta, Lotte, Rebecca, and those that I forgot, thank you all for the lunches, drinks, outings, group meetings, soccer tournaments, diners at Oerknal and the great memories.

Thank you to all the technicians that make it possible for us to do anything in the labs. Sander, Mark, Thomas, Bartjan and Reinout, from ARCNL; Bob, Dimitry, Andries, Igor and Hans from AMOLF/Amsterdam Nanocenter; Michiel and Hans from the Molecular Photonics group of UvA; Michaela, Dimitrios and Roberto from the Paul Scherrer Institute.

I also want to express my gratitude to the people that I met and who supported me from outside of the lab.
(DJ) Dennis, thank you so much for everything you showed me during the past six years. We have done a lot together and I hope that we can keep doing just that. Thank you to the diner club (Simon, Ilias, Jesse and Dennis) for the diners, the excess of wine and all the fün. Shout out to Marteen for the creek, the sauna and the wood fire. Simon, thank you for being a great

lockdown neighbor, working-out and discussing the stonk together helped me a lot during the writing process.

Thank you to my teammates for the trips all over Europe, the games, the practices, the pain, the smiles and the couple of championships. Dylan, thank you for becoming a great friend and continuously providing me with interesting stuffs to discover. Special thanks for the Dutch translations and go Blues (this year is your year).

To all the people that I met in ACTA or similar places, I am glad that our paths have crossed. Thank you for the fun and the often weird, yet amazing, experiences.

Thank you to my friends from France who supported me, often without knowing it. Théo, for the Christmas Eves, Dudu for the apex wins and to the whole BQC for being with me since the beginning, and hopefully forever. Lise, thank you for making me laugh for so long and for listening to me without judgment. Charlene, thank you for listening to me with judgment. Rémi, thank you for doing both.

Thank you to my parents and family for their unconditional love and support. Aurore, Sacha and Côme, you have been the perfect addition to this family. Germain et Mélanie, it was an incredible advantage to be able to look up to you as you consistently taught me more than I needed, before I could even understand what I need. Papa et maman, I cannot thank you enough. You made all of this possible. Always available since the first day to help me whenever I needed. For you I am grateful beyond words.

To Suzanne's family, thank you for welcoming me with open arms and being so nice to me all the time.
Suzanne, thank you for your love and constant support during my PhD, the writing process (and the concurrent covid lockdowns) and all of my other projects. Thank you also for designing the cover of the thesis and other schemes to illustrate my results, it means a lot to me. I look forward to return you the favor.

Olivier Lugier
Amsterdam, March 2021